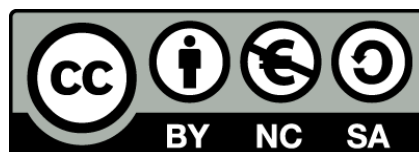




UNIVERSITAT DE
BARCELONA

Nanofabrication, simulation and optical characterization of plasmonic nanostructures

Ana Conde Rubio



Aquesta tesi doctoral està subjecta a la llicència **Reconeixement- NoComercial – Compartir Igual 4.0. Espanya de Creative Commons.**

Esta tesis doctoral está sujeta a la licencia **Reconocimiento - NoComercial – Compartir Igual 4.0. España de Creative Commons.**

This doctoral thesis is licensed under the **Creative Commons Attribution-NonCommercial-ShareAlike 4.0. Spain License.**

PhD Thesis

Nanofabrication, simulation and optical characterization of plasmonic nanostructures

Ana Conde Rubio

under the supervision of

Prof. Xavier Batlle

Prof. Amílcar Labarta



Institut de Nanociència
i Nanotecnologia



UNIVERSITAT DE
BARCELONA

Nanofabrication, simulation and optical characterization of plasmonic nanostructures

Memòria presentada per optar al grau de doctor per la

Universitat de Barcelona

Programa de doctorat en Nanociències

Autora:

Ana Conde Rubio

Directors:

Prof. Xavier Batlle (tutor)

Prof. Amílcar Labarta

Departament de Física de la Matèria Condensada

Institut de Nanociència i Nanotecnologia (IN2UB)

Universitat de Barcelona



Institut de Nanociència
i Nanotecnologia



UNIVERSITAT DE
BARCELONA



Aquesta tesi doctoral està subjecta a la llicència Reconeixement – NoComercial – CompartirIgual 4.0 Espanya Creative Commons (cc by-nc-sa)

Esta tesis doctoral está sujeta a la licencia Reconocimiento – NoComercial- CompartiIgual 4.0 España de Creative Commons (cc by-nc-sa)

This doctoral thesis is licensed under the Creative Commons Attribution-NonCommercial - ShareAlike 4.0 Spain License (cc by-nc-sa)

A mis padres,

Acknowledgments

Esta tesis no habría sido posible sin la ayuda de muchas personas que, de una forma u otra, han estado a mi lado durante todo este tiempo y por eso me gustaría dedicarles unas palabras.

En primer lugar, Xavi y Amílcar, gracias por confiar en mí. El comienzo no fue fácil y el final...tampoco mucho. Gracias por vuestro esfuerzo y dedicación, por buscar solución a todos los problemas y por vuestra infinita paciencia. Vuestro optimismo y entusiasmo han sido de gran ayuda.

También quiero dar las gracias de todo corazón a Francesc, que me acogió desde el primer día como una más de su grupo e hizo todo lo posible para que en el CNM también lo fuera. Gracias por tu inestimable ayuda a lo largo de todos estos años.

Miroslavna y Nerea, sin vosotras todo habría sido mucho más difícil. Muchas gracias por dedicar vuestro tiempo a enseñarme y guiarme en el comienzo de la tesis.

También me gustaría agradecer a Arantxa su participación en discusiones científicas, sugerencias y revisiones en el último año.

Todo este trabajo no habría sido posible sin la ayuda de todos los técnicos y personal de la sala blanca del CNM, ICN2, la UAB, la administración y los CCiTUB y por eso me gustaría agradecerles su ayuda. Al área de nanos y en especial a Xevi por su ayuda en mis comienzos con el e-beam, a Albert y a Jordi en su faceta de técnico :P. Al área de hornos, en especial a Ricard por estar siempre dispuesto a buscar una solución a mis problemas y a Sara por la rapidez en los momentos de crisis. Gracias también al área de RIE, Roser y Carles, por aguantar las quejas y problemas con el AMS y a Raquel por sufrir mis meses pre-estancia ajustando recetas y haciendo mil grabados cuando el AMS se tomó vacaciones. También a Raúl, por todas las evaporaciones. No me olvido del área de fotolito, ¡todavía queda un RUN pendiente! A Cristina, Bea y Elena, por ser tan eficientes y facilitarnos todo el papeleo.

I would also like to thank Prof. Giessen for giving me the opportunity to do a research stay in his group, it was a very enriching experience. Thanks also to Florian, Nik, Bettina and Marco for helping me during my stay. Bowen, it was a pleasure sharing the office with you!

Gracias también a los investigadores con los que he tenido el placer de colaborar: al Prof. Andrés Cantarero y a Daniel Cuesta, de la Universidad de Valencia y al Dr. Agustín Mihi, al Dr. André Espinha y a Cristiano Matricardi del ICMAB.

Pero por suerte, no todo es trabajo. Recuerdo perfectamente el día que llegué a Barcelona. Aurora me acogió en su casa y aguantó mi desesperación de los primeros días buscando piso, muchas gracias por eso y por ‘compartir Piedrafita’ con nosotros, siempre es un buen lugar para airear la mente. Ese mismo día quedé con Alberto y fui a mi primera reunión de ESN. Desde ese momento, ESN se convirtió en mi familia en Barcelona. Mirando atrás, me acuerdo de lo que era la asociación cuando empecé y en lo que se ha convertido y estoy orgullosa de todas las personas que han hecho esto posible, espero que sigáis así. Los viajes, tours, el running y vóley playa, los eventos culturales, fiestas, y los ‘tándems lingüísticos’ son solo algunas de las experiencias inolvidables que he podido compartir con todos vosotros. Muchas gracias a todos por contribuir a mi “Barcelona Experience”. Ana y Marc, sin nuestras quedadas gourmet a ponernos al día nada sería lo mismo; Alex e Irene, probablemente sin vosotros habría acabado antes la tesis, pero no habría sido lo mismo; Guillem, aunque haya abandonado el tándem para siempre y nuestras agendas sean complicadas, algún día conseguiremos ponernos de acuerdo; Barrins, eres un amor, da gusto estar con gente como tú, espero un directo de ukelele; Rafa, y Porron, el final de la tesis implica celebración, cuento con vosotros. Acabada la tesis, cierro también esta etapa para dejar hueco a los nuevos que vienen cargados de entusiasmo y energía.

Dentro de la parte ociosa incluyo también a mis compañeros a lo largo de todos estos años. Gracias a Carlos por su ayuda en mis comienzos, por introducirme en las comidas del v445. Después de estar sola en un despacho se valora mucho más la compañía, por eso ha sido un placer tener mi mesita en la “good vibes office” y compartir despacho con gente estupenda como vosotros Lauri, Jordi, Albert, Steven, Angelos, Marta, Alberto, Olga, Christian, Sophie, Nil, Alex, Marcos y Javi. Y a falta de uno, finalmente conseguí mi segundo despacho, el 4.11. Mariona, Gian, Xavi, Guille, Elisenda y Nahuel, he disfrutado de vuestra compañía...y de los muchos momentos de soledad XD. Mariona, ha sido un placer compartir contigo estos años, no desesperes, todo lo bueno se hace esperar.

No me olvido del grupo de los gordis (Sara, Liber, Sacris, María, Lauri y Sergi), por los buenos tiempos, porque siempre se piensa mejor con azúcar en vena, verdad Sergi?

Iulia and Lisa, it was a pleasure to be your flatmate during my stay. Thank you for everything, I felt like at home with you. Thank you Linda for your room, especially for the extra-time. El grupo de “Senderos por Stuttgart” hicisteis que disfrutara al máximo mi estancia, todavía me sorprende ver la cantidad de cosas que hice con vosotros ¡en solo 3 meses! Os debo una visita.

Lauri, gracias. Has estado ahí desde el principio hasta el final. Muchas gracias por tus consejos y apoyo, en lo profesional y lo personal. Gracias por entender mis momentos de estrés y por tener infinita paciencia. Este último año se ha hecho cuesta arriba sin ti.

A todos los amigos, que aunque están lejos, siempre están cuando los necesitas, gracias. A mis hermanitas adoptivas, Irene, Carmen y Marta, el piso sin vosotras no es lo mismo, os echo de menos. Eva, porque cada vez que entro en crisis estás ahí. Artu, porque todavía no sé porque pero siempre creíste en mí y me animaste a hacer todo lo que me proponía. Ruben, por toda tu cariño y comprensión. Inés, porque llevamos toda la vida juntas y por mucho tiempo que pasemos sin vernos, cuando coincidimos, todo sigue igual.

Bernat, al final te has ganado tener un huequito aquí. Ha sido divertido escribir en paralelo la tesis. Si no fuera por ti, seguiría importando archivos uno a uno, pero por suerte terminé. Me he ganado una birra, ¿no? :P Gracias por ver siempre el lado positivo de las cosas, por hacerme reír incluso en los momentos más difíciles y por venir a rescatarme en plan *superhero* cuando me ahogo en un vaso de agua. Gracias por sacarme a respirar aire puro, por tener siempre plan A, B, C...y hasta Z y, sobre todo, por hacer que este año tan duro haya pasado tan rápido.

Pero, sobre todo, gracias a mi familia. Paula, muchas gracias por aguantar mis monólogos interminables. Fue un placer compartir un año juntas en Barcelona, gracias por las noches de nachos y peli, por las visitas a mercadillos, por las cenitas y noches de fiesta y las otras “cositas en Barcelona”. Llegaste probablemente cuando más lo necesitaba y sin ti no habría sido lo mismo, espero que algún día volvamos a coincidir en la misma ciudad. Mientras tanto, mucha suerte y ¡a darle duro! Papá y mamá, si estoy aquí ha sido gracias a vosotros. Llevo toda mi vida rodeada de ciencia, desde los juguetes de navidad pasando por museos, libros, familia y casi todos vuestros amigos, si hubiera salido de letras habría sido altamente sorprendente. Habéis sido un gran ejemplo a seguir, sin vuestra ayuda, apoyo y confianza no hubiera sido capaz, gracias.

Esta tesis ha sido realizada gracias a una beca FPI concedida por el MINECO.

Motivation

“Basically, I have been compelled by curiosity.”

Mary Douglas Leakey

‘There is plenty of room at the bottom’, said Richard Feynman in his famous lecture in 1959, and so it is. When we go down to the nanoscale, properties change and new phenomena appear. While most people picture metals as simple shiny materials, downscaling their size results in new fascinating properties that arise from the coupling of their surface electrons to the electric field of light.

These properties are already present in nature. For instance, the wings of butterflies are composed of microstructured scales that behave as natural photonic crystals. The stunning color of beetles is also originated from the structures present in their skin that act as scattering centers. In fact, plasmonic structural color is a very active research field today where structures are engineered to obtain color by changing their reflective or diffractive properties.

Examples are found not only in nature, but also in human-made objects from ancient times. This is the case of the colorful stained glass windows obtained thanks to colloidal metallic nanoparticles. Yet, the physical explanation for these properties remained unknown for a long time. It was not until the 19th century that Faraday attributed these properties to the presence of colloidal particles and the first theoretical studies were not published until the 20th century, the most famous one being the Mie theory that is still applied today to explain the plasmonic response of metallic nanoparticles (*G. Mie, 1908*). However, technical difficulties in the fabrication and in the numerical methods delayed the development of the field for over fifty years.

Today, the field of plasmonics has reached its hype with discoveries such as extraordinary optical transmission or negative refractive index materials and applications in a wide variety of fields such as sensing, photovoltaics or medicine. The ability to confine light into subwavelength dimensions enables imaging below the diffraction limit. The enhanced light-matter interaction can be used to increase the spontaneous emission rate of quantum objects. Moreover, tailoring the resonant behavior of plasmonic

nanostructures can be used to design plasmon rulers or perfect absorbers. Nonetheless, these are only a few examples.

Of course, there are still some limitations; probably the most important one is dealing with optical losses. Despite that fact, plasmonics is a field of research still full of potential to cover several technological needs faced nowadays.

Foreword

“How to get the best of it all? ...To struggle and to understand - never this last without the other; such is the law.”

George Leigh Mallory

This Ph.D. thesis is devoted to the nanofabrication, simulation and optical characterization of arrays of plasmonic nanostructures. The manuscript is divided in three sections, each one sub-divided in several chapters.

Section I is a general introduction to the field of plasmonics. **Chapter 1** summarizes the theoretical aspects involved in the thesis. To find the physical response of plasmonic nanostructures to light, Maxwell equations have to be solved. Hence, Maxwell’s equations and numerical methods to solve them are discussed. The response of the structure also depends on the optical properties of the material, and in particular, its permittivity. Thus, a brief discussion of properties of metals and their viability for plasmonics is presented. To conclude, the limitations of the classical theory are discussed. **Chapter 2** describes different approaches to fabricate plasmonic nanostructures, addresses the typical characterization techniques and briefly outlines some of the most extended applications of plasmonic nanostructures nowadays.

Section II is devoted to the study of arrays of Au cylindrical nanocups. In **Chapter 3**, the fabrication process combining thermal nanoimprint lithography and sputtering metallization is detailed. A trilayer stack (resist-oxide-resist) is used to overcome the high aspect ratio limitation of nanoimprint lithography by decoupling the lithography process from the layer that controls the height of the nanostructures. Besides, the proposed fabrication process enables for an easy tunability of the geometry and combination of different materials can also be combined. Moreover, the same process can be adapted to fabricate solid structures by changing the metallization process from sputtering to electron beam evaporation. In **Chapter 4**, the optical properties of Au nanocups are analyzed. This includes both simulation and optical characterization of the nanostructures, their tunability and possible applications, including their use as perfect absorbers. For certain geometries, these structures present an excitation mode that concentrates the electric field inside the cavity. As compared to the most extended spherical cups, thanks to their symmetry, our cylindrical nanostructures allow for a

homogeneous enhancement of the electric field within the cavity that could be of interest to enhance the response of their possible content. This may be of interest for example for Surface Enhanced Raman Spectroscopy, where the resonance of the structures can be tuned to match the wavelength of the excitation laser, greatly enhancing the inefficient Raman process and reaching even single molecule detection. Also, by using a metal-insulator-metal configuration, dense arrays of Au cylindrical nanostructures have shown high absorption in the visible and near infrared regions on the spectra.

Section III is dedicated to hexagonal lattices of geometrically frustrated plasmonic arrays of nanoelements. Inspired by geometrically frustrated magnetic systems, different geometries have been studied, all of them designed in such a way that the pitch is on the order of the resonance wavelength and the gaps between them are small enough to allow near-field coupling. In **Chapter 5**, several lattices of nanoelements are studied, all of them presenting high absorption peaks and an extended time response due to the frustration induced by the geometry of the array. **Chapter 6** discusses the nanofabrication and the optical characterization of these arrays. Electron beam lithography has been used to enable an easy study of the optical response of the system as a function of the geometric parameters of the lattices. Fourier Transform Infrared Spectroscopy has been used to characterize the absorption of the samples, showing a very good agreement with the simulation results. Finally, some preliminary results of the application of these arrays as Surface Enhance Raman Spectroscopy substrates are presented.

List of abbreviations:

AFM	Atomic Force Microscope
EBL	Electron beam lithography
EM	Electromagnetic
FDTD	Finite Difference Time Domain
FTIR	Fourier transform interferometer
FWHM	Full width at half-maximum
IR	Infrared
LSP	Localized surface plasmon
LSPR	Localized surface plasmon resonance
MIM	Metal-insulator-metal
NIL	Nanoimprint Lithography
NIR	Near Infrared
PECVD	Plasma Enhanced Chemical Vapor Deposition
PML	Perfectly-matched layer
PMMA	Polymethyl methacrylate
RIE	Reactive ion etching
SEIRA	Surface enhanced infrared absorption
SEM	Scanning Electron Microscopy
SERS	Surface Enhanced Raman Spectroscopy
SLR	Surface Lattice Resonance
SNOM	Scanning near-field optical microscopy

SP	Surface Plasmon
SPP	Surface Plasmon Polariton
SPR	Surface plasmon resonance
TFSF	Total-field scattered-field
UV	Ultraviolet
VIS	Visible

Table of contents

SECTION I	1
1. Introduction	3
1.1. Introduction	3
1.2. Optical constants for metals	6
1.2.1. The Drude model	7
1.3. The use of Au for plasmonics	8
1.4. Maxwell's equations	9
1.4.1. The quasi-static regime	10
1.4.2. Mie theory	11
1.4.3. Beyond the quasi-static approximation	12
1.5. Numerical methods to solve Maxwell equations	13
1.5.1. FDTD simulations	13
1.6. Reaching quantum phenomena	15
1.7. Conclusions	16
1.8. References	17
2. Nanofabrication and characterization of plasmonic nanostructures	21
2.1. Introduction	21
2.2. Nanofabrication: lithographic techniques	22
2.2.1. Photolithography	22
2.2.2. Direct writing techniques	26
2.2.3. Soft lithographies	32
2.2.4. Lithographies based on self-assembly	34
2.3. Nanofabrication for plasmonics: special issues to solve	37
2.4. Characterization of plasmonic nanostructures	38

2.4.1.	Far-field characterization.....	38
2.4.2.	Near-field characterization.....	41
2.5.	Applications.....	42
2.5.1.	Sensing.....	43
2.6.	Conclusions, limitations and outlook.....	48
2.7.	References.....	49

SECTION II

55

3. Fabrication of cylindrical nanocups by NIL and sputtering..... 57

3.1.	Introduction.....	57
3.2.	Fabrication method.....	58
3.2.1.	Mold.....	59
3.2.2.	Fabrication of the sample.....	63
3.2.3.	Tunability of the fabrication process.....	69
3.3.	Large area fabrication.....	71
3.4.	Fabrication of nanocups by nanoimprinting.....	72
3.5.	Conclusions.....	73
3.6.	References.....	74

4. The plasmonic response of Au nanocups 77

4.1.	Introduction.....	77
4.1.1.	Nanoshells: highly tunable plasmonic nanostructures.....	77
4.1.2.	Open nanoshells: semishells, nanocaps, nanocups, etc.....	80
4.1.3.	Our system: hollow cylindrical nanocups.....	82
4.2.	The choice of the material.....	83
4.3.	Tunability of the plasmonic response.....	84
4.3.1.	Far-field spectra.....	84
4.3.2.	Near-field response.....	85
4.4.	The effect of the adhesion layer.....	88
4.5.	The effect of the substrate and the embedding medium.....	89

4.6.	Optical characterization of the nanocups	90
4.7.	Plasmonic perfect absorbers.....	92
4.7.1.	Metamaterial perfect absorbers.....	92
4.7.2.	Nanocups as perfect absorbers.....	94
4.8.	Possible applications of Au nanocups.....	95
4.8.1.	Surface Enhanced Raman Spectroscopy.....	95
4.8.2.	Surface Plasmon Resonance sensing.....	96
4.8.3.	Gas sensing.....	96
4.9.	Conclusions and further work.....	97
4.10.	References	99

SECTION III

105

5. Geometric frustration in plasmonic arrays

107

5.1.	Introduction.....	107
5.2.	Coupling in nanoantennas.....	107
5.3.	Previous studies of lattices of plasmonic nanoelements.....	108
5.4.	Triangular lattice of disks	110
5.5.	Honeycomb lattice of bars.....	114
5.6.	Triangular lattice of asterisks.....	117
5.7.	Conclusions and further work.....	121
5.8.	References	122

6. Arrays of plasmonic nanoelements: experimental results

127

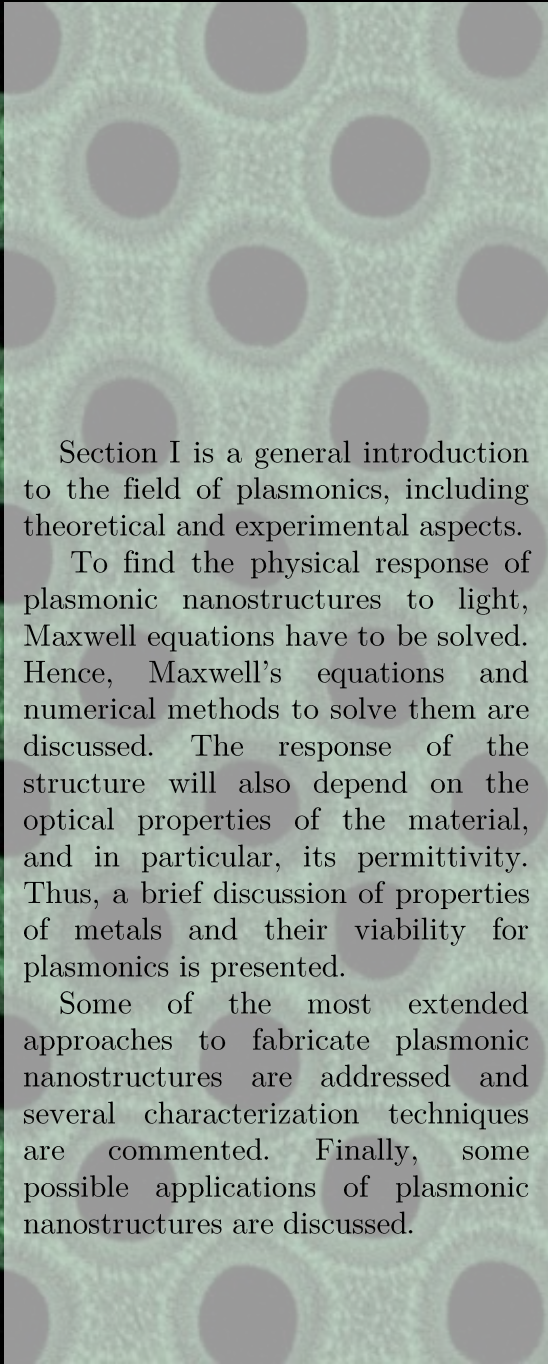
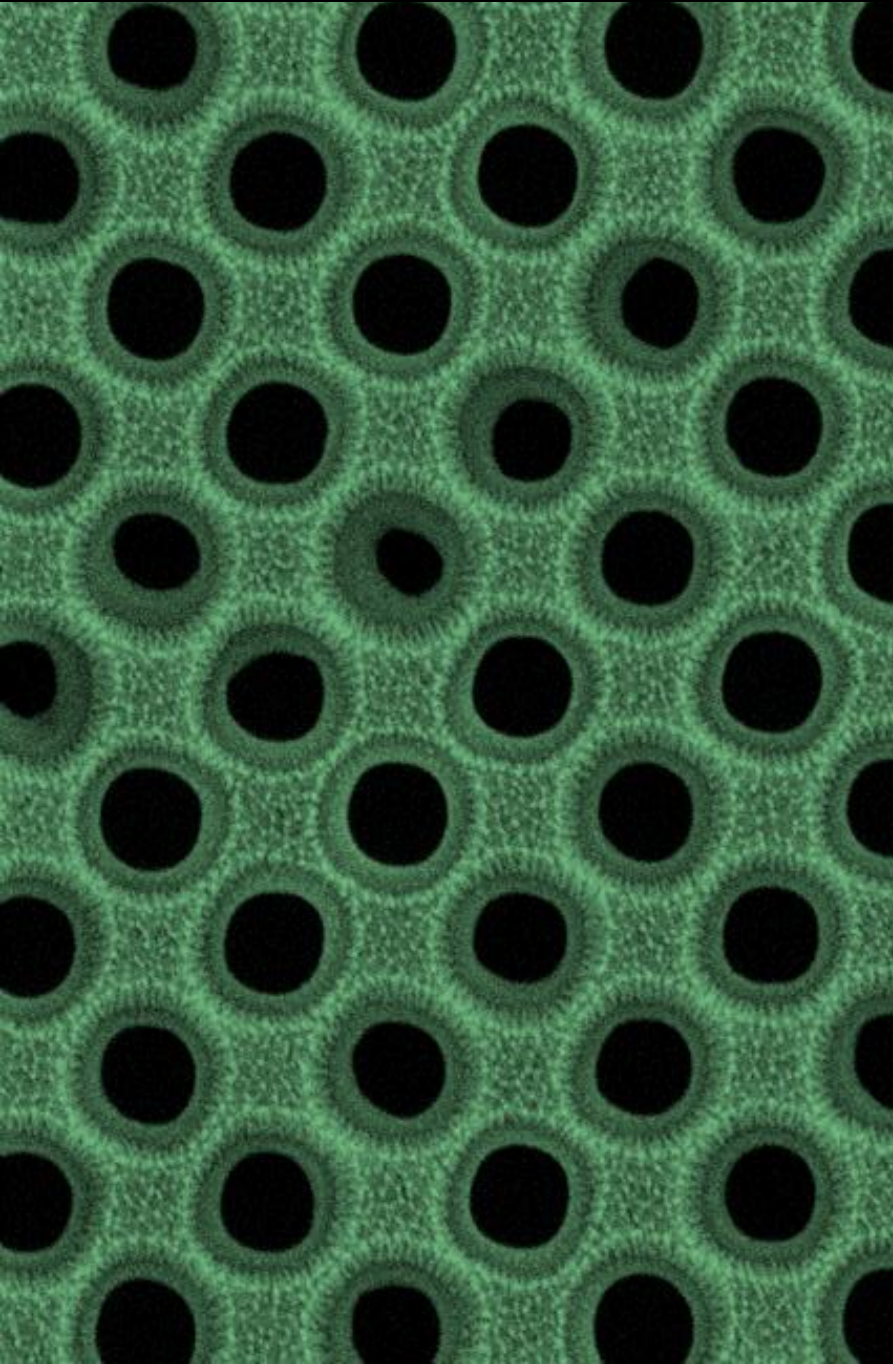
6.1.	Introduction.....	127
6.2.	Triangular lattice of asterisks.....	127
6.2.1.	Plasmonic response of a single nanoasterisk.....	128
6.2.2.	Plasmonic response of a lattice of asterisks.....	130
6.2.3.	Fabrication of the samples.....	133
6.2.4.	FTIR characterization	136
6.2.5.	Differences between simulations and experimental results	137

6.2.6.	Arrays of nanoasterisks as substrates for SERS	141
6.3.	Exp. results: honeycomb lattice of bars and triangular lattice of dots..	143
6.4.	Conclusions and further work.....	145
6.5.	References	147
General conclusions.....		149
Appendix A.....		153
A.1.	Introduction.....	153
A.2.	FDTD simulations in Lumerical.....	154
A.2.1.	Meshing.....	154
A.2.2.	Material modelling.....	155
A.2.3.	Boundary conditions.....	156
A.2.4.	Sources	156
A.2.5.	Simulations with unpolarized light	157
A.3.	References.....	158
Appendix B.....		159
B.1.	Peer-reviewed publications.....	159
B.2.	Contributions to scientific events.....	160
Resumen.....		165



SECTION I

INTRODUCTION



Section I is a general introduction to the field of plasmonics, including theoretical and experimental aspects.

To find the physical response of plasmonic nanostructures to light, Maxwell equations have to be solved. Hence, Maxwell's equations and numerical methods to solve them are discussed. The response of the structure will also depend on the optical properties of the material, and in particular, its permittivity. Thus, a brief discussion of properties of metals and their viability for plasmonics is presented.

Some of the most extended approaches to fabricate plasmonic nanostructures are addressed and several characterization techniques are commented. Finally, some possible applications of plasmonic nanostructures are discussed.

Chapter 1

Introduction to plasmonics

1.1. Introduction

When an electromagnetic (EM) wave reaches a metallic nanostructure, the cloud of free electrons in the metal can support a collective oscillation. These oscillations reach a maximum at the so-called surface plasmon resonance (SPR), whose intensity and wavelength depend on factors such as the material, the size and the geometry of the nanostructure, and the embedding medium.¹ Plasmons give rise to effects such as strong light confinement or enhanced light-matter interactions which are exploited for different applications.

Regarding the excitation of surface plasmons, we can distinguish two main cases (see Figure 1.1): (i) Surface Plasmon Polaritons (SPP), which are propagating charge oscillations bounded to the interface between a metal and a dielectric, with an evanescent decay on both sides of the interface; and (ii) Localized Surface Plasmons (LSP), which appear in metallic nanoparticles smaller than the wavelength of the incident radiation and result in non-propagating oscillations of the surface electrons in the metallic nanostructure. To be able to excite SPP, the momentum and the frequency of the incoming wave have to match the corresponding values for the SPP in the metallic film.

$$k_{spp} = k \sqrt{\frac{\epsilon_d \epsilon_m}{\epsilon_d + \epsilon_m}}$$

Hence, the momentum of the SPP wave is larger than that of light in free space, resulting in a momentum mismatch that has to be overcome somehow by coupling light and SPP modes at the interface when $\epsilon_d + \epsilon_m = 0$.² The three main ways to match the missing momentum are: the coupling through a prism by using total internal reflection, the scattering from a defect, protrusion or hole that generates surface plasmons locally, and the use of gratings or corrugations.³ However, exciting LSP only requires frequency matching since they do not have propagating character, making them much easier to be excited.

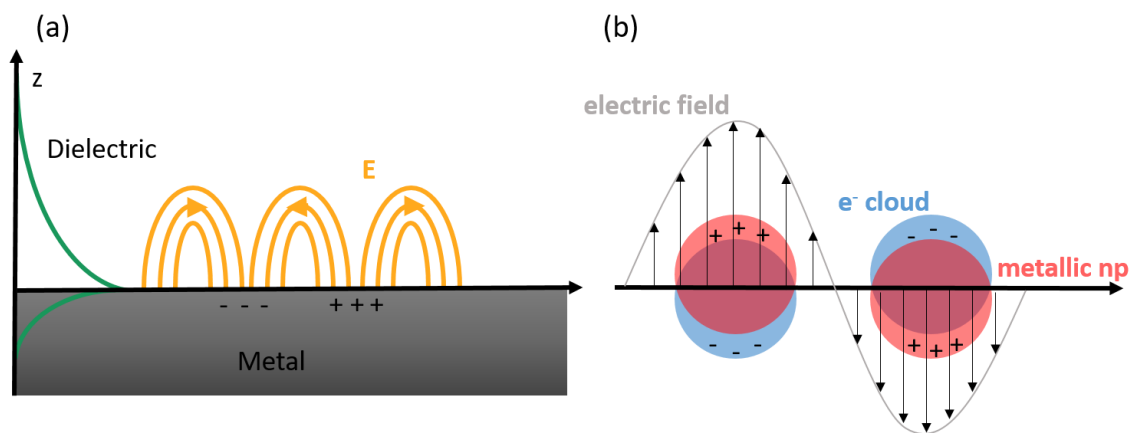


Figure 1.1(a) Scheme of SPP. The electric field of the incident EM wave induces oscillations in the charge density of the metal surface that results in an evanescent wave called surface plasmon polariton. The amplitude of these coupled oscillations decays exponentially in both media. (b) Scheme of LSP. When the incident electric field impinges a metallic particle, the free electrons of the metal can oscillate collectively giving rise to the so-called localized surface plasmons.

First studies related to plasmonics were carried out in the beginning of the 20th century, by Zenneck,⁴ Mie,⁵ and Sommerfeld⁶ but most of their work was forgotten for over fifty years due to the difficulties found at that moment to solve the complicated equations involved without powerful computers.

Nevertheless, plasmonic nanoparticles were used much earlier. An example of the use of plasmonic nanoparticles is the famous Lycurgus cup (Figure 1.2(a)), whose glass parts contain colloidal Au and Ag nanoparticles. When light penetrates from the outside, the cup appears green as a result of the strong scattering of light by the metallic nanoparticles. However, when the light source is located inside the cup, the object turns red due to the modified transmission spectrum as a consequence of the absorption of light by the metallic nanoparticles. In the Roman Empire, nanoparticles were already used as

colorants and in the middle-ages, colloidal Cu, Ag and Au nanoparticles were also used to obtain yellow and red colors in stained glass windows (Figure 1.2(b)), being Michael Faraday the first one attributing this behavior to the presence of colloidal nanoparticles.⁷

However, in the last decades, thanks to advances in nanofabrication techniques, computing resources and imaging tools, plasmonics has reappeared with renewed strength, finding applications in very diverse fields. For example, the ability to confine light can be used for imaging below the diffraction limit or in integrated photonics, for instance, to improve waveguides. Besides, LSP enable an efficient transfer of the energy from the near- to the far-field and *vice versa*. Hence, inspired in the idea behind radio-wave antennas, small metallic nanoparticles can be used as nanoantennas working at much higher frequencies. Moreover, the enhancement of the electric field can be used to improve processes that are not very efficient such as fluorescence,^{8,9} Raman scattering¹⁰⁻¹² or infrared absorption,¹³⁻¹⁵ reaching single-molecule detection capabilities. The ability to transform light into heat has also been used in photothermal cancer therapy.^{1,16} Also, nanostructures and nanoparticles can be tailored to exhibit enhanced absorption or scattering for certain wavelengths, and this is applied in many different fields, as for example to be used as the so-called plasmon rulers, a combination of high-resolution plasmonic spectroscopy and coupled plasmonic elements with sharp spectral features and high sensitivity, that can be used as nanometric distance rulers by measuring the changes in the spectrum,¹⁷ or to improve the efficiency of photovoltaic cells.¹⁸



Figure 1.2. (a) Lycurgus cup. Reprinted from britishmuseum.org

In this Chapter, I will present a brief introduction to plasmonics, summarizing the main theoretical aspects needed for later discussions. First, the optical constants for metals are analyzed and a justification for the use of Au is given. Then, a few comments on how to solve Maxwell equations for the simplest cases and the need of numerical approximations for more sophisticated ones are discussed. Possible quantum effects for the very small particles are also considered. Finally, the use of the classical theory for all the problems addressed in this dissertation is justified.

1.2. Optical constants for metals

In order to generate a SPR, a constricted gas of electrons is needed, which is usually supplied by metals. Whereas for low frequencies these materials behave as perfect conductors, for higher frequencies in the range of infrared (IR) or visible light their behavior is completely different. To understand the difference between the response for low and high frequency EM waves, one can use the mass-and-spring model, being the restoring force the Coulomb interactions between the electrons and the ions in the metal. For low energies, electrons can follow the excitation of the oscillating field, but as the frequency increases, the amplitude and the phase lag are both increased, until the amplitude reaches a maximum that corresponds to the SPR.

As a consequence, the response of metals at optical frequencies can be described by a complex frequency-dependent dielectric function, $\varepsilon(\omega)$:

$$\varepsilon(\omega) = \varepsilon_1(\omega) + i\varepsilon_2(\omega)$$

and an induced polarization density $P(\omega)$ that is related to the electric field $E(\omega)$ as:

$$P(\omega) = \varepsilon_0[\varepsilon(\omega) - 1]E(\omega)$$

Ohmic absorption is proportional to the material conductivity $\sigma(\omega)$, which is related to the imaginary part of the dielectric function through the expression:

$$\varepsilon_2(\omega) = \frac{\sigma(\omega)}{\varepsilon_0\omega}$$

making desirable to find materials with a low imaginary part of $\epsilon(\omega)$. Besides, Ohmic losses take place close to the surface, within the so-called penetration depth. So keeping them as low as possible using materials with either large (negative) real part of $\epsilon(\omega)$ to reduce the penetration depth - in Au, the penetration depth is 31 nm for a wavelength of 620 nm- or small imaginary part to directly reduce the losses, are largely advisable.¹⁹

1.2.1. The Drude model

In the range of optical frequencies, the response of metals (and other materials such as conducting oxides or doped semiconductors) is determined by the collective behavior of the free electron cloud, and they can be well described by a simple free-electron model, valid for frequencies below the interband transition, that is, the Drude model.²⁰

In 1900, only three years after the discovery of the electron by Thomson, Drude proposed his theory to explain the transport properties of electrons in materials. This theory, based on considering the conductor material as a crystalline lattice with fixed ions and a gas of non-interacting electrons that move freely, correctly explained the Ohm law as well as the decrease of the conductivity with temperature. However, Drude's model has several limitations. Sommerfeld based his theory on the same points as Drude's model but he introduced a quantum treatment of the electron: the electron must obey Pauli's exclusion principle. Further corrections that took into account for the first time the Coulomb interactions of electrons with the ions of the crystalline lattice gave rise to energy bands and gaps where no solutions for the electronic states are allowed. However, the Drude-Sommerfeld method is enough to explain some of the properties of metals, and, in particular, their optical properties.

According to this model, the frequency dependence of the dielectric function is given by the following expression:

$$\epsilon(\omega) = \epsilon_\infty - \frac{\omega_p^2}{\omega(\omega + i\gamma_0)} \approx \epsilon_\infty - \frac{\omega_p^2}{\omega^2} + i \frac{\gamma_0 \omega_p^2}{\omega^3}$$

where $\omega_p = \sqrt{ne^2/\epsilon_0 m^*}$ is the plasma frequency, n and m^* being the density and the effective mass of the conduction electrons, respectively, and γ_0 the

electron relaxation rate (inverse of the relaxation time). ϵ_∞ accounts for the contribution of the bound electrons to the polarizability and equals 1 when only the electrons from the conduction band contribute to the dielectric function.

If we neglect the contribution of both the bound electrons and the electron relaxation time, the expression for the dielectric function simplifies to $\epsilon(\omega) = 1 - \omega_p^2/\omega^2$, and two cases can be distinguished. On the one hand, when $\omega > \omega_p$, ϵ is positive and the refractive index is given by $n = \sqrt{\epsilon}$. On the other hand, when $\omega < \omega_p$, ϵ becomes negative and the refractive index is imaginary, meaning the EM wave cannot propagate in that medium.²¹ For noble metals in the visible range, typically $\omega < \omega_p$, which means that this model accounts for (i) $\epsilon_1(\omega) < 0$, implying that the conduction electrons do not oscillate in phase with the applied field and explains the high reflectivity of metals since EM wave cannot propagate, and (ii) not negligible $\epsilon_2(\omega)$, which results in energy absorption and lossy behavior.²²

When comparing experimental results of the reflection and transmission to theory, one can conclude that the Drude-Sommerfeld model provides an accurate description for low energy. However, when increasing energy, the model distances from the experimental data due to the fact that it does not account for the case where photons with high enough energy cause interband transitions by promoting electrons from deeper valence bands to higher energy conduction bands.

1.3. The use of Au for plasmonics

As discussed in the previous section, the requirement for a material to have good plasmonic properties is having a dielectric function with a large negative real part and a small imaginary part. These conditions are fulfilled by noble metals, such as Ag, Cu and Au. The losses depicted by the imaginary part of $\epsilon(\omega)$ can be divided into intraband and interband losses. Interband transitions are reflected as an absorption edge above which all the SPR are strongly damped.^{23,24} Au and Cu have very similar dielectric constants: they have interband transitions around 2.3 eV (530-550 nm) and can be treated as free electron systems satisfying the Drude model below 2.1 eV (>600 nm), making them interesting for the range of red light and near infrared (NIR). For Ag, the

first interband transition is above 3.1 eV (<400 nm), which makes it better than Au for the range between 450 and 550 nm.¹⁹

An emerging material is Al, which has a larger negative real part of the dielectric function, approximating better to a perfect metal, and making it interesting for applications in the 400-600 nm wavelength range. However, the interband transition around 800 nm hampers its application in the NIR spectral region. Intraband losses, also known as Drude losses, in Al are high in the NIR.¹⁹

The chemical stability of these metals is also of great importance: Ag and Cu easily corrode in ambient conditions, forming oxides and sulfides and Al passivates forming thin Al₂O₃ layers. The tarnishing of these metals results in an increased imaginary part of the dielectric function and a concomitant increase in the optical losses. Consequently, Au, which combines good dielectric properties and chemical stability, is the most extended material for systems without protection layers and will be the material chosen for the structures fabricated along this dissertation.¹⁹

1.4. Maxwell's equations

To determine the plasmon resonance of particles or nanostructures, Maxwell's equations need to be solved. Maxwell's equations are a set of four equations that fully describe EM phenomena. They took the name after J. C. Maxwell who gathered together the experimental results from Gauss, Ampere, Faraday and Coulomb, unifying electricity, optics and magnetism, and setting down the foundation of classical electrodynamics in his famous article in 1865.²⁵

Maxwell's equations imply: i) electric charges generate electric fields, ii) there are no magnetic charges, and iii) changes in the electric fields induce magnetic fields and vice versa; and they are as follows:

Gauss law:	$\vec{\nabla} \cdot \vec{D} = \rho$
Gauss' law for magnetism:	$\vec{\nabla} \cdot \vec{B} = 0$
Maxwell-Faraday equation:	$\vec{\nabla} \times \vec{E} = -\partial \vec{B} / \partial t$
Ampère's law:	$\vec{\nabla} \times \vec{H} - \partial \vec{D} / \partial t = \vec{j}$

being $\vec{D} = \epsilon_0 \vec{E}$ and $\vec{B} = \mu_0 \vec{H}$ for linear materials, where \vec{E} is the electric field, \vec{H} is the magnetic field, \vec{D} is the electric displacement field, \vec{B} is the magnetic flux density, ρ is the free charge density, \vec{J} is the free current density, ϵ_0 is the permittivity of free space and μ_0 is the permeability of free space.

1.4.1. The quasi-static regime

The interaction of a particle with an EM field can be analyzed using the simple quasi-static approximation as long as the particle size is much smaller than the wavelength of light in the surrounding medium. In this case, the phase of the oscillating EM field is practically constant over the particle volume, so that one can calculate the spatial field distribution assuming the particle to be in an electrostatic field and add later the harmonic time dependence once the field distributions are known.

The simplest case would be that of an homogeneous isotropic sphere of radius a and dielectric constant ϵ_p , located at the origin of a uniform static electric field $\vec{E} = E_0 \hat{z}$, surrounded by an isotropic and non-absorbing medium of dielectric constant ϵ_m .

In the electrostatic approach, we need to find the solution to the Laplace equation for the potential $\nabla^2 \phi = 0$ to calculate the electric field, $E = -\nabla \phi$. Applying the boundary conditions and after some algebra (see Ref. 3 for the details) one obtains the expressions:

$$\phi_{in} = -\frac{3\epsilon_m}{\epsilon_p + 2\epsilon_m} E_0 r \cos\theta$$

$$\phi_{out} = -E_0 r \cos\theta + \frac{\epsilon_p - \epsilon_m}{\epsilon_p + 2\epsilon_m} E_0 a^3 \frac{\cos\theta}{r^2}$$

where ϕ_{out} describes the joint effect of the applied electric field together with that generated by the dipole located at the particle center. This expression can be rewritten as a function of the dipole moment \vec{p} :

$$\phi_{out} = -E_0 r \cos\theta + \frac{\vec{p} \cdot \vec{r}}{4\pi\epsilon_0\epsilon_m r^3}$$

with $\vec{p} = 4\pi\varepsilon_0\varepsilon_m a^3 \frac{\varepsilon_p - \varepsilon_m}{\varepsilon_p + 2\varepsilon_m} E_0$. Hence, the applied field induces a dipole moment inside the sphere that is proportional to the incoming electric field. If we introduce the polarizability α defined via $\vec{p} = \varepsilon_0\varepsilon_m \alpha \vec{E}_0$ as:

$$\alpha = 4\pi a^3 \frac{\varepsilon_p - \varepsilon_m}{\varepsilon_p + 2\varepsilon_m}$$

we can see that the polarizability exhibits a resonance when $|\varepsilon_p + 2\varepsilon_m|$ reaches a minimum, which for the case of a small or slowly changing imaginary part of ε_p happens for $Re[\varepsilon_p(\omega)] = -2\varepsilon_m$. The enhancement in the polarization comes together with an enhancement of the absorption and scattering, whose corresponding cross-sections are given by:

$$C_{scat} = \frac{k^4}{6\pi} |\alpha|^2 = \frac{8\pi}{3} k^4 a^6 \left| \frac{\varepsilon_p - \varepsilon_m}{\varepsilon_p + 2\varepsilon_m} \right|^2$$

$$C_{abs} = k Im[\alpha] = 4\pi k a^3 Im \left[\frac{\varepsilon_p - \varepsilon_m}{\varepsilon_p + 2\varepsilon_m} \right]$$

with $k = \frac{2\pi}{\lambda}$. Consequently, for small particles with $a \ll \lambda$, the absorption dominates over the scattering.³

All in all, nanoparticles with sizes smaller than the wavelength of the incoming wave act as electric dipoles, that present a resonant field enhancement due to a resonance in the polarizability for $Re[\varepsilon_p(\omega)] = -2\varepsilon_m$. However, when the size is increased, the dipole approximation can no longer be used due to the non-negligible phase changes of the driving field over the particle volume.

1.4.2. Mie theory

Many explanations had been given throughout history to explain the different colors that metallic particles in colloidal suspensions exhibited. However, it was not until 1908 that Mie found a theoretical solution to the optical properties that had been observed in metallic nanoparticles by solving Maxwell equations in the visible regime for spherical nanoparticles with diameters much smaller than the EM wave wavelength (below 200 nm) and neglecting particle interactions.⁵ The approach followed in what today is known as Mie theory consists in expanding the internal and scattered fields into a set of normal

modes described by vector harmonics. Using this theory, the results above for the quasi-static approximation are obtained by keeping only the first term of the power series.

1.4.3. Beyond the quasi-static approximation

A few comments that will later be helpful to analyze the response of our nanostructures are given hereafter referring to particles that go beyond the dipole regime. When particles increase in size, the expansion of the first Transverse Magnetic (TM) mode of Mie theory gives the following expression for the polarizability of a sphere:

$$\alpha_{sphere} = \frac{1 - \left(\frac{1}{10}\right)(\epsilon_p + \epsilon_m)x^2 + O(x^4)}{\left(\frac{1}{3} + \frac{\epsilon_m}{\epsilon_p - \epsilon_m}\right) - \frac{1}{30}(\epsilon_p + 10\epsilon_m)x^2 - i\frac{4\pi^2\epsilon_m^{3/2}}{3}\frac{V}{\lambda_0^3} + O(x^4)}V$$

where $x = \pi a/\lambda_0$ is a dimensionless parameter that relates the radius of the sphere, a , to the free space wavelength, λ_0 and V is the volume of the sphere. Analyzing the new terms with respect to the quasi-static approximation, we see a quadratic term in x in the numerator that accounts for the retardation of the field along the particle, leading to a shift in the SPR. The quadratic term in the denominator produces also a shift due to the retardation of the depolarization field inside the particle. For materials that can be described by the Drude model, this results in a redshift of the resonance with increasing size that can be understood as a consequence of having a bigger distance between charges at opposite interfaces of the sphere. Therefore, they are subjected to a smaller restoring force, resulting in a lower resonance frequency. That shift also implies that effects of interband transitions decrease as the plasmon resonance moves away from the interband transition edge.

The quadratic term in the denominator increases the magnitude of the polarization, decreasing the absorption due to the imaginary part of ϵ_p . However, the third term in the denominator, which accounts for radiation damping, acts in the opposite direction. In other words, there are two damping mechanisms: a radiative decay process yielding the emission of photons, which dominates for larger particles, and a non-radiative one due to absorption. The

non-radiative decay is due to the creation of electron-hole pairs via either intraband excitations within the conduction band or interband transitions from d-bands to sp conduction bands (in noble metals).

1.5. Numerical methods to solve Maxwell equations

The exact solution to Maxwell equations can only be obtained for some easy geometries such as spheres, spheroids, or infinitely long cylinders. However, solving Maxwell equations for arbitrary geometries requires the use of numerical methods. Solving 3D complex geometries has only been enabled recently, since it requires of powerful computing resources. Some of the most common approaches used in the field are: the discrete-dipole approximation,²⁶ the finite-element method, the multiple multipole method, the Boundary Element Method,^{27,28} and the finite difference time domain (FDTD).^{29,30}

1.5.1. FDTD simulations

The FDTD approach is one of the most extended numerical methods used in plasmonics thanks to its versatility. It belongs to the so-called differential methods. The key lies in discretizing Maxwell equations in time and space with central difference approximations. The differential equations obtained are then solved using leap-frog integration. Since it is a time-domain method, it allows for broadband simulations in a single run.³⁰ This method implies few inherent approximations and can deal with many types of problems and complex geometries, which makes it ideal to understand the plasmonic response of metallic nanostructures.

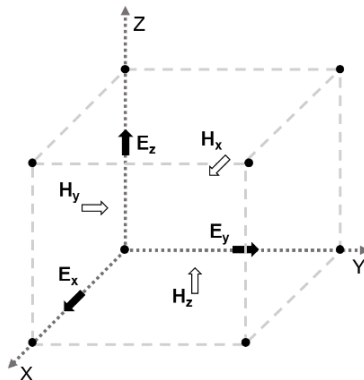


Figure 1.3. Scheme of a Yee cell showing the points at which the electric and magnetic field components are calculated.

FDTD or Yee method, named after the applied mathematician K. S. Yee, was first proposed in 1966, when he described the first space-grid time-domain numerical technique to find electric and magnetic fields by solving Maxwell's curl equations in time domain.²⁹

In terms of spatial calculations, space is discretized by creating a finite size mesh divided in the so-called Yee cells (Figure 1.3). It is recommended the spatial increments Δx , Δy and Δz to be smaller than $\lambda/20$, where λ denotes the wavelength of the incident wave. The time increment should satisfy the Courant condition, given by:

$$c_0 \Delta t \leq \frac{1}{\sqrt{\frac{1}{\Delta x^2} + \frac{1}{\Delta y^2} + \frac{1}{\Delta z^2}}}$$

The electric and magnetic fields are calculated in a slightly different place as shown in Figure 1.3 so they have a time shift of $\Delta t/2$. Therefore, the electric and magnetic fields for the next time step are calculated solving Maxwell's curl equations in the time domain alternatively, *i.e.*, the magnetic field at time $n + 1/2$ is calculated from the magnetic field at $n - 1/2$ and the electric field at n following the leap-frog algorithm described below:³¹

$$\vec{E}(t) \rightarrow \vec{E}^{n\Delta t} \qquad \vec{H}(t) \rightarrow \vec{H}^{(n+\frac{1}{2})\Delta t}$$

$$\vec{E}^{n+1} = \vec{E}^n + \frac{\Delta t}{\varepsilon} \vec{\nabla}_x \vec{H}^{n+1/2}$$

$$\vec{H}^{n+3/2} = \vec{H}^{n+1/2} - \frac{\Delta t}{\mu} \vec{\nabla}_x \vec{E}^{n+1}$$

$$\vec{E}^0 \rightarrow \vec{H}^{1/2} \rightarrow \vec{E}^1 \rightarrow \vec{H}^{3/2} \rightarrow \dots$$

As for the dielectric properties, the value of the permittivity is usually also discretized in space and it is calculated in each cell as an average value.

The fields are located as shown in Figure 1.3, which helps to calculate the curl from Maxwell equations. However, each field component is only known in a certain region of the space inside the unit cell.

Interfaces between different materials that pass through Yee cells can give rise to staircasing effects as fields are discontinuous at those points. To improve this, either a graded mesh, the use of conformal technology or a combination of both approaches can be used, since finite difference methods cannot resolve positions or layer thicknesses better than the mesh size.

Although this is a very accurate technique that can solve arbitrary geometries giving broadband results for many types of problems, one always has to keep in mind that the memory required for a 3D simulation is proportional to $V(\lambda/dx)^3$ and the simulation time scales as $V(\lambda/dx)^4$. The discontinuous Galerkin time-domain (DGTD) method has been proposed as an alternative to FDTD for large scale simulations or complex geometries with curved elements. DGTD works with unstructured meshes, which overcomes the limitations of the rectangular mesh used in FDTD and the memory consumption is drastically reduced. However, this comes at the expense of a more complex algorithm and a higher initialization cost.³²

The FDTD method has been extensively studied and custom code can be easily implemented. Along this dissertation thesis, the FDTD Solutions Package from Lumerical has been used. For further information about the simulations, one can refer to Appendix A.

1.6. Reaching quantum phenomena

One may wonder about the limits of the use of FDTD simulations or the classical Maxwell equations explained in the previous sections.

Along this chapter, the excitation of particles as a consequence of an incoming EM wave was treated as a purely classical phenomenon. In fact, this is valid for particles with radius as small as 1 nm due to the large concentration of conduction electrons in metals ($n \approx 10^{23} \text{cm}^{-3}$). For a small number of electrons ($N_e = nV$), the amount of energy gained by the electrons by interacting with the incident photons, given by $\Delta E \approx \frac{\hbar\omega}{N_e}$, becomes significant compared to $k_B T$. As a consequence, the coherent electron oscillation breaks down and a quantum mechanical treatment is necessary.³ Although the plasmon-like mode in

nanoparticles can appear for around 50 electrons, quantum confinement effects are still present for particles containing up to 500 electrons.³³

The other situation where quantum effects may not be neglected is when particles are very close to each other and they are strongly interacting. If we look at the changes in the spectrum when two nanospheres become closer, we observe redshifts and an enhancement of the electric field that evolve monotonically with decreasing gap separation. However, if the gap keeps being reduced, at some point, electron transfer between the two nanospheres will start. Thus, for gaps below 1 nm, the redshift saturates and the peak starts to blueshift due to the reduced coupling between the neighboring particles as a consequence of electron tunneling between them. Concurrently, the electric field enhancement is reduced. Hence, the classical theory is no longer valid and quantum mechanical theory must be used.³³

The fully quantum-mechanical treatment of the optical properties is highly complex. The most extended approach is the use of time-dependent density functional theory but, even this being a very simplified approach, the calculations are extremely time-consuming, making it necessary to use supercomputers.³³

1.7. Conclusions

Along this Chapter, a short introduction on the physics behind the optical response of plasmonic nanostructures has been given. In the following Chapters, several systems will be studied by solving Maxwell equations with the FDTD method. The quasi-static approximation will not (in general) be valid as we will study structures where retardation effects are already present. However, the study of the simplest case serves us to justify why absorption dominates over scattering for small nanoparticles and where the loopy properties of metals come from.

Moreover, the absence of quantum phenomena above 1 nm in both nanoparticle sizes and gap distances has been fully justified enabling, therefore, the classical treatment of our systems in the following Chapters.

1.8. References

1. Huang, X. & El-Sayed, M. A. Gold nanoparticles: Optical properties and implementations in cancer diagnosis and photothermal therapy. *J. Adv. Res.* **1**, 13–28 (2010).
2. Zhang, J., Zhang, L. & Xu, W. Surface plasmon polaritons: physics and applications. *J. Phys. D. Appl. Phys.* **45**, 113001 (2012).
3. Maier, S. A. *Plasmonics: Fundamentals and Applications*. (Springer US, 2007). doi:10.1007/0-387-37825-1
4. Zenneck, J. Über die Fortpflanzung ebener elektromagnetischer Wellen längs einer ebenen Leiterfläche und ihre Beziehung zur drahtlosen Telegraphie. *Ann. Phys.* **328**, 846–866 (1907).
5. Mie, G. Beiträge zur Optik trüber Medien, speziell kolloidaler Metallösungen. *Ann. Phys.* **330**, 377–445 (1908).
6. Sommerfeld, A. Über die Ausbreitung der Wellen in der drahtlosen Telegraphie. *Ann. Phys.* **333**, 665–736 (1909).
7. Faraday, M. The Bakerian Lecture: Experimental Relations of Gold (and Other Metals) to Light. *Philos. Trans. R. Soc. London* (1857). doi:10.1098/rstl.1857.0011
8. Bauch, M., Toma, K., Toma, M., Zhang, Q. & Dostalek, J. Plasmon-Enhanced Fluorescence Biosensors: a Review. *Plasmonics* **9**, 781–799 (2014).
9. Ayala-Orozco, C. *et al.* Fluorescence Enhancement of Molecules Inside a Gold Nanomatryoshka. *Nano Lett.* **14**, 2926–2933 (2014).
10. Gwo, S. *et al.* Plasmonic Metasurfaces for Nonlinear Optics and Quantitative SERS. *ACS Photonics* **3**, 1371–1384 (2016).
11. Vo-Dinh, T. Surface-enhanced Raman spectroscopy using metallic nanostructures. in *TrAC - Trends in Analytical Chemistry* **17**, 557–582 (1998).
12. Gonçalves, M. R., Enderle, F. & Marti, O. Surface-Enhanced Raman Spectroscopy of Dye and Thiol Molecules Adsorbed on Triangular Silver Nanostructures: A Study of Near-Field Enhancement, Localization of Hot-Spots, and Passivation of Adsorbed Carbonaceous Species. *J.*

- Nanotechnol.* **2012**, 1–15 (2012).
13. Neubrech, F., Huck, C., Weber, K., Pucci, A. & Giessen, H. Surface-Enhanced Infrared Spectroscopy Using Resonant Nanoantennas. *Chem. Rev.* **117**, 5110–5145 (2017).
 14. Brown, L. V. *et al.* Fan-Shaped Gold Nanoantennas above Reflective Substrates for Surface-Enhanced Infrared Absorption (SEIRA). *Nano Lett.* **15**, 1272–1280 (2015).
 15. Srajer, J. *et al.* Double-layered nanoparticle stacks for surface enhanced infrared absorption spectroscopy. *Nanoscale* **6**, 127–131 (2014).
 16. Ayala-Orozco, C. *et al.* Au nanomatryoshkas as efficient near-infrared photothermal transducers for cancer treatment: Benchmarking against nanoshells. *ACS Nano* **8**, 6372–6381 (2014).
 17. Liu, N., Hentschel, M., Weiss, T., Alivisatos, A. P. & Giessen, H. Three-Dimensional Plasmon Rulers. *Science (80-.)*. **332**, 1407–1410 (2011).
 18. Catchpole, K. R. & Polman, A. Plasmonic solar cells. *Opt. Express* **16**, 21793 (2008).
 19. Biagioni, P., Huang, J.-S. & Hecht, B. Nanoantennas for visible and infrared radiation. *Reports Prog. Phys.* **75**, 024402 (2012).
 20. Dastmalchi, B., Tassin, P., Koschny, T. & Soukoulis, C. M. A New Perspective on Plasmonics: Confinement and Propagation Length of Surface Plasmons for Different Materials and Geometries. *Adv. Opt. Mater.* **4**, 177–184 (2016).
 21. Li, M., Cushing, S. K. & Wu, N. Plasmon-enhanced optical sensors: a review. *Analyst* **140**, 386–406 (2015).
 22. Barnes, W. L., Dereux, A. & Ebbesen, T. W. Surface plasmon subwavelength optics. *Nature* **424**, 824–830 (2003).
 23. Wang, H., Tam, F., Grady, N. K. & Halas, N. J. Cu Nanoshells: Effects of Interband Transitions on the Nanoparticle Plasmon Resonance. *J. Phys. Chem. B* **109**, 18218–18222 (2005).
 24. Ye, J. *et al.* Plasmonic Modes of Metallic Semishells in a Polymer Film. *ACS Nano* **4**, 1457–1464 (2010).
 25. Maxwell, J. C. A Dynamical Theory of the Electromagnetic Field. *Philos.*

- Trans. R. Soc. London* **155**, 459–512 (1865).
26. Draine, B. T. & Flatau, P. J. Discrete-Dipole Approximation For Scattering Calculations. *J. Opt. Soc. Am. A* **11**, 1491 (1994).
 27. García de Abajo, F. J. & Howie, A. Relativistic Electron Energy Loss and Electron-Induced Photon Emission in Inhomogeneous Dielectrics. *Phys. Rev. Lett.* **80**, 5180–5183 (1998).
 28. García de Abajo, F. J. & Howie, A. Retarded field calculation of electron energy loss in inhomogeneous dielectrics. *Phys. Rev. B* **65**, 115418 (2002).
 29. Kane Yee. Numerical solution of initial boundary value problems involving maxwell's equations in isotropic media. *IEEE Trans. Antennas Propag.* **14**, 302–307 (1966).
 30. Taflove, A., Hagness, S. C. & London, B. I. *Computational electrodynamics: the finite-difference time-domain method.* (Artech House, 2005).
 31. Gallinet, B., Butet, J. & Martin, O. J. F. Numerical methods for nanophotonics: standard problems and future challenges. *Laser Photon. Rev.* **9**, 577–603 (2015).
 32. Niegemann, J., Pernice, W. & Busch, K. Simulation of optical resonators using DGTD and FDTD. *J. Opt. A Pure Appl. Opt.* **11**, (2009).
 33. Halas, N. J., Lal, S., Chang, W. S., Link, S. & Nordlander, P. Plasmons in strongly coupled metallic nanostructures. *Chemical Reviews* **111**, 3913–3961 (2011).

|Chapter 2

Nanofabrication and characterization of plasmonic nanostructures

2.1. Introduction

Thanks to the breakthroughs in nanofabrication, imaging tools and computer resources, plasmonics has experienced a thrilling advance in the last decades, yielding applications in a wide range of fields, such as sensing, nanofabrication, medicine, energy harvesting, etc...

Nanofabrication refers to the set of procedures and methods to obtain structures with, at least, one dimension in the nanometer scale. There are two large categories of nanofabrication methods as classified according to the way of nanostructuring: i) bottom-up methods, which consist in assembling molecules or atoms through physical or chemical interactions to form bigger structures; and ii) top-down methods, in which larger entities are downsized towards the nanometer scale.

Among the bottom-up methods, chemical routes have been, for a long time, the classical way to synthesize different kinds of nanoparticles with high throughput, enabling at the same time high tunability of the particle sizes and shapes. However, common drawbacks of all these methods are both the large

variability of the particle shape and the broad size distribution obtained within a single batch. Besides, in many plasmonics applications, having the particles in ordered arrays with control of both spatial distribution and orientation is highly convenient. Metal nanoparticles chemically synthesized can be arranged in an ordered manner by self-assembly so that one can monitor to a certain extent the interparticle interactions and the geometry of the ensemble. However, the variability in the particle arrangement that one can obtain through those particle self-assemblies is very limited as compared to that achieved by physical lithographies that offer a plethora of possibilities to shape and organize the nanostructures, taking advantage of the interparticle interactions to enhance the plasmonic response. For instance, having nanostructures with sharp corners and very small gaps between them that give rise to hotspots with large enhancement of the electric field is highly desirable for certain applications in plasmonics.

2.2. Nanofabrication: lithographic techniques

Lithography (from the Greek ‘lithos’ (stone) and ‘graphia’ (write)) is the art and science of producing a pattern on a substrate. These techniques, nowadays widely applied in semiconductor manufacturing, include a wide range of methods such as optical lithography or photolithography, electron beam lithography, and imprint lithography. All of them share the following general procedure: a substrate, that can be covered by a thin film, a stack of films or a functional material, is coated with a resist layer, and then patterned either by exposition of the resist layer (to light, electron or ion- beams) or by application of pressure to it, and further developing and etching.¹

2.2.1. Photolithography

Photolithography is a classical approach, well established in semiconductor industry, to manufacture large areas of plasmonic nanostructure arrays inexpensively.

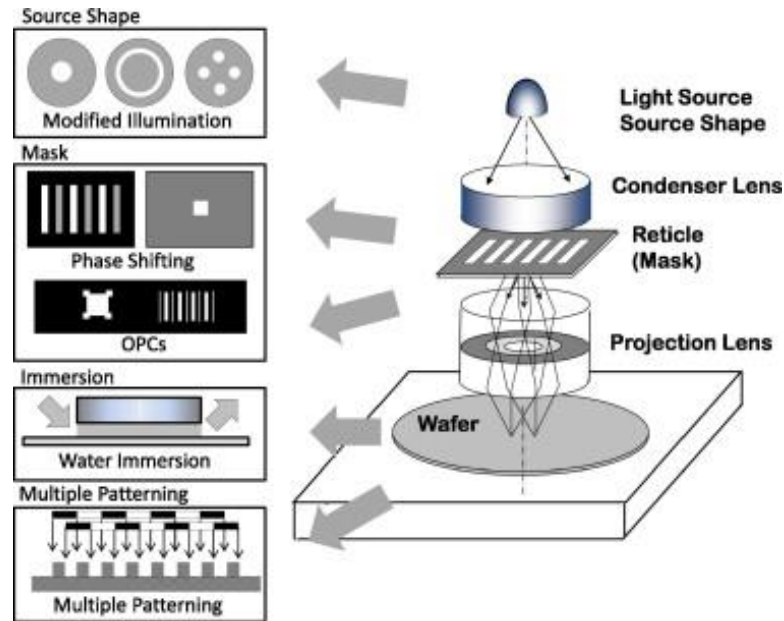


Figure 2.1 Scheme of the projection optical system and the parts where various resolution enhancement technologies can be applied. Reprinted from Ref. 2.

The aim of this technique is to create a pattern by means of light and a mask with the desired pattern, which are used to expose a resist layer previously deposited on the substrate. There are three modes of photolithography: contact printing, proximity printing, and projection printing. In the first two modes, the mask is in close proximity to the resist in such a way that the resolution is limited to a few micrometers. Usually, a projection optical system is used so that the mask can be larger than the final pattern, typically four times larger (see Figure 2.1). Then, the photoresist is exposed to an intense beam of light that goes through the mask, yielding a chemical change in the exposed areas. After exposition, the resist becomes soluble in the developer, in such a way that it is selectively removed from specific areas so that the desired pattern within the resist layer is obtained on top of the substrate.³

Whereas other lithographies struggle to face challenges such as throughput, yield or cost, optical lithography's main challenge is to improve its resolution, which is limited by light diffraction. The optical resolution limit for far field (Fraunhofer) diffraction is given by the Rayleigh's formula. Therefore, the

minimum achievable linewidth, LW , and the corresponding depth of focus, DOF , are:

$$LW = k_1 \cdot \lambda / NA$$

$$DOF = k_2 \cdot \lambda / NA$$

where k_1 and k_2 are constants that depend on the resist, the process and the image-formation technique, λ is the exposure wavelength, and NA is the numerical aperture of the projection lens defined as $NA = n \sin \theta$, being n the refractive index of the medium above the resist and θ the largest angle of converging rays subtended from the resist.¹⁴ Hence, to improve resolution, one can either reduce the wavelength of the incident light, the parameter k or increase the numerical aperture.

The wavelength is determined by the type of light source (see Figure 2.2). Until the late 1980s, high-pressure Hg discharge lamps with different working wavelengths (436 nm for the g-line, 405 nm for the h-line and 365 nm for the i-line) were used. These ultraviolet (UV) wavelengths have been the most used for decades in the semiconductor industry and other industries that require patterns above 300 nm such as flat screens televisions.⁵ Later, Hg discharge lamps were used to reduce the wavelength to approximately 250 nm, that were soon replaced by powerful monochromatic excimer lasers such as krypton fluoride (248 nm) or argon fluoride (193 nm) going to deep UV wavelengths.⁴ At 193 nm, the difficulties increased: thin transparent films or pellicles were used to protect the photomask from particulate contamination, and new photoresists were developed due to the increasing unacceptable photochemical darkening of the resist for the increasingly smaller wavelengths. A significant effort was made to further reduce the wavelength using fluorine lasers (157 nm), however, this evolution only encountered even worse difficulties: lack of organic pellicles, slow progress in new photoresists, availability and cost of the lenses due to the opacity of quartz at 157 nm, etc.⁵

shifting masks, and optical proximity corrections to lower the k factors (see Figure 2.1). For instance, k_1 has been reduced from approximately 0.8 to 0.4 since the 1980s. However, this comes at the expense of a dramatic increase in the cost of the technique, in turn limiting the use of the high-resolution photolithography to only highly demanding applications.⁴

To sum up, although photolithography allows for large-scale production, it may not be the most appropriate technique for plasmonics as it is still only cost-effective for structures over half a micron, still too big for many practical purposes. More complex approaches, such as the combination of a 193 nm light source with the immersion procedure, the double patterning, and the phase-shifting can achieve resolutions below 50 nm. However, this sophisticated method rises the price of the writing tool to be of the order of \$10M, plus the cost of the specific mask, that increases quickly as the size of the patterned features is reduced.⁶

Extreme UV (EUV) lithography, using a wavelength of 13.4 nm, seems to be promising. It is currently under development in several companies (Intel, Globalfoundries, Samsung and TSMC)⁷⁻⁹ and starting with volume manufacturing.⁸ In fact, the challenges of 3-nm and 5-nm node are already being analyzed.^{7,8}

2.2.2. Direct writing techniques

It is also possible to directly draw the desired pattern onto a resist layer instead of employing a mask for the exposition as in the case of optical lithography. Even though a focused light beam can be used to selectively expose a photoresist with the desired pattern, in order to achieve higher resolution, these maskless lithographies commonly use either electron or ion beams with shorter wavelengths.

Direct laser writing

An emerging tool for manufacturing 3D structures of interest for photonics is based on direct laser writing (DLW) where the laser beam is monitored focusing it along the three dimensions to "draw" the 3D design (see Figure 2.3). A beam of an ultra-fast laser, which is highly focused inside the volume of a transparent material with photoreactive monomers, produces the absorption of photons, causing a local polymerization. However, the linear absorption of the electromagnetic radiation by the monomer for polymerization limits both the resolution of the technique to the wavelength of light and the penetration depth into the material due to the strong linear absorption. Multi-photon absorption can be used as an alternative method.^{10,11}

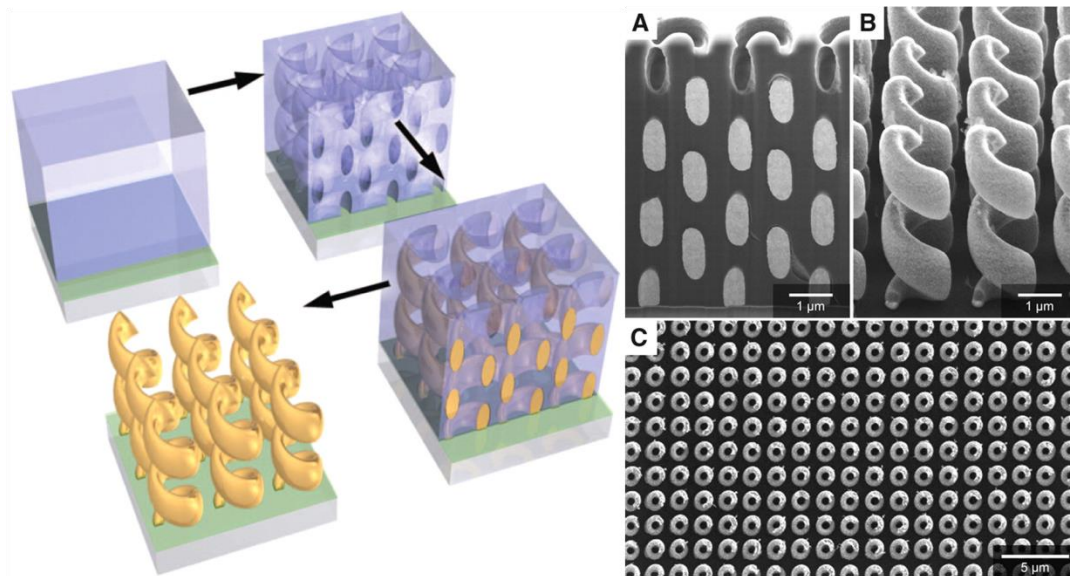


Figure 2.3 Scheme of direct laser writing (left): DLW is used in combination with plating to pattern 3D free-standing Au helices. (right) Scanning Electron Microscopy (SEM) micrographs showing (a) a Focused Ion Beam (FIB) cut of the structures (b) an oblique view and (c) a top view. Adapted from Ref. 12.

Two-photon absorption (TPA) is defined as the simultaneous absorption of two photons of identical or different frequencies to excite one molecule from its ground state to a higher state, being those two states separated in energy by the sum of the energies of the two photons. As it is a second-order process, its

strength depends on the square of the light intensity, being much weaker than the linear absorption. If the laser is focused using a lens with high NA , the TPA will only take place nearby the focal point, in a small region that can be less than 1 μm in size. These can be extended to more complex processes including the absorption of more photons.¹¹

The material used for TPA is commonly composed of a monomer or mixture of monomers and oligomers that will form the final polymer, and a photoinitiator that will absorb light and provide the active species for the photopolymerization. Both the monomer and the photoinitiator have to be transparent to the laser wavelength and the monomer must be also transparent to the TPA wavelength, while the photoinitiator should have a high absorption cross section for this wavelength.¹⁰

Electron beam lithography

Proposed in 1936 for microscopy, the use of accelerated electrons of 100 KeV offers a source of radiation of 3.9 pm in wavelength (without considering relativistic corrections).

Electron beam lithography (EBL) was first reported in 1960 and uses the accelerated electrons to directly write the desired pattern in an electron sensitive resist. For positive tone resists, such as polymethyl methacrylate (PMMA), long chain polymers are broken into smaller pieces by the action of the beam, becoming more soluble in the developer; while in negative tone resists, for example hydrogen silsesquioxane (HSQ), smaller polymers are cross-linked by the action of the beam, creating larger polymer chains with reduced solubility. After the exposure, the resist is immersed in the developer either to dissolve the fragments, in the case of positive resist, or the non-cross-linked molecules, for negative tone resists. Then, the pattern can be transferred to the substrate using either an etching process or a lift-off process which consists in metallizing the whole sample and then removing the undesired metal areas by

dipping the sample in an appropriate solvent to dissolve the remaining resist^{6,13,14}

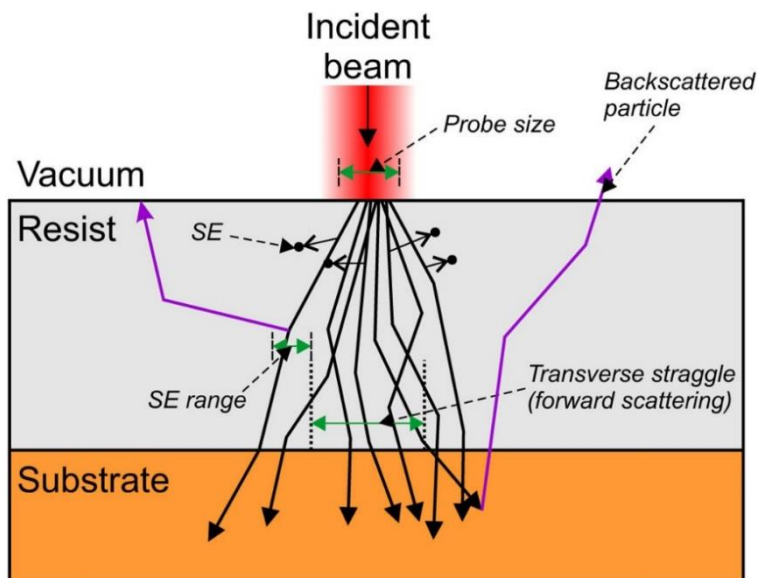


Figure 2.4 A schematic representation of the interactions between the electron beam and the resist layer on a substrate. Reprinted from Ref. 3.

Electrons are typically produced by thermal or field emission from a fine filament, and they are accelerated and focused on the sample via EM lenses. The size of the beam can be smaller than 1 nm for the most advanced setups and of a few nm for normal ones.¹³⁻¹⁵ Here, the diffraction limit is no longer a problem, and the resolution is limited by the lens aberrations, the quality of the resist, the substrate, and the processing conditions (energy, dose, development time, and temperature). The final resolution of the pattern is affected by the dispersion of the electrons due to diverse interactions (see Figure 2.4) as well as the collapse of the patterns due to swelling and capillary forces, or the size inhomogeneity of the patterned features (line edge roughness).¹³

The electron column is in vacuum to minimize gas scattering of the beam. However, electrostatic repulsion among electrons widens the beam, which is a problem that worsens with higher currents and lower energies. Besides, when electrons go inside the resist layer, they start to collide, resulting in an additional beam broadening at lower energies and for thicker resist layers.

Moreover, electrons that reach the substrate can be backscattered giving rise to exposure of undesired regions, causing pattern distortion and overexposure. This so-called proximity effect can be minimized by using thin membranes as substrates. Finally, although secondary electrons, produced by inelastic collisions of the primary electrons, have low energy and are only short range (some nm) so their effect can be negligible for a distance over 10 nm, they indeed could ultimately limit the highest achievable resolution of EBL.^{6,13}

It is also worth noting that electrostatic charging may be a serious drawback in this kind of lithography, especially for non-conductive substrates where the charge builds-up may cause beam deflection due to the absence of a mean to dissipate the absorbed electrons. There are several approaches to overcome this problem. A thin metallic layer on top of the resist that can be removed via chemical etching prior to the development process is one of the alternatives; however, this metallic film can result in electron beam scattering that decreases sensitivity. Another option is to coat the substrate with a thin metallic layer that can also be used as mask for a later etching step but sometimes this layer is not desired. Moreover, it is also possible to spin-coat a conductive polymer on top of the resist to avoid the charging effects, which reduces the broadening of the beam as compared to metallic layers, thus offering a better resolution.^{6,13}

Depending on the resist, the equipment, and the substrate, structures of even less than 10 nm can be obtained. The throughput is smaller than in optical lithography but it has the advantage of not needing the use of a mask. This type of lithography is mainly applied to the fabrication of photolithography masks and reticles, and to prototyping. In plasmonics, EBL is a reliable technique for manufacturing structures with small features such as metallic nanogaps or sharp structures that lead to hotspots.

Focused ion beam

In a similar way to EBL, Focused Ion Beam (FIB) uses an ion source instead of electrons to write the pattern. As in the case of field emission electron beams,

loosely bound atoms are ionized by large localized electric fields and accelerated towards the sample through electrostatic lenses that focus the beam. The larger mass of these ions as compared to electrons leads to shorter wavelengths and smaller scattering inside the resist film, yielding an improved resolution that can go below 10 nm.^{6,16}

FIB can also be used for direct patterning: the ions reaching the surface can either mill away material following a predefined pattern (ion-milling) or deposit a metal through the ion-beam aided decomposition of a precursor gas previously placed in the chamber.

FIB is often used in industry to repair defects or for prototyping. It is widely used in plasmonics to drill holes or slots in continuous metal films. For instance, sub-5 nm holes have already been obtained with this technique that has also been used to build antennas at the apex of Scanning Near-field Optical Microscopy (SNOM) tips.⁶

Dip pen lithography

Scanning Probe Lithography emerged in the late 1980s and comprises several approaches (near field optical lithography, scanning tunneling microscopy or atomic force microscopy), all of them having in common the use of a sharp scanning probe to produce local modifications (heat, scratch, oxidation or substance transfer) on a surface.¹⁷ One of the most suitable techniques for plasmonic applications among them is dip pen nanolithography (DPN), where an ink-coated Atomic Force Microscopy (AFM) tip is used to draw on a surface. It can also be combined with surface chemistry to locally link metallic particles to the substrate. Even though its main drawback is the difficulty to scale up, parallel arrays of probes have been used to create large patterns without the need of a mask.^{3,6,18}

Other techniques such as focused ion and electron beam induced deposition have hardly been applied to manufacture plasmonic structures in part by the

limited availability of gas precursors, in spite of the fact that they have proven to be useful for the preparation of complex chiral structures such as helices.^{19,20} Laser ablation can also be considered as a direct write technique; however, it is again limited by diffraction making its use very limited for plasmonics.

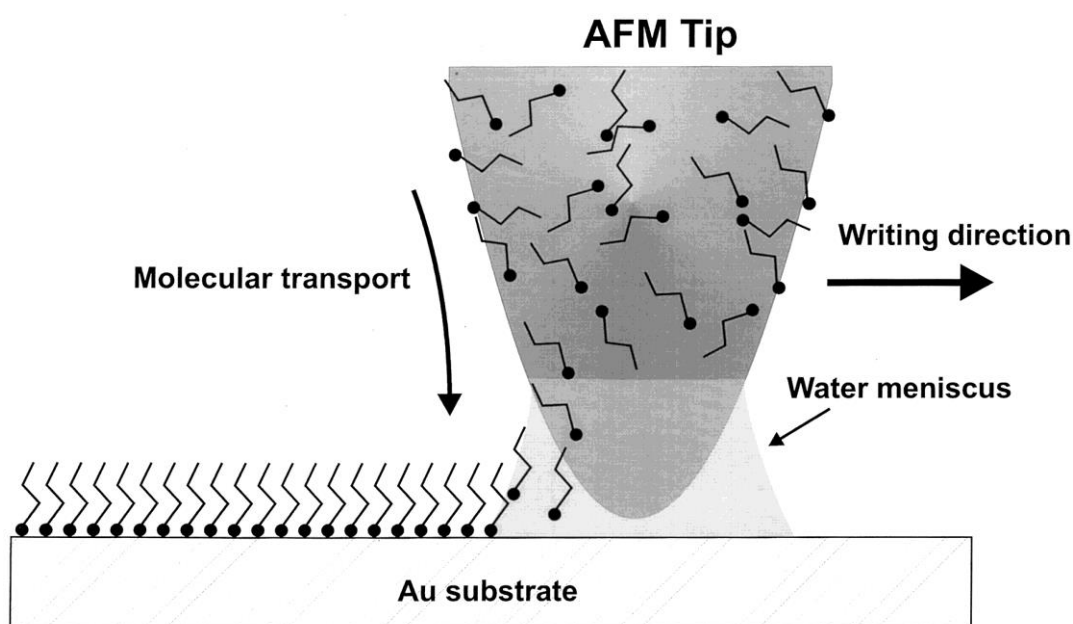


Figure 2.5 Scheme of DPN: a water meniscus forms between the AFM tip coated with the molecule ink and the substrate. Reprinted from Ref. 18.

2.2.3. Soft lithographies

Soft lithographies include a variety of techniques that use organic ('soft') compounds to enable replication and pattern transfer. They are based on three steps: (a) fabricating a patterned master; (b) molding this master to generate a patterned stamp, and (c) generating a replica or a 1:1 projection of the pattern on a surface by applying the stamp. The stamp is usually manufactured by conventional lithographic tools and can be used to produce many molds and replicas from the same master.

Embossing and nanoimprinting

Nanoimprint lithography (NIL) and hot embossing are high resolution parallel patterning methods commonly used to go beyond photolithography's resolution limit or when e-beam throughput is not enough. The basics of these techniques are to replicate the pattern from a stamp by mechanical contact onto a material where one wants to create the pattern thanks to the difference between the mechanical properties of the material and the mold. This can be done following different approaches such as patterning a liquid by pouring it in a mold that is later cured with UV-light, or heating a thermoplastic material above the glass transition to pattern it and then cooling it down. These patterns can later be transferred to the substrate or an underlying film by etching. These techniques offer resolutions below the 20 nm and high throughput.²¹

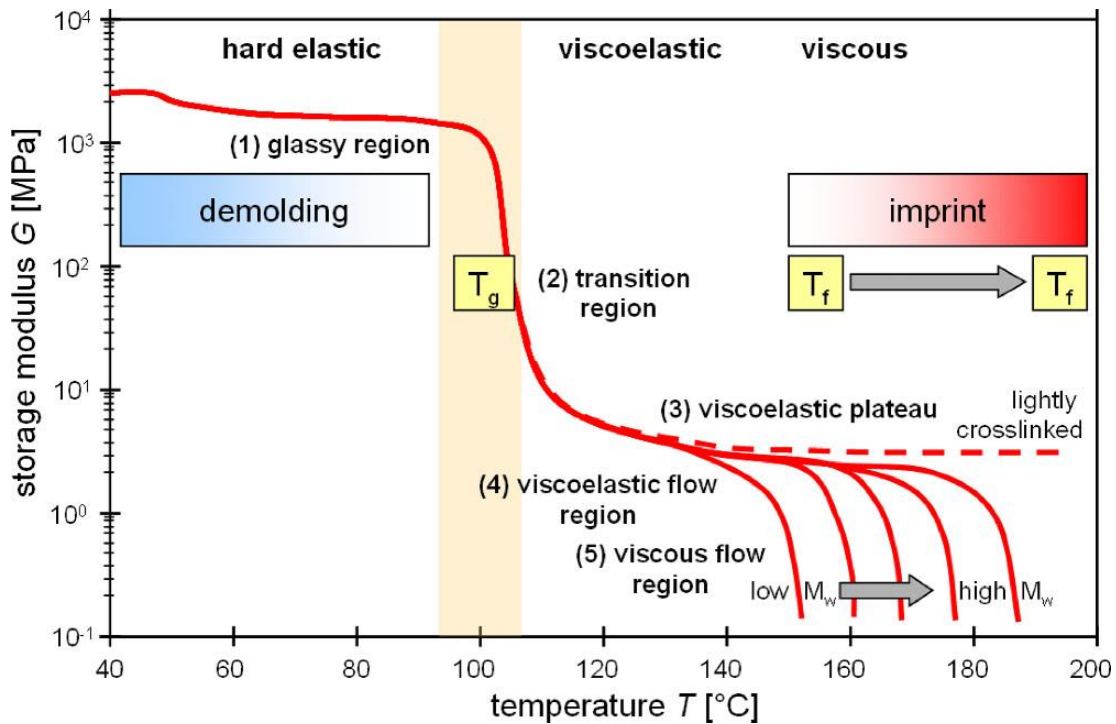


Figure 2.6 Scheme of the mechanical properties for polymers with a glass transition temperature (T_g) around 100°C for normal process conditions showing the effect of different molecular weights (M_w). Notice the drop of G at T_g (thermomechanical properties between stamp and polymer become sufficiently different for repeated molding) and T_f (temperature at which viscosity drops to the needed values for imprint). Reprinted from Ref. 22.

Thermal NIL uses thermoplastic materials whose viscosity changes drastically within tens of degrees making it possible to easily change its state from solid to viscous in a reversible manner (see Figure 2.6). Along the process, the material is heated 60-80°C above the glass transition temperature (T_g). Then, the stamp is pressed against the material with a pressure on the order of 20-100 Pa, forcing the displacement of the viscous material into the cavities of the mold. When the patterns are transferred to the thermoplastic material, the latter is cooled down while the pressure is maintained to keep the pattern. Once below T_g , the material becomes hard again and the mold can be detached. The most expensive part of this procedure is the fabrication of the master mold. However, this mold can be reused a lot of times.^{3,5,21-24}

Care should be taken when choosing the appropriate polymer since its molecular weight (M_w) will play a key role on determining both T_g and the final mechanical properties such as the stiffness, strength, and the viscosity. A widely used polymer both in NIL and EBL is PMMA, that can be found in different molecular weights. For EBL, higher M_w are desirable as they produce a higher contrast between the exposed and unexposed regions. However, shorter polymer chains are more suitable for NIL, usually some tens of kg/mol as compared to over 500 kg/mol for EBL. The reason for that is two-fold: firstly, shorter chains are expected to have higher mobility to fill the cavities in the mold. Secondly, with increasing M_w there is also an increase in the dependence of viscosity with temperature. Besides, T_g (around 105°C) is low enough for shorter chains to enable performing thermal NIL below 200°C but high enough to ensure the endurance of the hard phase of the polymer during the etching process.^{21,22,25}

2.2.4. Lithographies based on self-assembly

Whereas the previously addressed methods rely on the use of a mask or on controlled scanning with a beam or a tip, here, a set of lithographies based on self-assembly phenomena in different physical systems are commented.³

Colloidal or nanosphere lithography

This is a high-throughput, cost effective and large-scale, compatible technique that has been widely used for plasmonics, especially for Surface Enhanced Raman Spectroscopy (SERS). This method combines the advantages of both top-down (due to the use of structured layers) and bottom-up (due to the self-assembly of particles) fabrication techniques.^{6,17,26}

Here, a flat substrate is coated with a suspension of monodisperse spherical colloids, typically polystyrene or silica spheres after a chemical treatment to enhance hydrophilicity. Upon drying by thermal or laser pulse deposition, they self-assemble in a hexagonal-closed-packed (hcp) monolayer or bilayer called colloidal crystal mask. This mask is used to selectively pattern the substrate by depositing the desired material through the interstices of the ordered spheres. Then, the mask is removed by sonication or stripping leaving an array of ordered structures on the substrate. Annealing is sometimes used to crystallize the sample or induce a crystallographic phase transition.^{10,17,27,28}

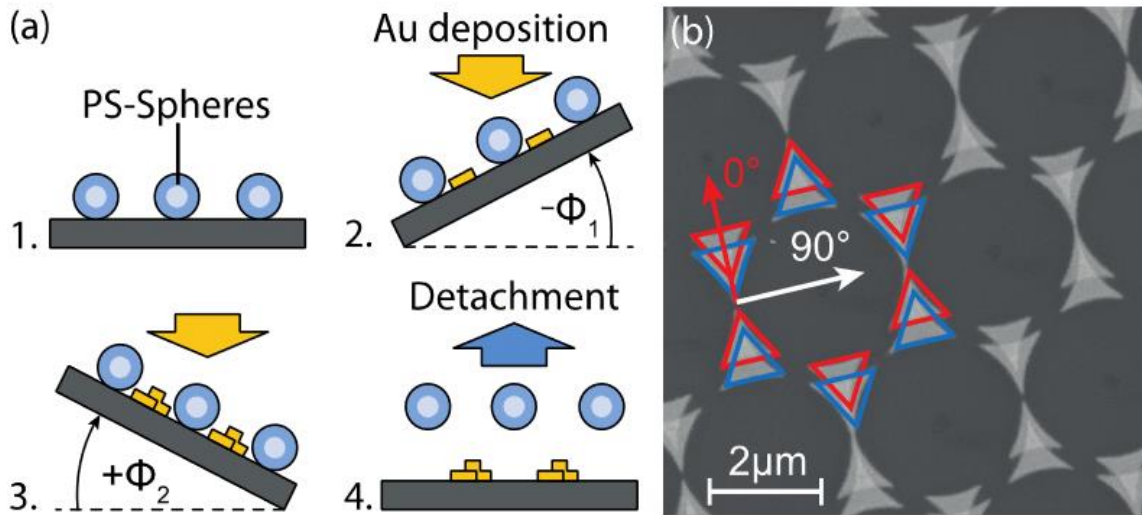


Figure 2.7 A modification of the typical normal metallization to obtain double triangles is shown here.(a) Scheme of the fabrication process: 1. Nanosphere deposition; 2. Metallization with tilt angle $-\Phi_1$;3. Metallization with tilt angle Φ_2 ; 4. Removal of the spheres. (b) SEM micrograph showing the resulting structures for tilt angles -5° and 5° . Reprinted from Ref. 29.

Holes can also be drilled in the substrate by modifying the general process adding etching or heating treatments. Nanorods, nanowires, nanopillars and nanotips can also be manufactured by catalytic deposition and overlapping structures, nanogaps and chains by the use of angle-resolved nanosphere lithography (see Figure 2.7).^{17,28,29}

Nanosphere lithography offers, therefore, the chance to produce nano-objects in large ordered arrays, with a controlled density and a certain flexibility to choose the material of both the substrate and the nanostructures, being its main drawback the fact that the resulting pattern is limited to hexagonal lattices.¹⁷

Block copolymers

Patterning of nanometric features can also be done using block copolymers (BCPs), a polymer with two or more different chemical blocks strongly bonded to each other.

Directed self-assembly of block copolymers combines a lithographic tool with the ability of BCPs to self-assemble. Two approaches can be used to control the orientation and alignment of the BCPs: (i) graphoepitaxy, in which a topographical pattern (i.e. trenches or holes) is created, for example, via EBL; and (ii) chemical epitaxy, in which chemical patterns, instead of topography, are used to guide the assembly, based on the fact that the modified areas present a larger affinity to one of the blocks. Then, this assemble can be used to create nanometric patterns, for example, by selectively removing one of the blocks via etching and transferring the patterns to an underlying material, reaching feature sizes on the order of a few nm.^{26,30}

Although still not very extended, some works have proved the usefulness of BCPs in the field of plasmonics.³¹⁻³³

2.3. Nanofabrication for plasmonics: special issues to solve

One typical problem in plasmonic applications is related to the poor adhesion of metals, especially to oxide substrates. Ti and Cr are common materials to promote adhesion, which is proved by AFM measurements. However, the use of Cr and Ti has strong effects on the plasmonic response of the nanostructures, showing visible effects even for 1 nm thick layers.^{6,34,35} The use of Cr and Ti oxides seems to be a better option, since the damping of the resonance is lower and the fluorescence enhancement, when occurring, is less affected. Besides, different groups are studying other possibilities to circumvent this problem.^{36,37}

Dissipative loss is one of the problems to overcome, as it is even further increased by the surface roughness that appears especially for the case of e-beam or sputtering metallization. Metals such as Au and Ag are the most widely used materials thanks to their small ohmic losses and their high DC conductivity.

Related to this, there is another crucial aspect: the crystallinity of the deposited materials. While chemical synthesis can provide crystalline structures, the films deposited by sputtering or e-beam evaporation show a granular structure.^{6,38} Ditlbacher *et al.* compared the results for a crystalline silver nanowire synthesized by a chemical route to an analogue one manufactured by EBL that showed surface roughness and poly-crystallinity, proving the importance of highly crystalline structures for having large surface plasmon propagation lengths.³⁹ To circumvent these difficulties, different approaches have been proposed. For example, Bosman *et al.* used encapsulation of EBL patterned nanostructures with HSQ to thermally anneal the sample, what gave rise to reduced grain boundaries while shape was preserved, resulting in Q-factors of the structures comparable to those of single crystals.³⁸ Self-assembling chemically synthesized nanoparticles in lithographed traps is another approach, as shown by Flauraud *et al.*⁴⁰

Last but not least, there is the issue of material compatibility with existing processes such as complementary metal-oxide-semiconductor (CMOS) technology.⁶

2.4. Characterization of plasmonic nanostructures

To be able to optimize their response, plasmonic nanostructures should be characterized geometrically and optically. To perform their structural characterization, the most spread techniques that allow for nanometer resolution are AFM, Scanning Electron Microscopy (SEM) and Transmission Electron Microscopy (TEM).

However, the optical characterization can be somehow challenging due to limitations imposed by the diffraction limit. Here, some of the most widely used techniques will be described briefly, classifying them in two big groups depending on which optical regime they operate: far-field or near-field.

2.4.1. Far-field characterization

Traditional techniques based on far-field configurations consisted in analyzing the absorption and extinction that the sample caused in the incident beam by collecting either the transmitted or the reflected light. In these techniques, the image of the particles or molecules appear darker than the bright background and that is the reason why they are known as bright-field methods. However, when a conventional bright-field microscope is applied to the study of nanometer particles, that provoke a very small effect in the total absorbed or reflected light, the obtained contrast is usually very small even with modern detectors and light sources. To improve this contrast, scattered light is usually studied with different set-ups designed to block the incident light.

Dark-field microscopy

The fundamental idea behind dark field techniques relies on the fact that the incident beam is somehow blocked and only an outer ring of illumination is left.

The scattered light is collected to form the image while the transmitted or reflected light is not. Nanoparticles or nanostructures appear bright in the image against a dark background, hence the name of dark-field. Therefore, better resolution than for bright field microscopy can be achieved thanks to the improvement in the signal-to-noise ratio.

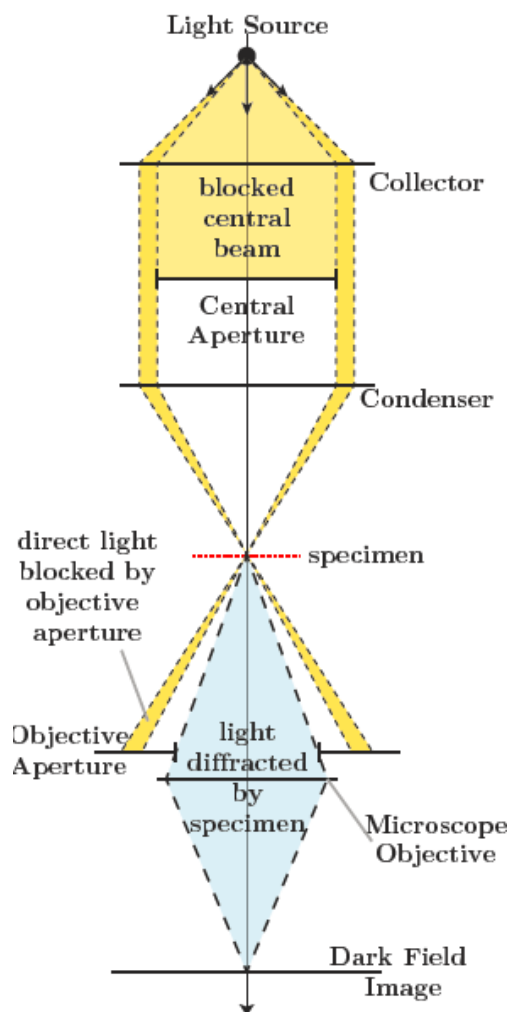


Figure 2.8 Configuration of a dark-field microscope. Reprinted from Ref. 41.

This idea was first exploited by Richard Zsigmondy, who was awarded the Nobel Prize in Chemistry in 1925 for giving the idea that led to the invention of the ultramicroscope to characterize the aggregation of colloidal nanoparticles in solution by analyzing the changes in the dark-field scattering spectrum.

Nowadays, this technique is extensively used for imaging as well as for several spectroscopies.⁴²

FTIR spectroscopy

Fourier transform infrared (FTIR) spectroscopy is based on the use of a Michelson interferometer in which the coherent incident beam is split into two equal parts by a beam splitter. One half is reflected to a fixed mirror and the other one is transmitted to a movable mirror. The beams are later recombined after introducing a small difference in their optical path to create an interference pattern (see Figure 2.9). The resulting signal is called interferogram and contains information coded at each frequency, meaning that the whole range of frequencies is analyzed at once, resulting in really fast measurements.

An incident light beam is impinging on the sample and transmitted (or reflected) light is collected by an optical microscope coupled to a Fourier transform spectrometer that analyzes the difference in intensity as a function of the mirror position (*i.e.*, the optical path difference). Thus, the transmission or reflection spectra normalized to a reference measurement which is usually taken from a bare transparent substrate (e. g. glass) background for transmission, and a mirror (Ag or Au) for reflection, are obtained through the Fourier transform of the interferogram.

The spectral resolution is determined by the retardation of the moving mirror within the Michelson interferometer: to double the resolution, the mirror needs to be moved twice the original distance.^{43,44}

One of the advantages that FTIR presents is its multiplex character: each sampling contains information from all the wavelengths of the incoming light as compared to traditional dispersive instruments where each measurement point corresponds to a single wavelength. Another advantage is the absence of slits in the optical path that allows more light to reach the detector improving the signal to noise ratio.

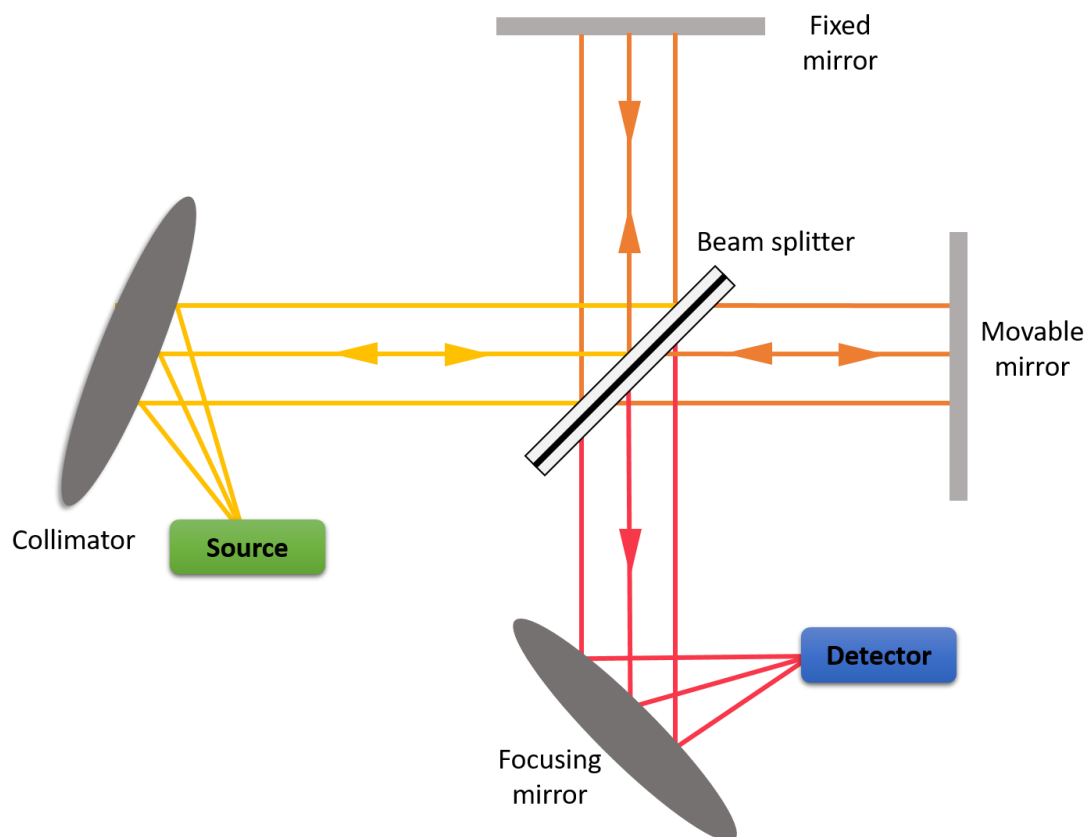


Figure 2.9 Schematic diagram of a Michelson interferometer configured for FTIR spectroscopy.

2.4.2. Near-field characterization

Near-field optics uses light emerging from a subwavelength aperture or scattered by a subwavelength metallic tip or nanoparticle that shines on an object placed in close vicinity ($<$ wavelength) of the subwavelength light source. It is worth noting that light in the near-field regime has a non-propagating, evanescent character that is associated with an electric field showing quick exponential decay with the distance from the subwavelength source.

Near-field characterization benefits from the existence of evanescent waves at the interfaces between the metal and the dielectric, that is, they exploit the ability to concentrate the light in the close vicinity of the metal surface, achieving resolutions below 100 nm. To overcome Abbe's diffraction limit, Synge proposed in 1928 the use of the near-field regime of light for imaging.⁴⁵

However, the implementation was not easy as it needs nm accuracy actuators capable of moving sensors a few nm from the sample and the first use of a near-field microscope was in 1972 by E. A. Ash and G. Nicholls who reached a resolution better than $\lambda/60$. The first optical image was recorded at IBM in 1984 by D. W. Pohl and coworkers and the first IR image came out in 1986 recorded by G. A. Massey.¹⁰

SNOM

The most widely used probe consists in a very small optical tapered fiber in the form of a tip which is coated on the outside with a reflective aluminum layer. Light propagating through this tip may yield an optical resolution only limited by both the size of the aperture on the apex of the tip (typically around 50 nm) and the distance from the sample. An image is obtained by scanning the tip along the sample; hence the name of near-field scanning optical microscopy or scanning near-field optical microscopy (SNOM).

The SNOM takes advantage of the evanescent electric field that exists around the tip to produce the optical excitation of very localized areas of the sample. These evanescent fields carry high frequency spatial information and decay exponentially with the distance from the tip. Therefore, it is necessary to place the sample in the near-field region of an evanescent light source and collect the scattered light to form an image. The local probe ensures a confined photon flux between the probe and the sample surface.

2.5. Applications

The ability of plasmonic nanostructures to confine optical energy in subwavelength volumes has been exploited for applications like bio-sensing,⁴⁶⁻⁴⁹ non-linear optics⁵⁰⁻⁵² or solar energy harvesting,^{53,54} where the efficiency is increased thanks to the extreme localization of the electromagnetic fields, or in optical elements, interconnects or chips where the strong confinement offers the possibility to obtain dense packing and reduce the size.

Localized surface plasmon resonance (LSPR) strongly depends on the refractive index of the embedding medium. Hence, it has been used for colorimetric plasmonic sensors. Also, the strong localization of the EM field around metallic nanostructures, that extends into the surrounding medium (around 30 nm) and decays exponentially (for the dipole approximation), has been used to enhance optical processes such as plasmon-enhanced fluorescence, surface-enhanced Raman scattering or surface-enhanced infrared spectroscopy.⁴⁷

2.5.1. Sensing

Plasmonic nanoparticles have been exploited as platforms for sensing in different ways (analytes in environmental monitoring, homeland security, biomedicine...). On the one hand, the fact that SPR depends strongly on the refractive index of the embedding medium has been used in SPR sensors, where the change in the refractive index is detected as a shift in the resonance. On the other hand, the enhancement of the EM field is used to increase the efficiency of optical processes, which are usually very inefficient, for example in spectroscopies such as Raman, fluorescence or IR.

The high sensitivity of LSPR has also been used to design the so-called plasmonic molecular rulers, which are based on the strong dependence of the optical response to the distance between coupled particles. This effect is applied to measure label-free, both the size and structure of biomolecules, or to observe binding processes in real time.⁵⁵

SPR sensing

Here, the sensor is based on the frequency shift of the plasmon resonance to act as a transducer of the sensing signal. Both SPP and LSP can be exploited. The wavelength of the SPR peak varies linearly with the refractive index of the surrounding medium according to the Drude model and the sensitivity, S , of the sensor ($S = \Delta\lambda_p/\Delta n$, where λ_p is the plasmon resonance wavelength and n the refractive index of the medium) can be expressed in units of nm per Refractive

Index Unit (RIU). To evaluate the performance of the sensor, a figure of merit, FOM, defined as $FOM = S/FWHM$ can be calculated, where $FWHM$ stands for full width at half-maximum of the SPR peak. We can find chip-based or colloidal based sensors, that rely on the same physical principle.^{46,47}

To enhance the optical response, the peak of the plasmonic element can be overlapped to the absorption band of the chromophore that binds to the metal.^{46,47}

This type of sensor offers label-free detection (eliminating the need of different antibodies like in enzyme-linked immunoabsorbent assay, ELISA) and real-time measurement of reaction kinetics to study binding events.^{46,47}

Plasmon-enhanced fluorescence sensors

Plasmon-enhanced fluorescence sensors use fluorophore labels coupled with the highly confined fields of surface plasmons (SP), an interaction that can be engineered to enhance emitted fluorescence light allowing for improved detection limit and shorter analysis time.

The coupling between plasmons and fluorophores can happen at the fluorophores absorption and emission wavelengths, altering their transitions between the ground state and the higher excited states.⁵⁶ The fluorophores have long-lived excited states (nanoseconds) that radiate strongly after thermal relaxation, while the plasmon relaxes almost instantaneously. The energy transfer between plasmons and fluorophores is dominated by dipole-dipole interactions and is determined by the separation distance. When the separation is below 10 nm, the non-radiative field of one dipole can excite the surrounding ones, phenomenon which is known as Förster resonance energy transfer (FRET), and has an efficiency given by:

$$Eff_{FRET} = \frac{1}{1 + \left(\frac{R}{R_0}\right)^6}$$

being R the separation distance and R_0 a factor that depends on the spectral overlap between the donor's excited state and the acceptor's ground state absorption.

The second enhancement possibility is through the Purcell effect: if a radiative dipole is located within a resonant cavity, the emission intensity is amplified on-resonance and quenched off-resonance because the cavity modifies the local density of optical states (LDOS):⁴⁷

$$\rho_{LDOS}(\omega) \sim |E_{loc}(\omega)|^2$$

where $|E_{loc}(\omega)|^2$ is the local electric field of the cavity normalized to the incoming intensity.

The overlap between the plasmon and the fluorophore determines which of the two effects is actually present and whether it leads to either enhancement or quenching of the signal. If the plasmon overlaps with the fluorophore's absorption, the excitation rate will be enhanced. For small metallic nanoparticles where absorption dominates, fluorescence will be enhanced through FRET. For larger particles which mainly behave as scattering centers, FRET will be possible at small distances (around 10 nm) and Purcell effect at longer distances (10-50 nm). Purcell enhancement for the plasmon's radiation is usually negligible because the LDOS of the fluorophore is negligible. Hence, the enhancement is primarily coming from FRET at distances of few nm. If the plasmon overlaps with the fluorophore's emission, enhancement or quenching is possible. If the fluorophore is within a few nm of the plasmon, the signal will be quenched through FRET. At longer distances, a strong enhancement thanks to Purcell effect may happen.⁴⁷

Enhancement factors through this effect over 1000 have been reported.⁵⁶

Surface enhanced infrared absorption (SEIRA)

Surface enhanced infrared absorption (SEIRA) and, in particular, on-resonance SEIRA, is a key tool for detecting molecules even down to single-

molecule detection, since most molecules have their characteristic absorption bands in the mid-IR region of the spectrum. However, the molecular absorption cross-sections of mid-infrared vibrations are very low (of the order of 10^{-20} cm²), requiring large amounts of material for their effective detection. Discovered in 1980, the presence of a thin film of Ag nanoparticles with plasmonic resonances in the visible gives rise to an enhancement by a factor of 20 of the infrared vibrations of the molecular film beneath the nanoparticles. However, this factor can be much bigger (approximately five orders of magnitude) when the resonances of the plasmonic nanoparticles are engineered to match the vibrational modes of the molecules to be detected.⁵⁷ This "resonant" SEIRA was first discovered by Neubrech *et al.* in 2008 and was applied to detect 50 attograms of analytes placed on a single nanoantenna.⁵⁸

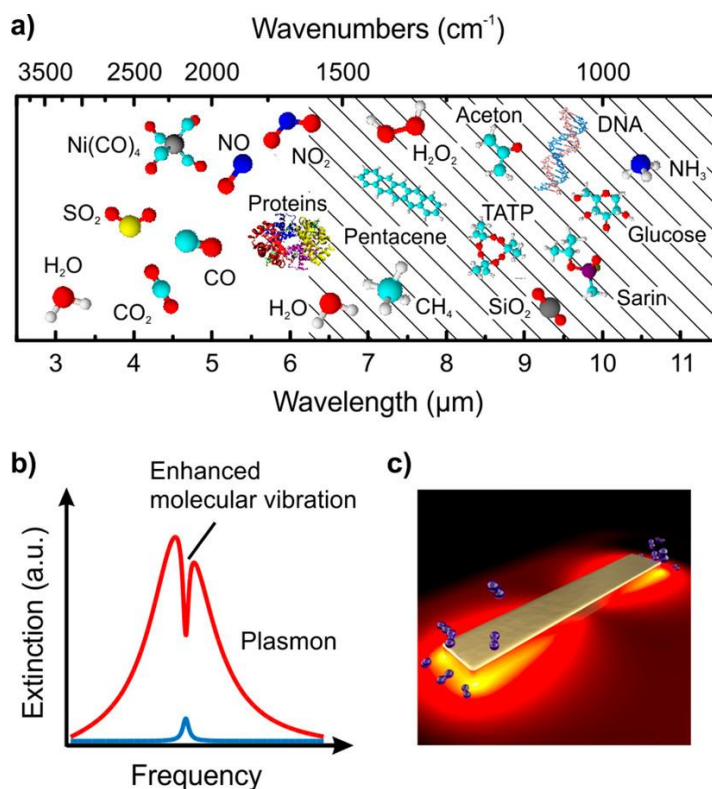


Figure 2.10 (a) Characteristic IR vibrations of some molecular species. The hatched part corresponds to the fingerprint region containing skeletal vibrations. (b,c) Resonant SEIRA: IR vibrations of molecules located in the enhanced electromagnetic near-field of a plasmonic nanoantenna are enhanced if the plasmon (red) is resonantly matched to the molecular vibration (blue). Reprinted from Ref. 57.

Surface enhanced Raman Spectroscopy (SERS)

SERS refers to the phenomenon in which the Raman scattering from molecules is enhanced thanks to the presence of metallic structures in close vicinity. The response is a "fingerprint" of the vibrational spectra of every molecule, providing a way for molecular identification.⁴⁷

The total enhancement in SERS comes from two contributions: the chemical and the EM enhancements of the signal. The first one may imply an increase in the rate of the conventional Raman scattering between one and two orders of magnitude and is related to the charge transfer between the adsorbed molecules and the metallic structures. However, the second contribution is by far the most important one and its effect may increase the conventional Raman scattering rate by a factor as large as 10^8 . This outstanding effect is associated with the large enhancement of the electric field in the vicinity of metallic nanostructures.

The enhancement factor of SERS ($EF_{SERS}(\lambda_{SERS})$) is given by the equation:⁵⁹

$$EF_{SERS}(\lambda_{SERS}) = |E_{out}(\lambda)|^2 |E_{out}(\lambda_s)|^2 / |E_0|^4$$

where E_0 is the incoming field, $E_{out}(\lambda)$ is the local field at the incoming wavelength λ , and $E_{out}(\lambda_s)$ the electric field at the scattered wavelength λ_s . Taking into account that $\Delta\lambda = \lambda_s - \lambda$ is usually much smaller than the linewidth of the surface plasmon mode, and therefore, $E_{out}(\lambda)^2 \approx E_{out}(\lambda_s)^2$, the previous equation can be approximated to:

$$EF_{SERS}(\lambda_{SERS}) = |E_{out}(\lambda)|^4 / |E_0|^4$$

SERS offers the advantages of being a tool for detecting a unique spectral signal of the analyte without interference with water, easy sample preparation, multiplex detection with a single excitation laser, high throughput, and ease to implement in point-of-care applications with single-molecule sensitivity. Thus, it is a technique widely used for bioapplications,⁵⁷ and manufacturing different substrates and plasmonic nanostructures for SERS is a very active field.⁴⁷

2.6. Conclusions, limitations and outlook

Along this chapter, some of the fabrication tools, the characterization techniques, and the applications, in particular those related to enhanced spectroscopies, have been covered. The thrilling development of plasmonics has been reflected in the emergence of an innumerable variety of techniques for the obtaining and the analyses of plasmonic nanostructures. The outlook in the field seems promising: thanks to the applications found in very different areas, plasmonics has attracted a lot of attention. However, realizing practical applications ready for commercialization is still an issue. Nowadays, only a few of companies are commercializing plasmonic products for sensing (Renishaw Diagnostics, Cabot Corporation, Causeway Sensors...). Nevertheless, experts in the field believe that the gap between research and industry will be soon overcome. Photo-thermal cancer treatment is in clinical trial. Several companies work on thermo-optical plasmonic modulators for Si photonics. Some experts foresee that we will soon see heat-assisted magnetic recording based on the fact that major magnetic recording companies like *Seagate* have already moved on their research activity to this new field and that it could be the major success of the field together with sensing.⁵⁷ Meanwhile, efforts in this research field will continue to grow, enabling eventually the transfer of knowledge that will make possible the appearance on the real market of a plethora of products based on plasmonic applications.

References

1. Ito, T. & Okazaki, S. Pushing the limits of lithography. *Nature* **406**, 1027–1031 (2000).
2. Okazaki, S. High resolution optical lithography or high throughput electron beam lithography: The technical struggle from the micro to the nano-fabrication evolution. *Microelectron. Eng.* **133**, 23–35 (2015).
3. Pimpin, A. & Srituravanich, W. Review on Micro- and Nanolithography Techniques and their Applications. *Eng. J.* **16**, 37–56 (2012).
4. Projection optical lithography. *Mater. Today* **8**, 18–24 (2005).
5. Robinson, A. P. G. & Lawson, R. *Materials and Processes for Next Generation Lithography. Frontiers of Nanoscience* **11**, (Elsevier, 2016).
6. Léron del, G., Kostcheev, S. & Plain, J. in *Springer Series in Optical Sciences* 269–316 (2012). doi:10.1007/978-3-642-28079-5_9
7. EUV Defects Cited in 5-nm Node | EE Times. Available at: https://www.eetimes.com/document.asp?doc_id=1333008. (Accessed: 31st May 2018)
8. NEW! 2017 Edition Reports - IEEE International Roadmap for Devices and Systems. Available at: <https://irds.ieee.org/roadmap-2017>. (Accessed: 31st May 2018)
9. Semiconductor Engineering ∴. The Race To 10/7nm. Available at: <https://semiengineering.com/racing-to-107nm/>. (Accessed: 31st May 2018)
10. Prasad, P. N. *Nanophotonics*. (Wiley, 2004).
11. Selimis, A., Mironov, V. & Farsari, M. Direct laser writing: Principles and materials for scaffold 3D printing. *Microelectronic Engineering* **132**, 83–89 (2014).
12. Gansel, J. K. *et al.* Gold helix photonic metamaterial as broadband circular polarizer. *Science* **325**, 1513–5 (2009).
13. Mohammad, M. A., Muhammad, M., Dew, S. K. & Stepanova, M. in *Nanofabrication* 11–41 (Springer Vienna, 2012). doi:10.1007/978-3-7091-0424-8_2

14. Bucknall, D. G. *Nanolithography and patterning techniques in microelectronics*. (Woodhead Publishing Limited, 2005). doi:10.1533/9781845690908
15. Utke, I., Moshkalev, S. & Russell, P. *Nanofabrication Using Focused Ion and Electron Beams: Principles and Applications*. (Oxford University Press, 2012).
16. Papadopoulos, C. *Nanofabrication*. (Springer International Publishing, 2016). doi:10.1007/978-3-319-31742-7
17. Colson, P., Henrist, C. & Cloots, R. Nanosphere Lithography: A Powerful Method for the Controlled Manufacturing of Nanomaterials. *J. Nanomater.* **2013**, 1–19 (2013).
18. Piner, R. D., Zhu, J., Xu, F., Hong, S. & Mirkin, C. A. ‘Dip-Pen’ nanolithography. *Science* **283**, 661–3 (1999).
19. Esposito, M. *et al.* Nanoscale 3D Chiral Plasmonic Helices with Circular Dichroism at Visible Frequencies. *ACS Photonics* **2**, 105–114 (2015).
20. Kusters, D. *et al.* Core–Shell Plasmonic Nanohelices. *ACS Photonics* **4**, 1858–1863 (2017).
21. Schiff, H. & Kristensen, A. in *Springer Handbook of Nanotechnology* 271–312 (Springer Berlin Heidelberg, 2010). doi:10.1007/978-3-642-02525-9_9
22. Schiff, H. Nanoimprint lithography: An old story in modern times? A review. *J. Vac. Sci. Technol. B Microelectron. Nanom. Struct.* **26**, 458 (2008).
23. Haus, J. W. & Sarangan, A. in *Fundamentals and Applications of Nanophotonics* 149–184 (2016). doi:10.1016/B978-1-78242-464-2.00005-1
24. Yao, Y. *et al.* Nanoimprint lithography: an enabling technology for nanophotonics. *Appl. Phys. A* **121**, 327–333 (2015).
25. Acikgoz, C., Hempenius, M. A., Huskens, J. & Vancso, G. J. Polymers in conventional and alternative lithography for the fabrication of nanostructures. *Eur. Polym. J.* **47**, 2033–2052 (2011).
26. Papadopoulos, C. in *Nanofabrication* 37–44 (Springer, Cham, 2016). doi:10.1007/978-3-319-31742-7_6

27. Hulteen, J. C. & Van Duyne, R. P. Nanosphere lithography: A materials general fabrication process for periodic particle array surfaces. *J. Vac. Sci. Technol. A Vacuum, Surfaces, Film.* **13**, 1553–1558 (1995).
28. Haynes, C. L. & Van Duyne, R. P. Nanosphere Lithography: A Versatile Nanofabrication Tool for Studies of Size-Dependent Nanoparticle Optics. *J. Phys. Chem. B* **105**, 5599–5611 (2001).
29. Hoffmann, J. M., Janssen, H., Chigrin, D. N. & Taubner, T. Enhanced infrared spectroscopy using small-gap antennas prepared with two-step evaporation nanosphere lithography. *Opt. Express* **22**, 14425 (2014).
30. Evangelio, L. Directed self-assembly of block copolymers on chemically nanopatterned surfaces. (2017).
31. Go, S. J., Lee, D.-E., Lee, D. H. & Chin, B. D. Plasmonic nanostructures based on block copolymer templates for efficient organic solar cells. *J. Korean Phys. Soc.* **68**, 257–263 (2016).
32. Mistark, P. A. *et al.* Block-Copolymer-Based Plasmonic Nanostructures. *ACS Nano* **3**, 3987–3992 (2009).
33. Capretti, A. *et al.* Block-copolymer-based plasmonic metamaterials. in *Proc. SPIE 8771, Metamaterials VIII, 87710V* 87710V (2013). doi:10.1117/12.2018492
34. Habteyes, T. G. *et al.* Metallic Adhesion Layer Induced Plasmon Damping and Molecular Linker as a Nondamping Alternative. *ACS Nano* **6**, 5702–5709 (2012).
35. Brown, L. V. *et al.* Fan-Shaped Gold Nanoantennas above Reflective Substrates for Surface-Enhanced Infrared Absorption (SEIRA). *Nano Lett.* **15**, 1272–1280 (2015).
36. Siegfried, T., Ekinici, Y., Martin, O. J. F. & Sigg, H. Engineering Metal Adhesion Layers That Do Not Deteriorate Plasmon Resonances. *ACS Nano* **7**, 2751–2757 (2013).
37. Colas, F., Barchiesi, D., Kessentini, S., Toury, T. & Chapelle, M. L. de la. Comparison of adhesion layers of gold on silicate glasses for SERS detection. *J. Opt.* **17**, 114010 (2015).
38. Bosman, M. *et al.* Encapsulated Annealing: Enhancing the Plasmon

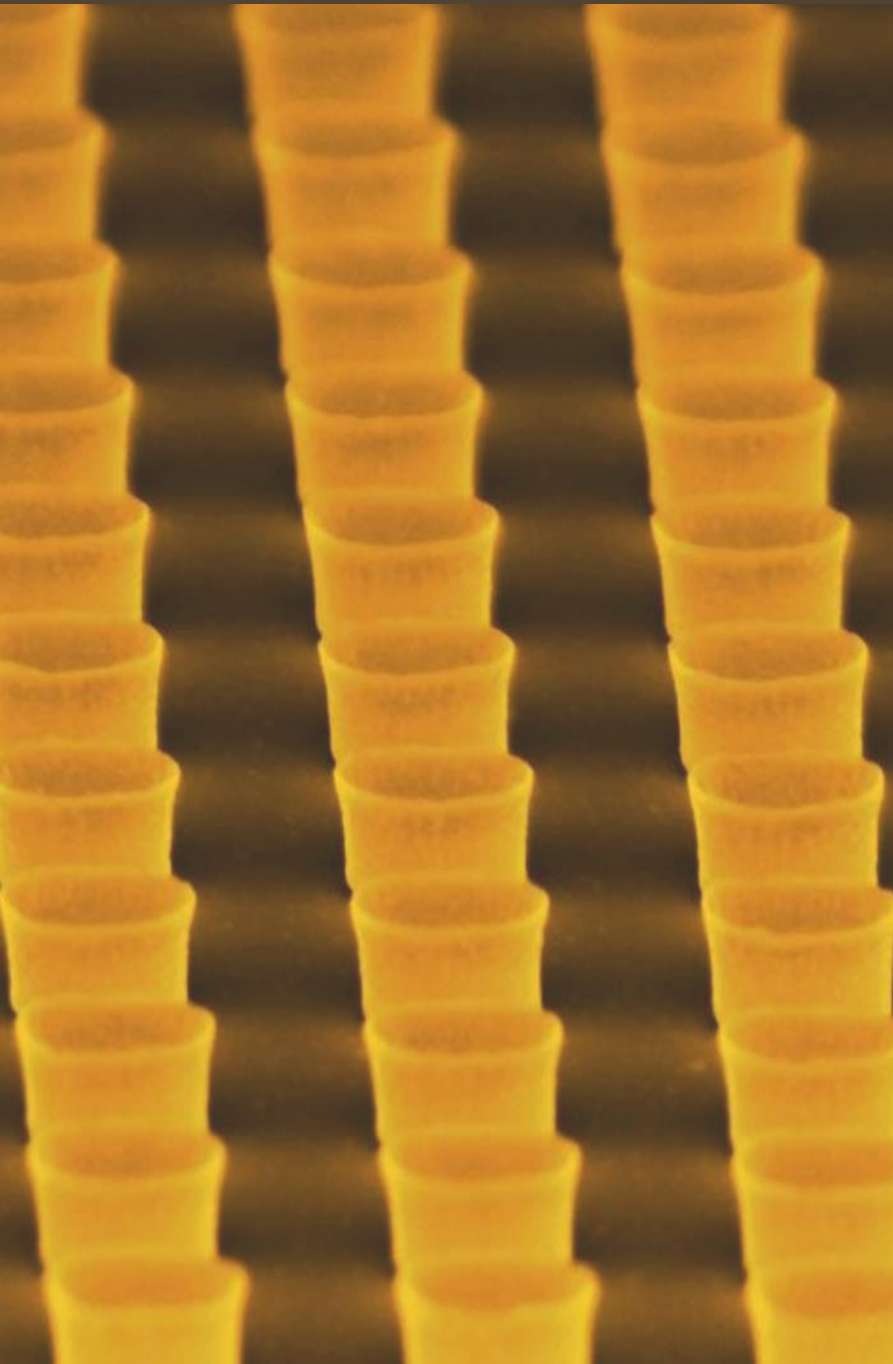
- Quality Factor in Lithographically–Defined Nanostructures. *Sci. Rep.* **4**, 5537 (2015).
39. Ditlbacher, H. *et al.* Silver Nanowires as Surface Plasmon Resonators. *Phys. Rev. Lett.* **95**, 257403 (2005).
40. Flauraud, V. *et al.* Nanoscale topographical control of capillary assembly of nanoparticles. *Nat. Nanotechnol.* **12**, 73–80 (2016).
41. File:Dark field microscopy 2D.pdf - Wikimedia Commons. Available at: https://commons.wikimedia.org/wiki/File:Dark_field_microscopy_2D.pdf. (Accessed: 6th December 2017)
42. Richard Zsigmondy - Facts. Available at: https://www.nobelprize.org/nobel_prizes/chemistry/laureates/1925/zsigmondy-facts.html. (Accessed: 31st May 2018)
43. Huth, F. Nano-FTIR - Nanoscale Infrared Near-Field Spectroscopy. (2015).
44. Guo, Q. Quantitative infrared spectroscopy in challenging environments: applications to passive remote sensing and process monitoring. (2012).
45. Synge, E. H. XXXVIII. A suggested method for extending microscopic resolution into the ultra-microscopic region. *London, Edinburgh, Dublin Philos. Mag. J. Sci.* **6**, 356–362 (1928).
46. Lopez, G. A., Estevez, M.-C., Soler, M. & Lechuga, L. M. Recent advances in nanoplasmonic biosensors: applications and lab-on-a-chip integration. *Nanophotonics* **6**, 123–136 (2017).
47. Li, M., Cushing, S. K. & Wu, N. Plasmon-enhanced optical sensors: a review. *Analyst* **140**, 386–406 (2015).
48. Anker, J. N. *et al.* Biosensing with plasmonic nanosensors. *Nature Materials* **7**, 442–453 (2008).
49. Jin, Y. Engineering plasmonic gold nanostructures and metamaterials for biosensing and nanomedicine. *Adv. Mater.* **24**, 5153–5165 (2012).
50. Mesch, M., Metzger, B., Hentschel, M. & Giessen, H. Nonlinear Plasmonic Sensing. *Nano Lett.* **16**, 3155–3159 (2016).
51. Boardman, A. D. & Zayats, A. V. Nonlinear plasmonics. *Handb. Surf.*

- Sci.* **4**, 329–347 (2014).
52. Gwo, S. *et al.* Plasmonic Metasurfaces for Nonlinear Optics and Quantitative SERS. *ACS Photonics* **3**, 1371–1384 (2016).
 53. Catchpole, K. R. & Polman, A. Plasmonic solar cells. *Opt. Express* **16**, 21793 (2008).
 54. Jang, Y. H. *et al.* Plasmonic Solar Cells: From Rational Design to Mechanism Overview. *Chemical Reviews* **116**, 14982–15034 (2016).
 55. Liu, N., Hentschel, M., Weiss, T., Alivisatos, A. P. & Giessen, H. Three-Dimensional Plasmon Rulers. *Science (80-.)*. **332**, 1407–1410 (2011).
 56. Bauch, M., Toma, K., Toma, M., Zhang, Q. & Dostalek, J. Plasmon-Enhanced Fluorescence Biosensors: a Review. *Plasmonics* **9**, 781–799 (2014).
 57. Neubrech, F., Huck, C., Weber, K., Pucci, A. & Giessen, H. Surface-Enhanced Infrared Spectroscopy Using Resonant Nanoantennas. *Chem. Rev.* **117**, 5110–5145 (2017).
 58. Neubrech, F. *et al.* Resonant Plasmonic and Vibrational Coupling in a Tailored Nanoantenna for Infrared Detection. *Phys. Rev. Lett.* **101**, 157403 (2008).
 59. Du, L., Zhang, X., Mei, T. & Yuan, X. Localized surface plasmons, surface plasmon polaritons, and their coupling in 2D metallic array for SERS. *Opt. Express* **18**, 1959 (2010).



SECTION II

PLASMONIC CYLINDRICAL NANOCUPS



In this section, the fabrication, simulation and optical characterization of Au cylindrical nanocups is presented.

Inspired by the easy tunability of the well known core-shell plasmonic nanostructures and open shell structures, we have gone one step further fabricating ordered arrays of nanocups with a key difference: its cylindrical structure.

Simulations show that, for certain geometries, our nanocups present an homogeneous enhancement of the electric field in the cavity, that is not allowed in the most extended spherical structures due to the lack of symmetry.

The fabrication process, based on a combination of nanoimprint lithography and non-directional metallization, allows for an easy tunability of the geometric parameters. Besides, it is low cost and can be implemented in large scale manufacturing.

Chapter 3

Fabrication of cylindrical nanocups by NIL and sputtering metallization

3.1. Introduction

Gold nanocups or semishells have been the focus of interest of many studies thanks to their adjustable plasmonic response,¹⁻⁸ as well as the results that appear due to the symmetry breaking they present as compared to complete shells.^{1,4,5} Inspired by the easy tunability of core-shell nanoparticles,⁹ nanocups offer the possibility to engineer their plasmonic response as a function of the geometrical parameters, *i.e.*, diameter, height and wall thickness.

Several routes have been used to fabricate cup-shaped nanostructures. Most commonly, chemical synthesis or a combination of chemical synthesis with other physical techniques, such as reactive ion etching (RIE) or metallization, have been used to obtain hollow semi-spheres.² To avoid interparticle effects, nanoparticles can be sparsely dispersed on the substrate, which results in a weak response of the system. Otherwise, when nanoparticles are more densely deposited, interparticle interactions may give rise to an uncontrolled response. However, for certain applications, it is of vital importance to dispose the structures ordered on a substrate to control the interactions between the plasmonic entities. One approach is to benefit from the self-assembly of nanoparticles. For instance, the use of polystyrene spheres allows for ordered arrays of hollow nanocups following a hexagonally-closed-packed distribution,³

but the geometric arrangement of the nanoparticles is limited just to that distribution.

For a more versatile control of the lattice geometry, other methods, such as direct write lithographies or soft lithographies can be used, being the latter a better option to achieve cheap and large-area results, opening up the possibility for commercialization.

In this manuscript, thermal NIL has been used to obtain hollow cylindrical nanostructures. This technique permits a precise control of the geometric parameters, allowing to freely design the arrangement of the structures on the substrate. Besides, NIL is cheap, has high throughput, and in fact, is a technique that is already implemented for mass manufacturing.

However, NIL also has some limitations. In particular, it is not easy to obtain high-aspect ratio structures due to the difficulty of filling high-aspect ratio cavities and the later separation of the imprinted structures from the stamp.¹⁰ To overcome these problems, we propose the use of a trilayer configuration (resist-oxide-resist), for which the bottom resist layer, that controls the height of the structures, is decoupled from the top layer where the NIL process is performed. In addition, the intermediate oxide layer acts as a hard mask to etch the bottom layer, making it possible to obtain high-aspect ratio nanostructures.

Moreover, in contrast to most of previous works which show semi-spherical structures such as semishells, open spheres, or voids, we present cylindrical nanostructures with a constant diameter along the height of the nanostructure. This cylindrical symmetry becomes really handy in enabling the excitation of uniform modes inside the cavity.

3.2. Fabrication method

Hollow cylindrical nanostructures (nanocups) were fabricated by following a tunable cheap method that yields high throughput, permits easy changes of the aspect ratio and offers a precise control of the nanostructure's geometry. In particular, the arrangement of the nanostructures on the substrate provides an easy way to control the interaction and plasmonic response of the individual

structures and is essential for plasmonic applications. Moreover, different materials could be combined without increasing the difficulty of the fabrication process, to obtain, for example, multifunctional nanostructures, or combine the plasmonic response of different materials. The method, sketched in Figure 3.1, is based on a combination of NIL and non-directional sputtering metallization.¹¹

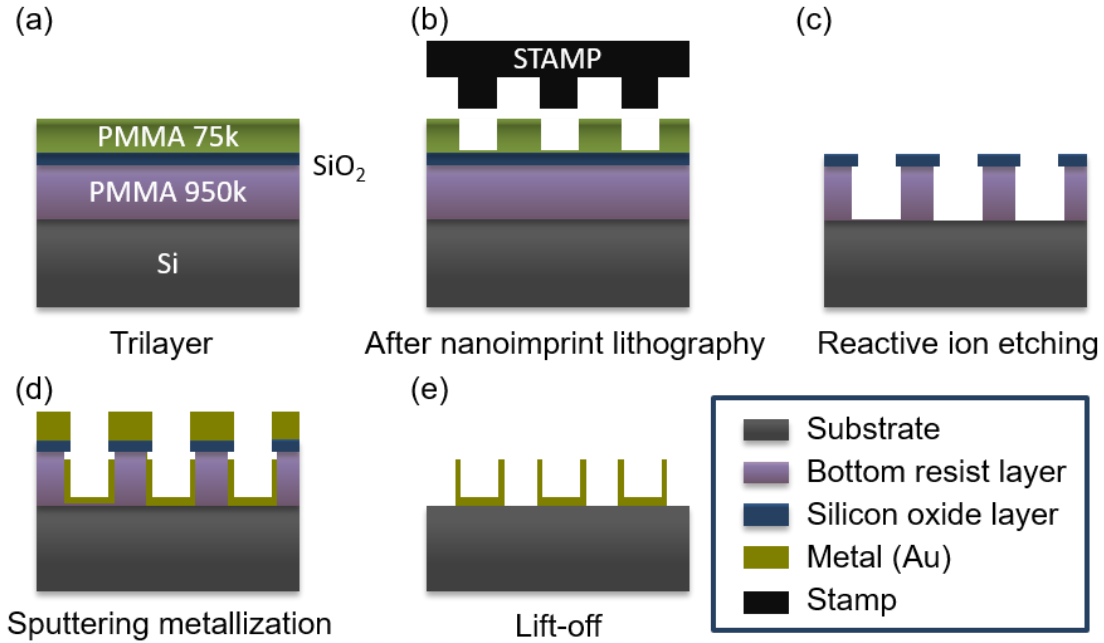


Figure 3.1 Sketch of the fabrication procedure to obtain nanocups.

3.2.1. Mold

The fabrication of the mold is the most expensive stage; however, the mold can be reused hundreds of times.

Molds can be classified in hard and soft molds. Hard molds are usually made of quartz or Si, and are characterized by their rigidity, durability and the easy way to clean them. Soft molds are made of polydimethylsiloxane (PDMS) or plastic, which allows nanoimprinting on curved surfaces. They have, usually, fewer defects, but the patterns are easier to deform worsening the final resolution of the nanostructure. Hybrid molds, which are a combination of both cases where the soft and hard parts are attached together, overcome most of the limitations previously commented.¹²

In our case, and due to the fact that the desired structures were of the order of 350-500 nm, Si molds were fabricated by photolithography followed by an oxidation process to reduce dimensions (see Figure 3.2). To do so, a commercial reticle (Photronics) was designed to fabricate holes with different pitch and diameter, ranging from 0.7 to 2.5 μm pitch and 350 to 500 nm diameter.

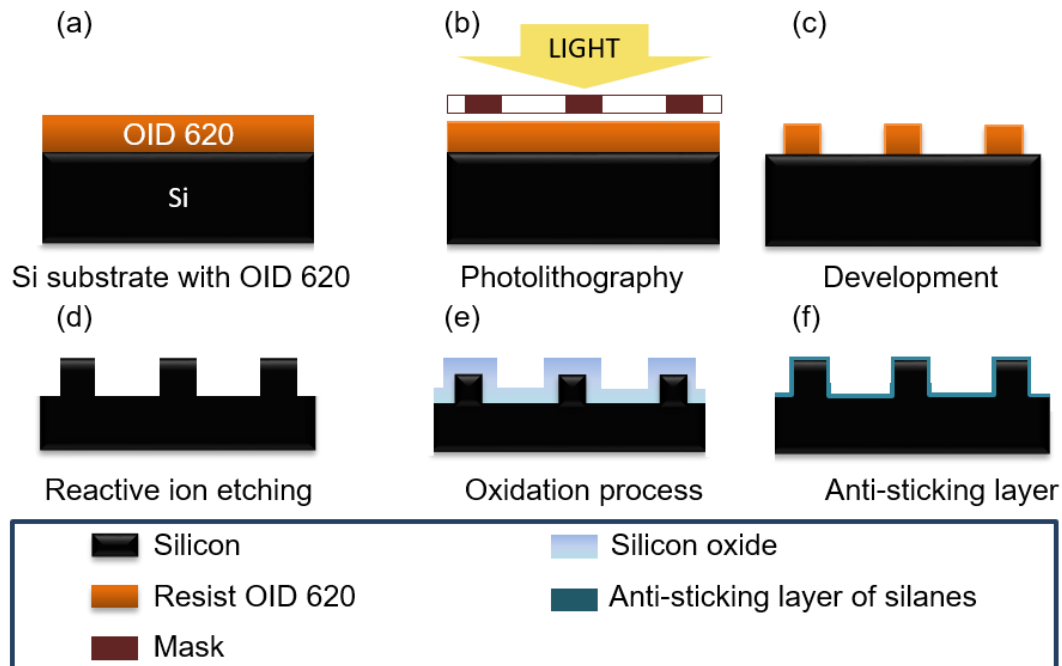


Figure 3.2 Sketch of the fabrication process to obtain the molds for the thermal NIL.

Photolithography

A 600 nm layer of positive resist (OID 620) was used for the photolithography procedure.

In positive resists, the exposed regions become soluble due to chain incision, *i.e.*, the irreversible breaking of the covalent bonds in the polymer, which reduces the mean molecular weight, increasing its solubility. On the contrary, in the case of negative-tone resists, the polymer molecules are cross-linked, forming additional covalent bonds between chains that in turn results in an increase of the molecular weight, reducing its solubility, and therefore the exposed area will remain after the development.¹³

Photolithography was performed with an i-line stepper (NIKON NSR 1505-G7) whose theoretical resolution is ~ 350 nm. Several patterns were processed in separate wafers to optimize the results, by adjusting the exposition time (between 340 and 370 ms) and the offset focus (between - 0.2 and 0). In each wafer, 52 molds of 1×1 cm² were obtained, each of which can be used for many imprints. In this way, the fabrication of molds is also low cost, being the reticle, the only important investment to make.

Reactive ion etching

To transfer the pattern to the Si, dry etching, in particular, RIE is used.

In dry etching, chemically reactive neutrals, like F and Cl, and ions, such as SF_x⁺, formed by the collision of molecules in a reactive gas (such as SF₆, C₄F₈, or Cl₂) with a cloud of energetic electrons excited by a RF field, are accelerated under the effect of an electric field towards a target substrate. When the process implies ion bombardment, it is called RIE.¹⁴

ALCATEL AMS-110 DR from the IMB-CNM clean room facilities was used to etch the samples. The RIE was performed in a three-step process. First, the native silicon oxide layer was etched for 30 seconds using 50 sccm of C₄F₈, under a pressure of 0.3 Pa and a source and a chuck power of 1800 and 50 W, respectively. Afterwards, a mixture of C₄F₈ (30 sccm) as passivating agent and SF₆ (20 sccm) as etching agent at a pressure of 2 Pa, and a source and a chuck power of 220 and 20 W were used to etch the Si.

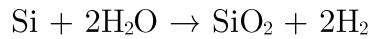
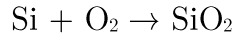
The length of the second step can be modified to adjust the height of the obtained structures. The time can be increased up to the moment in which resist mask completely disappears. At that time, the maximum height is obtained, which in our case corresponds to 130 nm. Finally, to eliminate the resist, oxygen plasma is performed.

When examining the molds in the SEM we observed some residues that were eliminated in a stripper solution for 10 minutes followed by 10 minutes in water, in an ultrasound bath at 60°C.

Oxidation

When the desired dimensions for the final structures are beyond the resolution of the stepper, one can reduce the size of the features of mold's patterns by oxidizing them and then removing the oxide layer, being this procedure much cheaper and faster than other alternatives such as direct writing techniques.

Thermal oxidation of Si is done by heating the wafer up to high temperatures (900-1200°C) in an atmosphere containing oxygen or water vapor that diffuse through Si. Hence, oxygen combines with Si to form SiO₂ via:



During the process, Si is consumed as the oxide grows and the oxide expands.¹⁴ When a layer of oxide of thickness t is grown, the initial Si is reduced by $0.46t$, meaning that if cylinders had a diameter D , the final diameter would be $D-0.92t$ (see Figure 3.3).

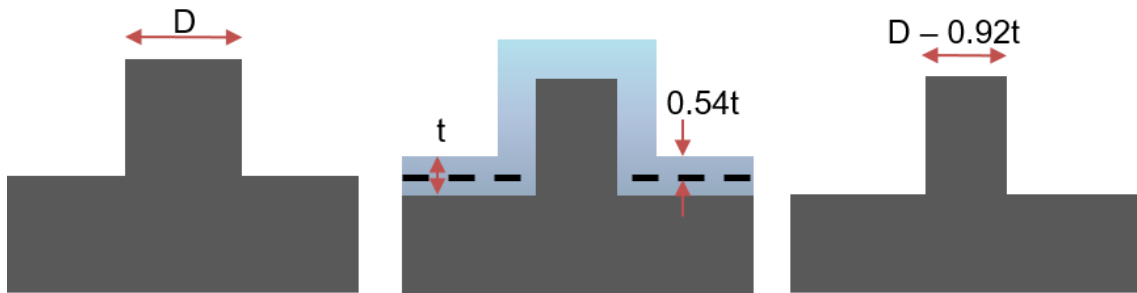


Figure 3.3 Sketch of the oxidation process. From the thickness of the grown oxide layer (t), 46% corresponds to the actual reduced thickness of the Si layer, and 54% comes from the expansion of the SiO₂ lattice with respect to that of the Si.

To do so, the BTU-Bruce diffusion furnace at the IMB-CNM clean room facilities was used. Before the oxidation, a thorough cleaning of the molds was performed to eliminate impurities and organic residues. The molds were put inside the furnace at 400°C under a flow of N₂. Then, the temperature was increased up to 1000°C under a flow of 6000 sccm of N₂ and 1000 sccm of O₂ with a ramp of 2 hours. The main oxidation process took place at 1000°C and under a flow of 7500 sccm of O₂. The duration of the oxidation process was

adjusted depending on the desired oxide thickness. After that, the temperature was decreased and fixed to 600°C during 1.5 hours under a flow of nitrogen and finally reduced to 400°C.

The oxide layer growth is not a linear process: as the oxidation goes on, oxygen must pass through a thicker oxide layer to reach the Si and the growth rate decreases.¹⁴ In our case, the maximum thickness that could be obtained was approximately 100 nm. Hence, when more than 100 nm of oxide are required, the SiO₂ layer has to be removed by wet etching before the oxidation process is repeated (see Figure 3.4).

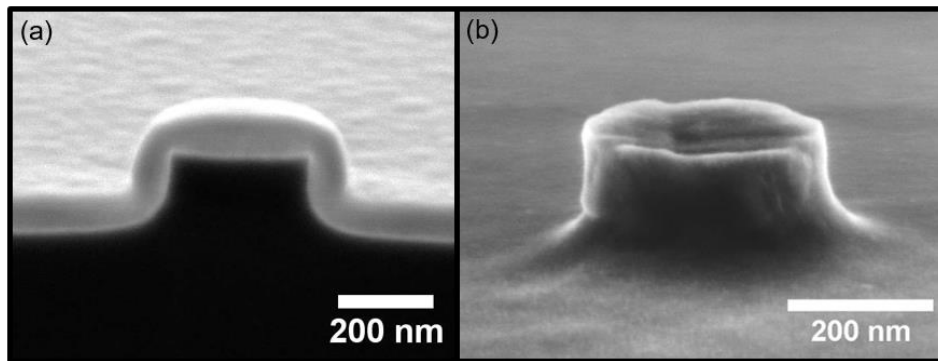


Figure 3.4 SEM image of (a) a cylinder of the mold after the oxidation where the conformal layer of oxide is visible; (b) the resulting cylinder after the removal of the oxide layer.

Functionalization

The molds were functionalized with an anti-sticking layer of silanes (1H,1H,2H,2H-perfluoro-octyltriethoxysilane, FTS13, from Sigma Aldrich) to prevent them from sticking to the resist. First, to enhance the formation of OH-groups, the molds were exposed to oxygen plasma. Subsequently, silanes were deposited by vapor deposition in a nitrogen atmosphere for 1 hour.

3.2.2. Fabrication of the sample

Substrates

Substrates should be chosen according to later applications. In this thesis, glass substrates (LH24.1 precision cover slips from Carl Roth GmbH + Co. KG)

were chosen for their transparency in the visible and near infrared regions of the spectrum, allowing for the later transmission measurements.

Another approach applied along these pages is the use of a metal-insulator-metal stack. This is a widely used technique in plasmonics that consists of an optically thick metallic layer and a dielectric spacer on top of which the structures are fabricated. This scheme is used either to couple the propagating modes in the metallic layer to the localized modes in the structures or to reflect light and enhance the response by coherent interference.¹⁵⁻²⁴

The fabrication process requires a thorough cleaning of the substrates as any dust particle or impurity will affect the final quality of the sample. Therefore, substrates were cleaned in an ultrasonic bath at 40°C for 10 minutes in acetone, followed by 10 minutes in isopropanol and dried with a nitrogen gun. To complete the cleaning process and improve the subsequent spin-coating, the substrate was also subjected to oxygen plasma at 500 W in TEPLA for 5 minutes.

Trilayer stack

One of the limitations of nanoimprint lithography is the aspect ratio, especially during the demolding.¹⁰ To overcome this limitation, a trilayer stack can be used.²⁵ The trilayer is composed by a bottom resist layer, which will determine the height of our nanostructures, a thin oxide layer, than will act as a hard mask during the etching, and a top resist layer where the patterning of the sample is performed. Consequently, the height of the structures is no longer linked to the imprinting step and better results can be achieved.

Bottom layer

A wide variety of resists can be used, in principle, being the desired thickness the key parameter to choose the most suitable one. For the samples presented here, PMMA 950K A7 (Microchem) was used since our objective was to spin-coat layers of resist around 400-600 nm. Several values of speed were used to obtain structures of different heights. In some cases, the resist was diluted in anisole to reduce the thickness of the layer.

Thin oxide layer as hard mask

A layer of silicon oxide was used as a hard mask. This layer is deposited by Plasma Enhanced Chemical Vapor Deposition (PECVD) (Oxford 800Plus).

PECVD is a chemical vapor deposition technique (CVD) whose working principle relies on the controlled reaction of a precursor gas that results in the deposition of the reacted species on a heated substrate. In the case of PECVD, not only thermal energy but also an RF-induced glow discharge is used to provoke the reaction. Usually, a carrier gas is used, most commonly N_2 , to allow the substrate to remain at a lower temperature than in the case of CVD. The glow-discharge, generated by an RF-field, creates free electrons with enough energy to dissociate the reactant gases to form the solid film on the substrate. PECVD allows for low deposition temperature, good dielectric properties, low mechanical stress and good conformal step coverage.²⁶

Here, SiO_2 is deposited by reacting 25 sccm of silane (SiH_4) with 1000 sccm of nitrous oxide (N_2O), using N_2 as a carrier, 955 sccm. The process is performed on the substrate with the top layer of resist, and hence, care must be taken to keep the temperature low. Therefore, the process is performed at $150^\circ C$ with an RF power of 100 W and a pressure of 1000 mTorr.

This layer has to be thick enough to endure the etching process. However, the thicker it is, the more material will be deposited during metallization and the more clogging of the cavities one will have. So, it will be harder to properly metalize those cavities.

Top layer

The top resist layer is the place where the patterning process is carried out. Thus, the resolution achievable with a specific resist is a key point. Mr-I PMMA 75k (Micro Resist Technology) has been used. The thickness of the resist layer has to be fixed according to the height of the structures of the mold in order to reduce as much as possible the residual layer after the imprinting of the mold.

As explained before, the fact that the patterning process only affects the top layer means that one could, in principle, spin-coat a bottom layer as thick as

desired to obtain high aspect ratio nanostructures as the bottom layer does not affect the patterning layer at all. However, this fabrication method has still some limitations that will be discussed later.

Nanoimprint lithography (NIL)

To create the patterns by thermal NIL; the sample has to be heated above the glass transition temperature (T_g) of the resist (114°C for PMMA, depending on the commercial brand²⁷) to make it flow; usually 50 to 80 K above T_g . In our case, the sample is heated up to 180°C and kept for 2 minutes at constant temperature to achieve thermal stability. Then a pressure of 40 bar is applied during 5 minutes to ensure the resist fills all the cavities of the mold. Afterwards, the sample is cooled down below T_g before demolding (at 80-90°C) so that the resist becomes hard enough and the patterns remain with the minimum possible distortion.

Reactive ion etching

This is probably the most delicate step of the fabrication process and it requires high precision in adjusting the times. It is composed of two steps.

The first step is used to etch the residual layer left after the NIL process (that is, the resist that remains in the holes we wanted to make) and the oxide layer. The top resist layer acts as a hard mask to etch the oxide. This is done using 50 sccm of C_4F_8 , a pressure of 0.6 Pa and a source and chuck power of 450 and 50 W, respectively. The duration of the process has been varied for different top layer thickness, oxide thickness or mold height from 50 seconds to 1 minute 30 seconds. Also, in case the residual layer is too thick, oxygen plasma can be applied for some seconds to reduce it before etching the oxide layer.

Secondly, the bottom layer is etched until the desired undercut is obtained (oxygen plasma produces an isotropic etch in the PMMA) while the oxide acts as a hard mask. The parameters used for this step were: 15 sccm of O_2 , a source power of 200 W, a chuck power of 15 W, a pressure of 0.1 Pa and various times depending on the thickness of the bottom layer and the desired undercut. Both

procedures have been carried out in the DRIE AMS-110 from the IMB-CNM clean room.

Besides, same results have been obtained using Oxford 80Plus in the Laboratori d'Ambient Controlat of Universitat Autònoma de Barcelona where a mixture of O_2 and CHF_3 is used for the first step and O_2 plasma is also used for the second step obtaining equivalent results to those from the AMS-110.

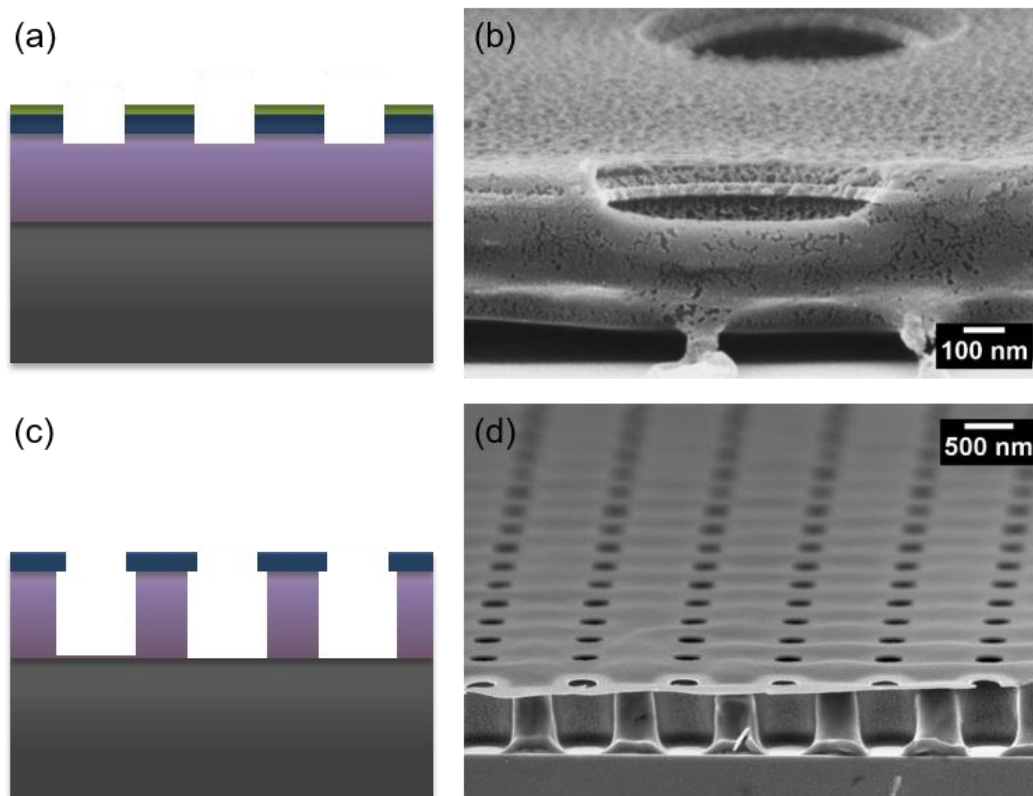


Figure 3.5 Scheme (left column) and SEM images (right column) of the etching process. (a) and (b) correspond to the first step of the reactive ion etching, where the SiO_2 layer is etched. (c) and (d) show the final etch, where the bottom resist layer is etched while the SiO_2 layer acts as a mask.

Metallization process

Depending on the type of metallization, different structures can be obtained. When using electron beam evaporation, as it is a directional method, solid structures such as nanocones or nanodots can be obtained.¹¹ However, we have focused our work in hollow structures, which are obtained by non-directional

sputtering metallization. Also a combination of both directional and unidirectional deposition with the same or different materials could be done.¹¹

Metallization of the structures has also been performed in two setups: the home-made equipment from our group in the Physics Faculty of the University of Barcelona and the 903 MRC (Materials Research Corporation) at the IMB-CNM clean room.

For plasmonics, the most extended materials are Ag and Au. In this case, Au was chosen due to its inertness and the easy functionalization with thiols.

We used a model to compute the thickness of the lateral walls of our nanostructures as a function of the thickness of the deposited material, the thickness of the bottom layer, the diameter of the hole in the oxide layer and the undercut. This calculation is carried out assuming that the material is homogeneously distributed throughout the cavity.¹¹ Results showed that the latter assumption is only valid for certain values of the parameters. By analyzing the results as a function of both the Ar pressure and the power, we concluded that for high pressures and low powers the assumption was successfully fulfilled.¹¹

This is another key aspect of the fabrication method. One has to keep in mind that very thin walls are indeed a problem for the later lift-off process but thick walls could be a problem as well if gold from the cavity and gold from the top layer became contacted, since the lift-off would be impossible in that case. That can be overcome by tuning the undercut monitoring the etching time. This necessarily yields a larger diameter of the final nanostructures.

Although Au is the most used material for plasmonics thanks to its plasmonic properties, inertness and easy functionalization, it is adhered poorly to glass and Si, and the use of an adhesion layer is broadly used. Metals such as Ti or Cr or metal oxides such as TiO₂ or Cr₂O₃ are widely used as adhesion promoters. However, it has been reported that this adhesion layer may worsen the properties of the nanostructures.^{28,29} In the present work, a 5 nm thick Ti layer was deposited, (even though one should keep in mind that the final amount of Ti in the structures would be much less). However, we also

fabricated some samples without the adhesion layer to check the actual attenuation on the plasmonic response that it caused.

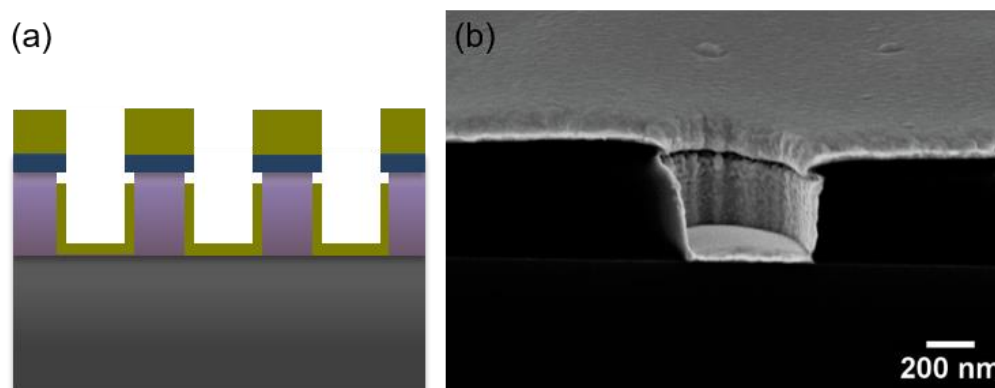


Figure 3.6. Scheme (a) and SEM image (b) of the sputtering metallization. (b) shows the results after metallizing the sample with 5 nm of Ti and 100 nm of Au.

Lift-off

For the lift off, samples were dipped in an acetone bath at 40°C for 5 minutes. Then, ultrasounds were applied until the lift-off was completed (normally less than a minute).

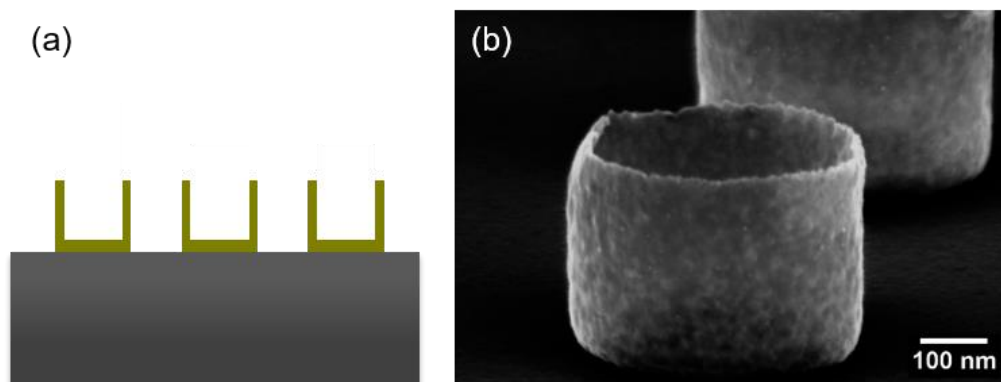


Figure 3.7. Scheme (a) and SEM image (b) of the resulting structures after the lift-off process.

3.2.3. Tunability of the fabrication process.

This fabrication route enables us for an easy tunability of the geometry (see Figure 3.8). For instance, the height of the nanostructures can be modified just by changing the thickness of the bottom layer. Besides, the thickness of the

deposited material will determine both the wall and base thicknesses of the nanostructures. And finally, the diameter of the nanostructures can be tuned to a certain extent by modifying the time of the second step in the RIE.

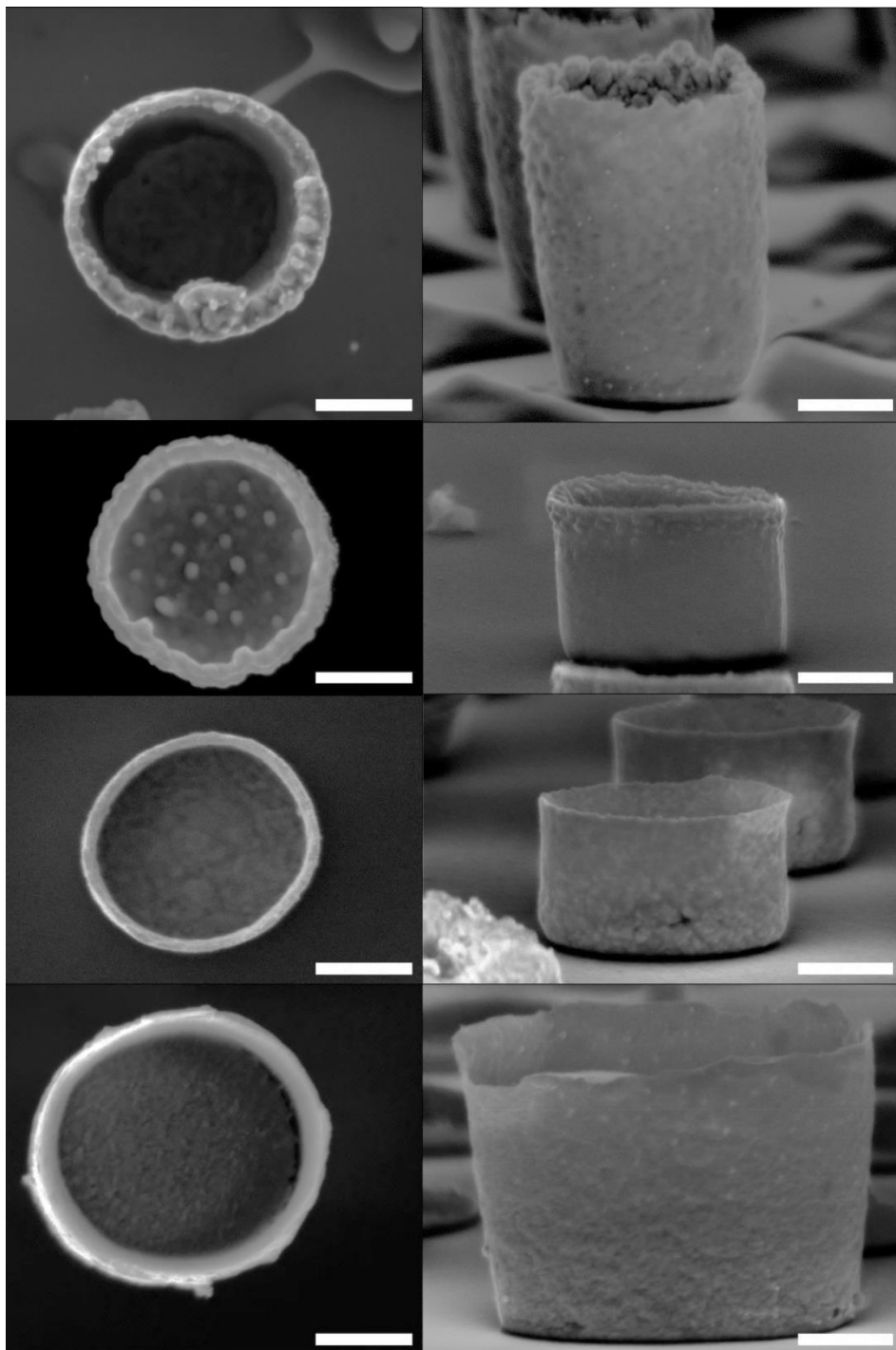


Figure 3.8. Top (left) and side (right) views of cup shaped nanostructures with different geometries. The scale bars correspond to 200 nm.

Moreover, this technique allows combining different materials, which could be deposited by sputtering without breaking the vacuum to obtain multi-layered nanocups. Also, a combination of sputtering and electron beam evaporation could be used to fill the nanocup with another material by metallizing first with sputtering and carrying out a subsequent metallization by electron beam evaporation.¹¹

3.3. Large area fabrication

Presented as one of the alternatives for the next generation lithographies, one of the main drawbacks of nanoimprint is the relatively large amount of imperfections and defects that are transferred from the mold by direct contact to the resist.³⁰ However, in plasmonics or, at least, in our particular case, the amount of defects is not as crucial as for semiconductor device fabrication, since we are only interested in the overall response of the system.

Aside from that, the use of nanoimprint lithography enables scalable production for commercial applications. For instance, the molds used for the fabrication of the samples in this work were 1x1 cm² in effective area, proving the validity and homogeneity of the process to pattern large areas. The machine used for the preparation of our samples allows patterning 4-inch wafers. Moreover, there are other approaches available for larger areas.

Step and flash UV imprint lithography uses a small template that is replicated along the substrate, reducing the cost of fabricating a large-scale stamp. The resist is locally deposited in the substrate, only in the region that will be immediately printed, to avoid the exposure of the surrounding resist. Then the template is aligned with the substrate, it contacts the resist, and light is aligned to cure the resist. Once the resist is cured, the template is moved to the next field and the process is repeated.³¹ There are also some companies that work with the thermal version, but the resist needs to cool down before moving the template to the next area, making it a slower process. However, there are some concerns related to throughput, template cost, overlay or defectiveness.³² Roller based NIL, and in particular roll to roll NIL where nanopatterns are replicated from a master roll to a substrate roll, shows promising results for

commercial applications. Similar to step and flash NIL, the patterns from a small master roll can be transferred to large areas by repeating the roll to roll NIL process.^{33,34}

3.4. Fabrication of nanocups by soft nanoimprinting

The nanocups have also been fabricated by soft nanoimprinting with a hard PDMS mold onto an SU8 photoresist (2000.5 Microchem) in collaboration with Dr. A. Mihi's group in the Institut de Ciència de Materials de Barcelona (ICMAB). In this case, the molds had a pitch of 400, 500 and 600 nm, and the patterns were cylinders of 300 nm. Here, the residual layer after the imprinting was much thicker so the first RIE step was increased to 3 minutes. Structures of different heights were fabricated (from 300 to 600 nm) so the etching time of the bottom resist layer was modified accordingly between 2 and 3 minutes. Using these molds, very dense arrays of nanocups were fabricated (see Figure 3.9).

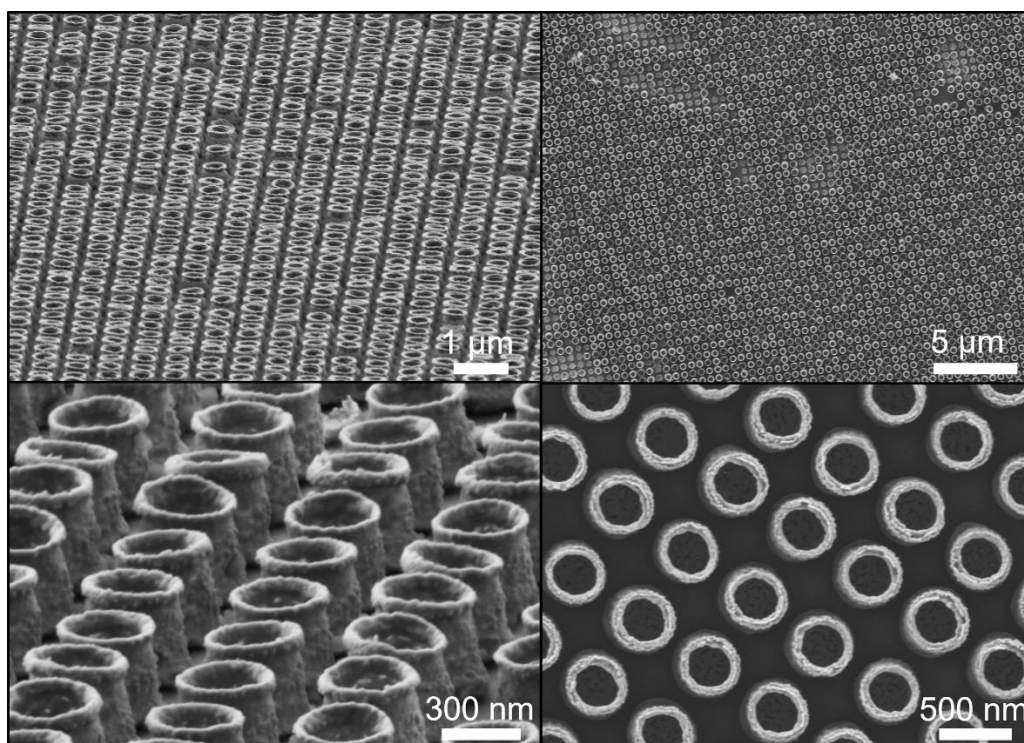


Figure 3.9. Side (left) and upper (right) views of the arrays of nanocups fabricated by soft nanoimprinting.

3.5. Conclusions

In this chapter, a detailed description of the fabrication process of hollow cylindrical nanostructures with tunable aspect ratio has been presented. This method, that combines NIL and a hard mask concept, together with non-directional metallization, overcomes the high-aspect ratio limitations of NIL and other limitations that other methods present such as low throughput or lack of control of the arrangement of the structures on the substrate. As a matter of fact, arrays of $1 \times 1 \text{ cm}^2$ have been fabricated and the fabrication of high-aspect ratio nanostructures has also been demonstrated. This process could be adapted as well to other soft-lithographies as shown for soft imprinting.

Besides, the use of photolithography in combination with an oxidation process enabled us to fabricate sub-diffraction patterns to be used as molds for the imprint process in a much cheaper way than conventional direct-writing techniques.

Taking all the aforementioned into account, it is concluded that this fabrication approach is suitable for up-scale production with a precise control of geometry and distribution of the structures, so it is ideal for plasmonics at large scale.

3.6. References

1. Ye, J., Lagae, L., Maes, G., Borghs, G. & Van Dorpe, P. Symmetry breaking induced optical properties of gold open shell nanostructures. *Opt. Express* **17**, 23765 (2009).
2. King, N. S. *et al.* Angle- and Spectral-Dependent Light Scattering from Plasmonic Nanocups. *ACS Nano* **5**, 7254–7262 (2011).
3. Wollet, L. *et al.* Plasmon hybridization in stacked metallic nanocups. *Opt. Mater. Express* **2**, 1384 (2012).
4. Cortie, M. & Ford, M. A plasmon-induced current loop in gold semi-shells. *IOP Publ. Nanotechnol. Nanotechnol.* **18**, 235704–6 (2007).
5. Van Dorpe, P. & Ye, J. Semishells: Versatile Plasmonic Nanoparticles. *ACS Nano* **5**, 6774–6778 (2011).
6. Knight, M. W. & Halas, N. J. Nanoshells to nanoeggs to nanocups: optical properties of reduced symmetry core-shell nanoparticles beyond the quasistatic limit. *New J. Phys.* **10**, 105006 (2008).
7. Frederiksen, M., Bochenkov, V. E., Cortie, M. B. & Sutherland, D. S. Plasmon Hybridization and Field Confinement in Multilayer Metal-Dielectric Nanocups. *J. Phys. Chem. C* **117**, 15782–15789 (2013).
8. Ye, J. *et al.* Plasmonic Modes of Metallic Semishells in a Polymer Film. *ACS Nano* **4**, 1457–1464 (2010).
9. Oldenburg, S. ., Averitt, R. ., Westcott, S. . & Halas, N. . Nanoengineering of optical resonances. *Chem. Phys. Lett.* **288**, 243–247 (1998).
10. Scheer, H., Mayer, A., Dhima, K., Wang, S. & Steinberg, C. Challenges with high aspect ratio nanoimprint. *Microsyst. Technol.* **20**, 1891–1898 (2014).
11. Alayo, N. *et al.* Nanoparticles with tunable shape and composition fabricated by nanoimprint lithography. *Nanotechnology* **26**, 445302 (2015).
12. Yao, Y. *et al.* Nanoimprint lithography: an enabling technology for nanophotonics. *Appl. Phys. A* **121**, 327–333 (2015).

13. Bucknall, D. G. *Nanolithography and patterning techniques in microelectronics*. (Woodhead Publishing Limited, 2005). doi:10.1533/9781845690908
14. Jaeger, R. C. *Introduction to microelectronic fabrication. Processing V*, (2002).
15. Lin, L. & Zheng, Y. Optimizing plasmonic nanoantennas via coordinated multiple coupling. *Sci. Rep.* **5**, 14788 (2015).
16. Liu, N., Mesch, M., Weiss, T., Hentschel, M. & Giessen, H. Infrared Perfect Absorber and Its Application As Plasmonic Sensor. *Nano Lett.* **10**, 2342–2348 (2010).
17. Christ, A. *et al.* Interaction between localized and delocalized surface plasmon polariton modes in a metallic photonic crystal. *Phys. status solidi* **243**, 2344–2348 (2006).
18. Yan, M. Metal–insulator–metal light absorber: a continuous structure. *J. Opt.* **15**, 025006 (2013).
19. Brown, L. V. *et al.* Fan-Shaped Gold Nanoantennas above Reflective Substrates for Surface-Enhanced Infrared Absorption (SEIRA). *Nano Lett.* **15**, 1272–1280 (2015).
20. Du, L., Zhang, X., Mei, T. & Yuan, X. Localized surface plasmons, surface plasmon polaritons, and their coupling in 2D metallic array for SERS. *Opt. Express* **18**, 1959 (2010).
21. Chen, Y., Dai, J., Yan, M. & Qiu, M. Honeycomb-lattice plasmonic absorbers at NIR: anomalous high-order resonance. *Opt. Express* **21**, 20873 (2013).
22. Chen, Y., Dai, J., Yan, M. & Qiu, M. Metal-insulator-metal plasmonic absorbers: influence of lattice. *Opt. Express* **22**, 30807 (2014).
23. Chu, Y. & Crozier, K. B. Experimental study of the interaction between localized and propagating surface plasmons. *Opt. Lett.* **34**, 244 (2009).
24. Liu, F., Zhang, X. & Fang, X. Plasmonic plano-semi-cylindrical nanocavities with high-efficiency local-field confinement. *Sci. Rep.* **7**, 40071 (2017).

25. Yu, Z., Gao, H., Wu, W., Ge, H. & Chou, S. Y. Fabrication of large area subwavelength antireflection structures on Si using trilayer resist nanoimprint lithography and liftoff. *J. Vac. Sci. Technol. B Microelectron. Nanom. Struct.* **21**, 2874 (2003).
26. HITECH PROJECTS. Plasma Enhanced CVD. Available at: <http://www.hitech-projects.com/dts/docs/pecvd.htm>. (Accessed: 9th October 2017)
27. Utke, I., Moshkalev, S. & Russell, P. *Nanofabrication Using Focused Ion and Electron Beams: Principles and Applications*. (Oxford University Press, 2012).
28. Colas, F., Barchiesi, D., Kessentini, S., Toury, T. & Chapelle, M. L. de la. Comparison of adhesion layers of gold on silicate glasses for SERS detection. *J. Opt.* **17**, 114010 (2015).
29. Sexton, B. A., Feltis, B. N. & Davis, T. J. Characterisation of gold surface plasmon resonance sensor substrates. *Sensors Actuators A Phys.* **141**, 471–475 (2008).
30. Hatano, M. *et al.* NIL defect performance toward high volume mass production. in *SPIE Advanced Lithography* (eds. Bencher, C. & Cheng, J. Y.) **8680**, 97770B (International Society for Optics and Photonics, 2016).
31. Colburn, M. *et al.* Step and Flash Imprint Lithography: A New Approach to High-Resolution Patterning.
32. Malloy, M. & Litt, L. C. Step and Flash Imprint Lithography for Semiconductor High Volume Manufacturing. *J. Photopolym. Sci. Technol.* **23**, 749–756 (2010).
33. Kooy, N. *et al.* A review of roll-to-roll nanoimprint lithography. *Nanoscale Res. Lett.* **9**, 1–13 (2014).
34. Roll-to-roll nanoimprint lithography for patterning on a large-area substrate roll. *Microelectron. Eng.* **123**, 18–22 (2014).

Chapter 4

Optical properties of Au nanocups

4.1. Introduction

Gold nanocups, semishells and other hollow metallic nanostructures have been the focus of interest of many studies thanks to their adjustable plasmonic response¹⁻²⁵ and the new properties they present, induced by symmetry breaking with respect to complete shells.^{20,23-26} Inspired by the easy tunability of core-shell nanoparticles,^{1,2,5-8,13,19,27} nanocups offer the chance to engineer their optical response as a function of diameter, height and wall thickness.

Along this chapter, FDTD simulations were used to find the optimum parameters for the fabrication of the nanocups as well as to compare with optical characterization measurements. Far- and near-field simulations have been performed. First, the spectra for visible (VIS) and near infrared (NIR) regions were obtained for different conditions. Then, on-resonance excitation is used to analyze the near-field response, obtaining the electric field and charge distributions of the different modes.

4.1.1. Nanoshells: highly tunable plasmonic nanostructures

The interest of having customized nanostructures to tune the interaction with the electromagnetic radiation requires precise synthesis or nanofabrication methods to properly engineer the optical resonances. Probably, one of the most studied structures is the nanoshell,^{1,2,5-8,13,19,27} composed of a thin metal shell of nanometer thickness with a (usually concentric) dielectric (or more rarely semiconductor) core. This is due to the easy control of its response as a function

of its geometric parameters: by simply varying the ratio between the core and shell dimensions, the optical resonance of this type of structure can be shifted hundreds of nanometers, from the visible to the infrared region of the spectrum.^{1,5,6,13,27} Besides, these structures interact strongly with the EM waves, having an extinction cross-section that is typically five times the physical cross section.^{1,6,7}

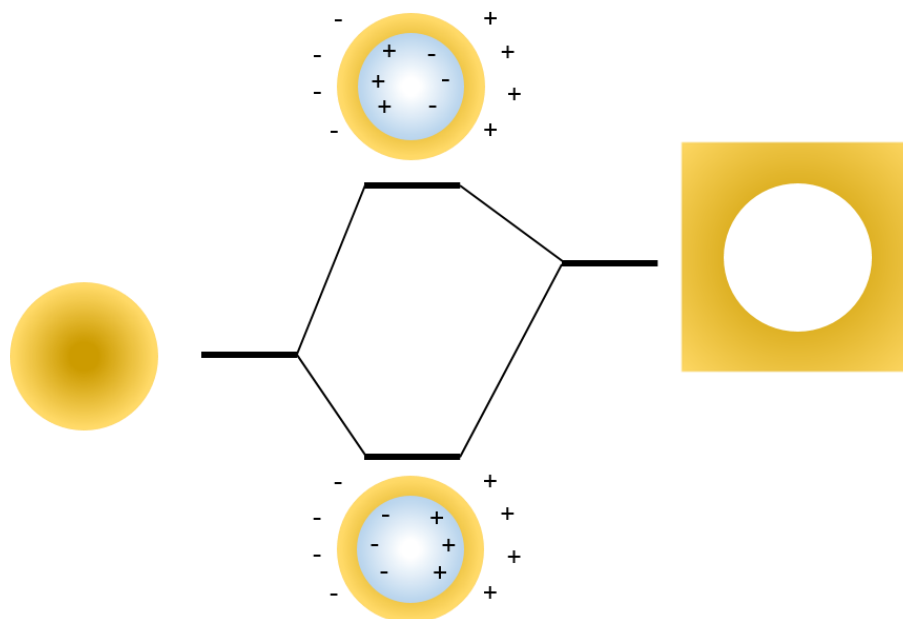


Figure 4.1 Energy-level diagram showing the plasmon hybridization in metal nanoshells. Based on Ref. 28.

The plasmon hybridization model can be used for a better understanding of the plasmonic response of complex structures such as nanoshells. Proposed in 2003 by P. Nordlander and co-workers, it is an EM analogue to the well-known molecular orbital theory used to predict how atomic orbitals interact to form the molecular orbitals.²⁸ The model consists on decomposing a complex plasmonic structure in simpler ones, calculating how the plasmons behave in the simpler elements and, finally, how these plasmons interact to generate the hybridized modes of the complex structure. Nanoshells can be regarded as the interaction between the response of a nanosphere and a spherical cavity (see Figure 4.1).^{7,28} Interaction effects are highly dependent on the shell thickness and give rise to two states: the lower energy "bonding" mode and the higher "anti-bonding" mode. The lower energy mode, which is symmetric, yields large absorption due to its high dipole moment. Hence, nanoshells show dipole plasmon resonances with redshifts relative to the corresponding modes for solid nanospheres.⁸ The plasmon resonance can be tuned by changing the thickness of

the shell: thinner shells give rise to higher splitting of the energy modes and therefore a shift of the bonding mode to lower energies due to the higher interaction, in agreement with Mie theory.⁷

For small nanoshells that respond like dipoles to the applied EM field, the plasmon resonance wavelength depends only on the ratio between the shell and the core radius, and not on the absolute size.^{1,2,13,19} When cores are small, the extinction peaks lie in the VIS or NIR and the change in the total particle size, keeping a constant core/shell ratio, will control the ratio between absorbed and scattered light: in small particles, absorption will be dominant, whereas an increase in the size will result in a larger scattering cross section.^{6,7,27}

When the size is increased beyond the dipole limit and the diameter of the particles reaches sizes of the order of λ , the full Mie scattering theory needs to be used and a redshift is observed for increasing size, even if the core/shell ratio is kept constant. This is accompanied by a broadening of the linewidth and higher order modes start to be noticeable, giving rise to new peaks.^{1,27} With a decrease in the shell thickness while the core size is kept constant, a shift to longer wavelengths is observed, making it possible to obtain structures with surface plasmon resonances in the NIR region.^{1,13} This fact can be understood according to the plasmon hybridization theory as due to the increasing interaction between the sphere and cavity plasmons, giving rise to a bigger splitting between the two hybrid modes. At the same time, as the nanoshells become bigger, the higher-order modes gain increasing importance as compared to dipolar ones.^{1,2,8,13,19} All these facts come as a consequence of the retardation of the electric field for sizes comparable to the wavelength of light.²⁷

Studies have also been performed to show how the embedding medium affects the resonant behavior of the nanoshells. As is well known, a redshift on the resonant wavelength appears as a consequence of an increased refractive index of the medium. However, this change seems to be more noticeable for bigger particles. Small nanoparticles within the dipole regime also show an enhanced extinction, a behavior not observed for the bigger ones. The quadrupole mode also increases its contribution as compared to the dipolar one with increasing refractive index, as a consequence of the shorter optical wavelength.^{6,7}

The highly tunable response of nanoshells results in well-separated frequency peaks that constitute a ‘fingerprint’ of these nanostructures. The control on the far field response is also linked to a ‘designed’ near-field response, that can be used for SERS.¹ Besides, the fact that their resonances can be tuned by shifting

them into the NIR means that one can fabricate nanoshells with resonant wavelengths in the ‘water window’, where the tissue and blood are transparent and light can penetrate more than 10 cm. This is of clear interest in biomedical applications.^{7,8}

4.1.2. Open nanoshells: semishells, nanocaps, nanocups, etc

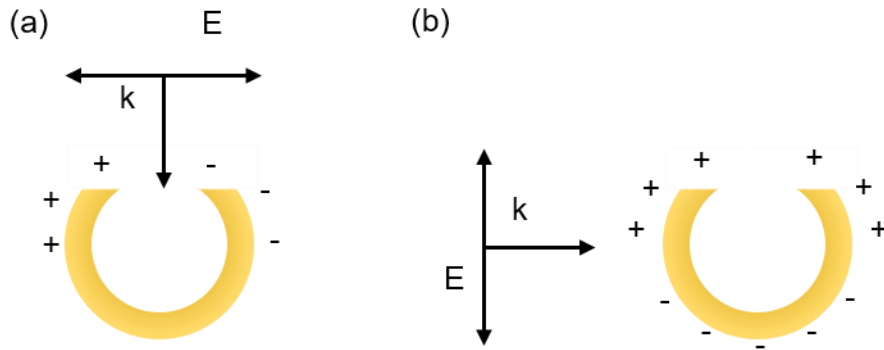


Figure 4.2 Dipolar modes in open nanoshells: (a) transverse mode (b) axial mode, adapted from Ref. 24.

When the nanoshells are opened, symmetry is broken and the plasmon properties are dramatically modified. This is the case of semishells, nanocaps, nanocups, nanobowls and other types of structures, all of them having in common the basic structure: a nanoshell structure with an aperture.^{4,16,18,20,22,24,25,29} Symmetry breaking induces the appearance of new hybridized modes and a dependence of the optical response on the polarization. In particular, the single peak characteristic of small core-shell nanostructures splits into two peaks corresponding to transverse and axial modes. While the charges around the rim of the nanocups tend to repel each other causing a blueshift in the axial dipole, the energy of the transverse dipole is lowered because opposite charges at the rim attract each other.⁹

Consequently, they have two bonding dipolar resonances (see Figure 4.2): one parallel to the axis of symmetry (axial mode) and another one perpendicular to it (transverse mode). The later presents a strong magnetic component due to the fact that the electric field excites a current loop in the metallic shell,^{23,24} analogue to that of split-ring resonators.^{30,31} As compared to the resonant wavelength of the complete nanoshell, the open shells present a blue shifted axial resonance and a redshifted transverse one.

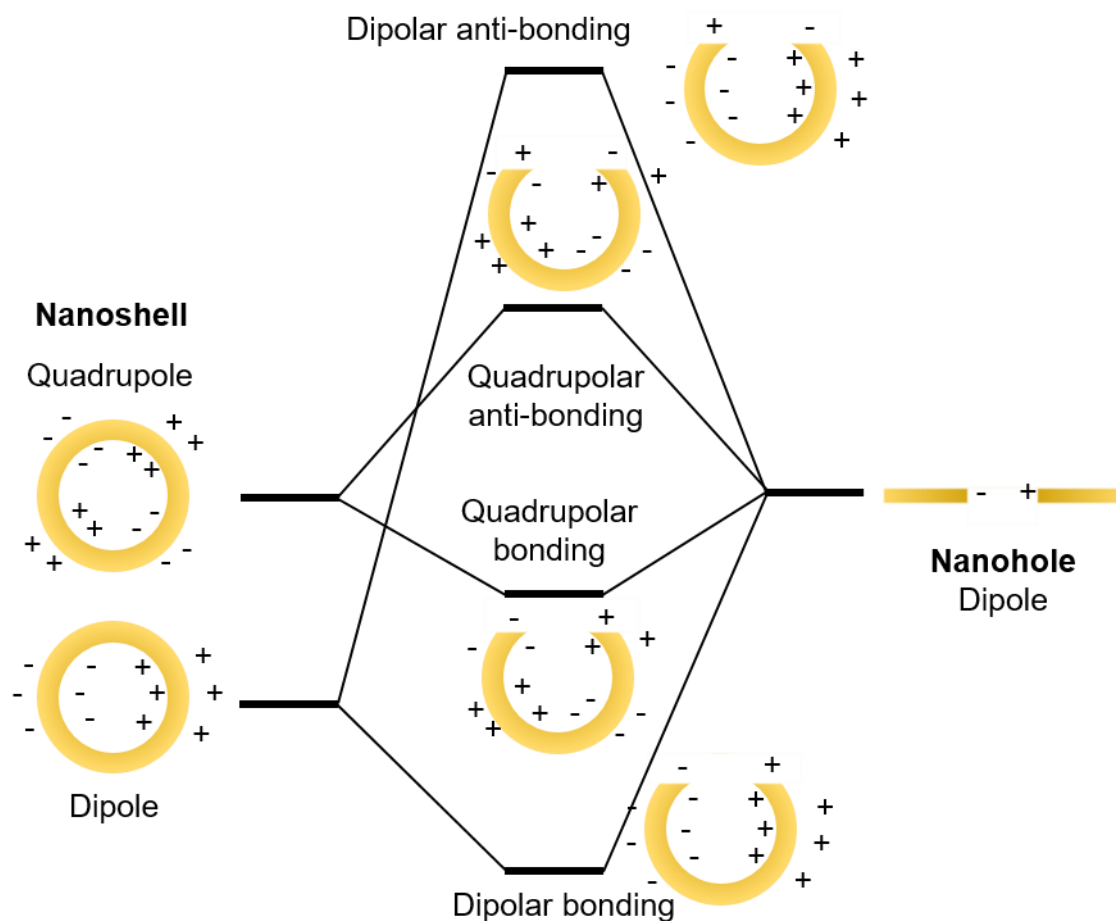


Figure 4.3 Hybridization model for open shells in the transverse model, adapted from Ref. 20.

Also, the scattering properties are strikingly different. While for the axial mode the scattering direction is mainly dependent on the angle of incidence, for the transverse mode, the geometry dominates its behavior and the scattering is always parallel to the symmetry axis. Moreover, while symmetric nanoshells have a scattering pattern that depends on the polarization and the angle of incidence, open shells exhibit maximum scattering for an excitation either parallel to the symmetric axis for the transverse mode or parallel to the substrate for the axial mode, as the dipoles are fixed due to the broken symmetry.^{20,24} For a thorough study of the changes in the far-field response, one can refer to Refs. 20 and 24.

Yet, the transverse mode will be the only one excited for symmetric nanostructures placed on a substrate with the aperture looking upwards and the incident source perpendicular to the substrate (such as ours). Therefore, from here on, only transverse excitation will be studied. According to the

hybridization model (see Figure 4.3), one can understand the transverse modes of nanocups as the hybridization between the dipole resonance of the rim with the bonding mode of the nanoshell, resulting in charge accumulation at the edges of the rim and large field enhancements. This behavior is reflected in the far-field spectra as a strong redshift of the resonance as a consequence of charge build up in the aperture. As it happens in nanoshells, a decrease in the thickness gives rise to a redshift of the plasmon resonance due to an increased interaction between the inner and outer shell surfaces which is associated with a lower energy level.

Regarding the near-field response, open shells show interesting enhanced localized electric fields under suitable excitation. Dipolar resonances (featured as the longest wavelength peaks in the far-field spectrum) are characterized by charge build-ups in the edges of the aperture that translate into hot-spots, *i.e.*, regions with high electric field enhancement. Quadrupole modes (typically associated with peaks in the VIS) show a weaker behavior, with enhancements of the electric field in the top and bottom corners of the cavities.^{16,20}

Besides, this type of structures present an additional geometric parameter to tune (as compared to complete nanoshells): the height of the remaining portion of the sphere that can help to further engineer their response, as shown in Ref. 20.

4.1.3. Our system: hollow cylindrical nanocups

Most of the nanoshells and open nanoshells are prepared by chemical synthesis or using polymer spheres as template. Consequently, they have spherical shape. In our case, we are studying the response of cylindrical nanostructures that have a key difference with respect to spherical nanoshells: the diameter of the cavity is kept constant along its height, which can be tailored to have samples covering a wide range of aspect ratios. This fact has important consequences in the optical response of the system that will be discussed later. From now on, the term nanocup will define a hollow cylindrical nanostructure with a thin shell thickness.

Except otherwise specified, along this chapter, single nanocups and periodic structures were normally illuminated by a total-field scattered-field (TFSF) source and a plane wave, respectively, being the electric field in both cases parallel to the x -axis. Perfectly-matched layers (PMLs) were used in the three axes as the radiation boundary conditions for single elements, while periodic

conditions were used for the x - and y -axes to simulate arrays of structures. Symmetric and antisymmetric boundary conditions have also been used to further reduce the calculation to a quarter of cell when possible. The dielectric constant of Au was fitted to the experimental data from Johnson and Christy³² while for Ti and SiO₂, the data of Palik³³ were used, all of these values taken from the data base of Lumerical.³⁴ The relative dielectric constant of the background is fixed to 1. The experimental characterization was done by FTIR measurements and UV-VIS spectrophotometry with an integrating sphere.

Besides, as pointed out previously, our nanocups are grown on a substrate and the experiments were done with normal illumination; therefore, all the simulations shown along Chapter 4 will be carried out with an excitation perpendicular to the substrate to excite the transverse mode, just as shown in Figure 4.2(a).

4.2. The choice of the material

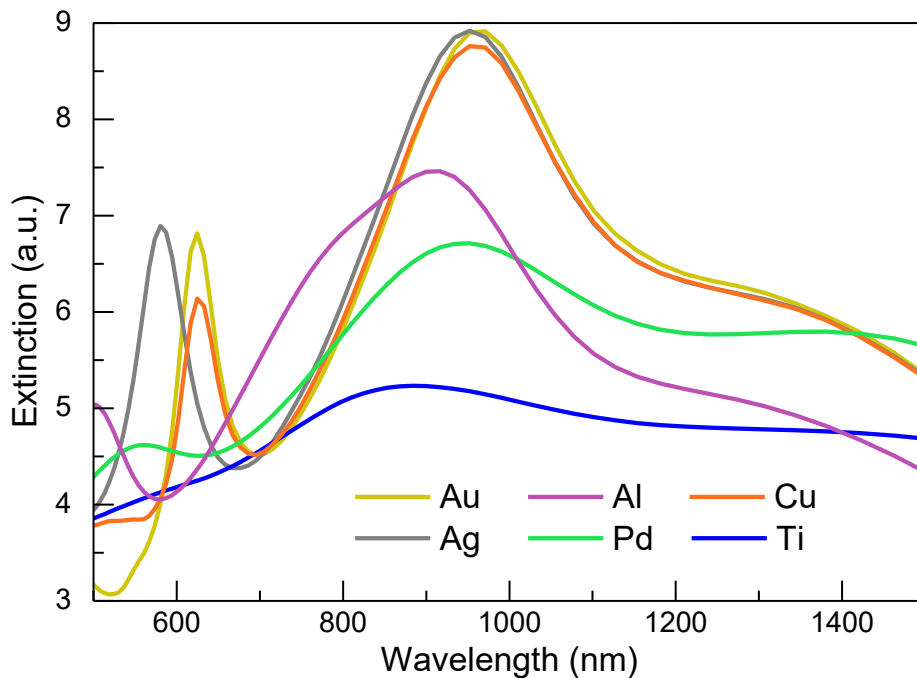


Figure 4.4 FDTD simulated extinction for nanocups with $h=d=400$ nm and $h=30$ nm made of different materials. For the sake of simplicity, no substrate has been used in these simulations.

Simulations have been done to seek the most suitable material for the plasmonic response of nanocups. Figure 4.4 shows the FDTD simulated extinction for a nanocup of 400 nm height (h) and diameter (d) and 30 nm wall

and base thickness (t), without substrate, for different materials. The dielectric constants of Al, Ag and Pd were taken from Palik³³ and CRC data were used for Cu.³⁵ Results show that Au, Cu and Ag present two well defined peaks in the visible and NIR regions of the spectrum, respectively. The feasibility of these materials was already commented on Chapter 1. In this work, due to its inert behavior, we have focused on Au. However, if protected with a dielectric layer, Cu and Ag would also provide good results. Ti, that has been used in the manufactured samples to promote adhesion, shows however a very poor response, fact that should bear in mind during the fabrication process in order not to spoil the optical response of the nanostructure.

4.3. Tunability of the plasmonic response as a function of the height, diameter and thickness of the nanocup

As in the cases of nanoshells and open shells, our hollow cylindrical nanocups show a highly tunable response under electromagnetic excitation. In the following, a thorough study of the plasmonic response as a function of the geometric parameters (h , d , t) of the nanocup will be discussed.

4.3.1. Far-field spectra

Thickness

Figure 4.5 (a) shows the extinction calculated for nanocups with $h=d=400$ nm and several wall and base thicknesses (t). It can be inferred from Figure 4.5 (a) that our nanocups follow the expected trend: a redshift is shown in the peaks when decreasing the thickness of the walls as a consequence of the increasing interaction between the modes inside and outside the cavity, with different intensities of the peaks coming from competing interactions.^{3,24} Besides, a decrease in the thickness results in the appearance of a higher order peak (for $t<20$ nm), that could be assigned to the polarization of the wall itself.

Height

Figure 4.5 (b) shows the extinction spectra for nanocups with $d=400$ nm and $t=30$ nm and height ranging from 100 to 800 nm. For the case of 100 nm, only a dipolar peak is observed. An increase in the height is accompanied by the appearance of new peaks at increasingly high energies corresponding to higher order modes, while the existing ones are redshifted. These results are in good

agreement with previous ones reported for the case of Au semishells, nanobowls and nanocages.^{18,20}

Diameter

Figure 4.5 (c) presents the extinction spectra for nanocups with $h=400$ nm $t=30$ nm and different values of d . For $d=100$ nm, only one peak is observed. For $d>200$ nm, the extinction spectra have two maxima, that are both redshifted for increasing d . However, a stronger dependence of the red shifting on d is observed for the lower energy peak, fact that agrees well with previous results for semishells.²⁹

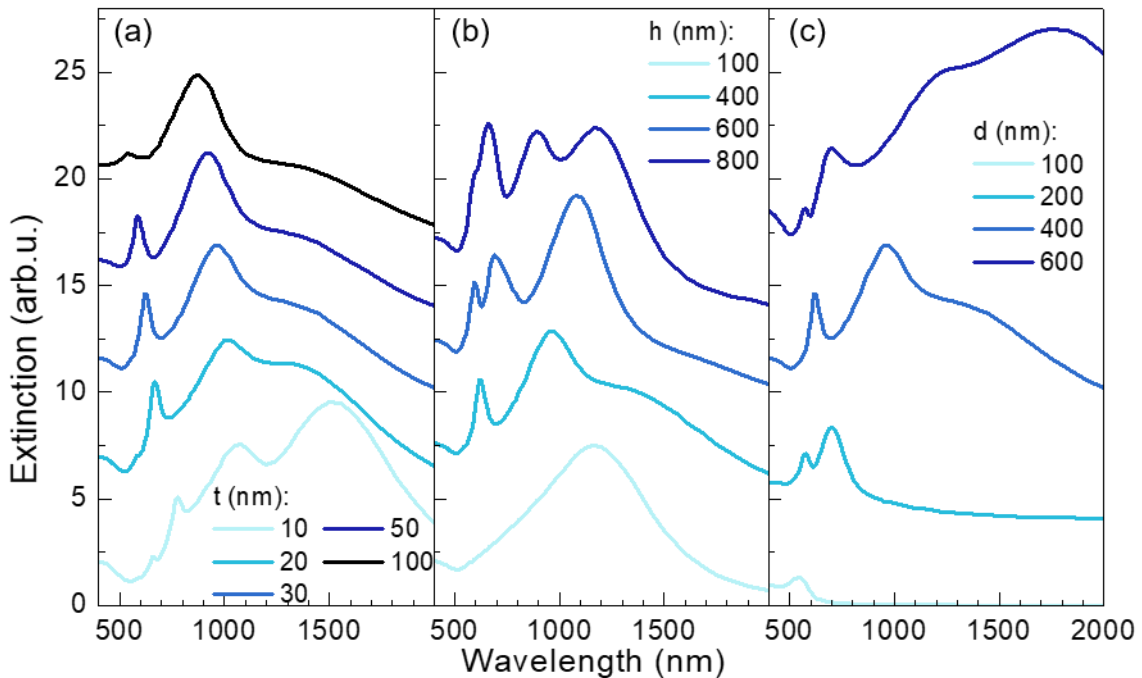


Figure 4.5 FDTD simulated extinction for a Au nanocup for several values of: (a) the diameter, (b) the height and (c) the wall and base thicknesses, being $h=400$ nm, $d=400$ nm and $t=30$ nm the reference values for each one of the three panels where two of these parameters are kept constant. For simplicity, no substrate has been used in these simulations.

4.3.2. Near-field response

To gain a further insight into the peaks in the far-field spectra, on-resonance distributions of the electric field of the nanostructures have been simulated to analyze the nature of the modes and the enhancement they exhibit.

Au nanocups as tunable optical nanoresonators

Here, two particular cases are compared: 200/200/15 and 400/400/30 nm ($d/h/t$) nanocups that will be referred to hereafter as the 200 and the 400 nm nanocups. The extinction spectra for both cases are shown in Figure 4.6. For the 200 nm case (red curve), two peaks appear: a small and narrow peak at higher energy (649 nm) and a larger and much broader one at lower energy (873 nm). When the size is doubled (black curve), the modes shift to lower energies and a higher order mode emerges, resulting in two well defined peaks (622 nm and 968 nm) and a broad peak around 1364 nm. The spatial distribution of the electric field has been calculated for the maxima of the extinction marked as points A and B in Figure 4.6 (a).

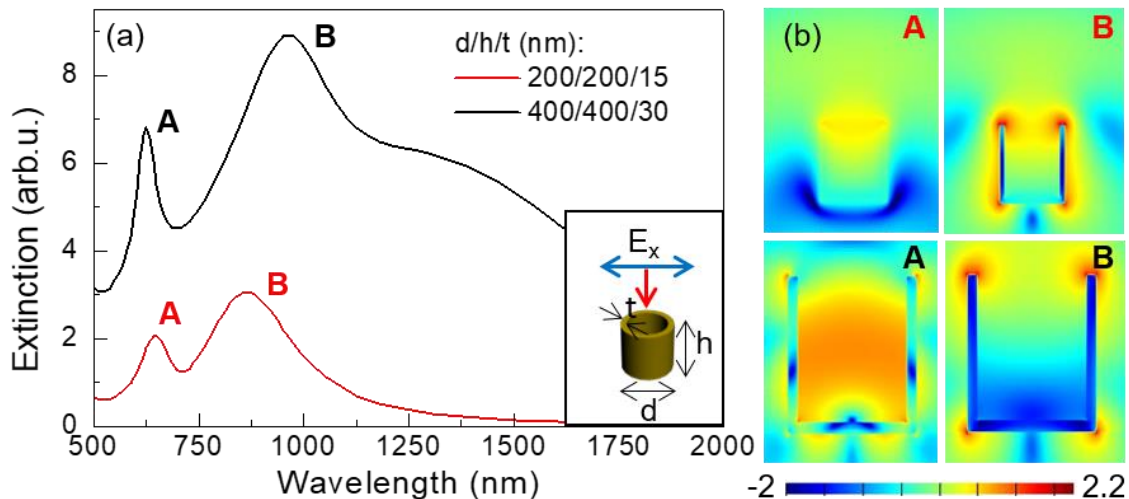


Figure 4.6 (a) FDTD simulated extinction for a $d=h=200$ nm and $t=15$ nm Au nanocup (red curve) and one double in size, i.e. $d=h=400$ nm and $t=30$ nm thickness (black curve). The inset shows the configuration of the incoming wave. (b) $\text{Log}(|E|^2/|E_0|^2)$ for the maxima marked in (a), in cross section view. Top pannels in (b) correspond to the 200 nm nanocup, while bottom pannels correspond to the 400 nm case. For simplicity, no substrate has been used in these simulations.

Figure 4.6(b) shows that for lower energies, both cases look similar and the electric field is enhanced in the outer parts of the walls, upper rims and corners in the base. However, for the higher energy peaks we can see a significant difference. For the 200 nm case, a strong evanescent decay can be observed along the propagation axis inside the cavity, and only the upper rims and upper part of the cavity are excited. However, for the 400 nm case and for certain values of the wavelength, the wave is able to penetrate and excite the modes inside the cavity. This internal excitation of the cavity only takes place when

both the internal diameter and height are greater or equal than half the incident wavelength.

This homogeneous enhancement of the field within the cavity is not previously reported in open nanoshells due to two main reasons. First, simulations mainly deal with structures within the dipolar approximation limit. However, to observe this behavior in the optical spectrum, one has to go far beyond this regime, so that the cavity is big enough for the wavelength to penetrate and excite the modes inside the cavity. Secondly, most of the studied structures have a spherical shape that does not allow for a homogeneous distribution of the electric field throughout the cavity. This can be observed for example in Ref. 36, where it can be seen that spherical plasmonic voids present also a resonance inside the cavity but with an enhancement of the electric field limited to a small volume of the cavity, where the geometric parameters are the appropriate ones for the resonance to take place.

Near field response as a function of the geometry

Figure 4.7 displays the charge distribution and electric field enhancement ($\text{Log}|E|^2/|E_0|^2$) for nanocups with $d=400$ and $t=30$ and for three different heights ($h=100, 400$ and 800 nm). Figure 4.5(b) showed that, for $h=100$ nm, the extinction spectra only displayed one peak. Figure 4.7 (a) illustrates the dipolar character of the peak, with enhancements of the electric field in the outer walls, upper rims and corners of the base, in accordance with previous results for open nanocages.³⁷ The dipolar peak is shifted from 1167 nm for $h=100$ nm to 1365 nm for $h=400$ and suppressed for $h=800$ nm. For $h=400$ nm, the structure presents a quadrupole peak at 968 nm, that is shifted to 1180 nm for $h=800$ nm. The electric field for the quadrupole peak is mainly concentrated in the aperture and the base corners, also in accordance with nanocages.³⁷ For the cases of 400 and 800 nm, there are higher order modes whose charges and electric fields are also displayed in Figure 4.7. However, it is worth mentioning that the highest energy peak (622 nm) of the $h=400$ nm structure, presents an enhancement of the electric field inside the cavity that is not found for other geometries such as the case of 800 nm. The reason for this is that when both the diameter and height are of the order of the incident half wavelength, a kind of resonance phenomenon takes place, giving rise to this large and intense field enhancement within the cavity.

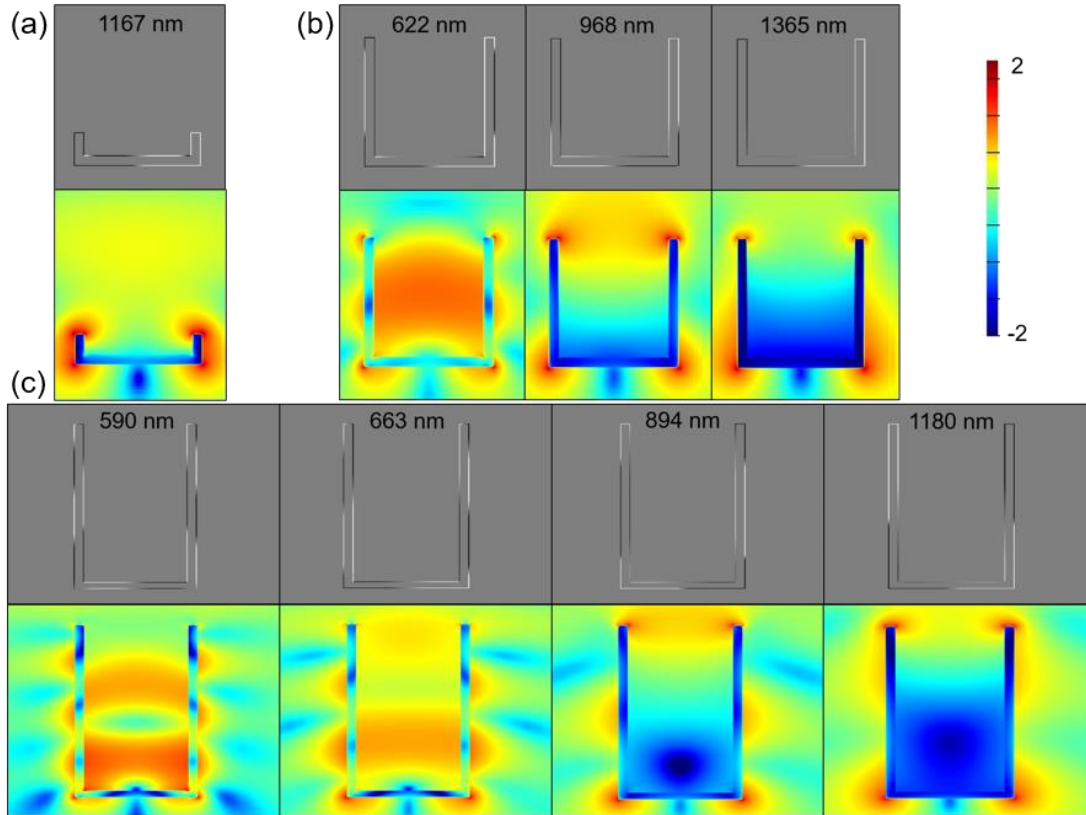


Figure 4.7 On-resonance charge (grey-scale pannels) and electric field distribution ($\text{Log}|E|^2/|E_0|^2$) (colored pannels) for nanocups with $d=400$ nm, $t=30$ nm, as a function of h : $h=100$ (a), $h=400$ nm (b) and $h=800$ nm (c), corresponding to the maxima in the extinction spectra shown in Figure 4.5(b). Cross section views are displayed.

4.4. The effect of the adhesion layer

Simulations have been performed to analyze the effect of the adhesion layer in the optical properties of cup-shaped nanostructures. Geometric parameters ($d=h=400$ nm and $t=30$ nm) have been chosen to be similar to fabricated samples. Only the thickness of Ti, and therefore the total base and wall thickness is varied. Also, for an easier analysis, no substrate has been used in the simulations. Figure 4.8 shows the different behavior of nanocups for no Ti, 5 nm and 10 nm of Ti. While the lower energy peak, labeled as B , seems to be barely affected with just a slight redshift and small decrease of the intensity when the Ti thickness is increased, the highest order peak (A) is drastically reduced and blueshifted with increasing Ti thickness. A similar effect is also observed in the electric field distribution (Figure 4.8(b)), especially for shorter wavelengths as expected due to the fact that the dielectric functions of metals

are increasingly negative.³⁸ We point out that, although in the fabrication process the deposited layer of Ti is of 5 nm, the final thickness of Ti in the nanostructures is much lower, therefore optical properties should not be so affected.

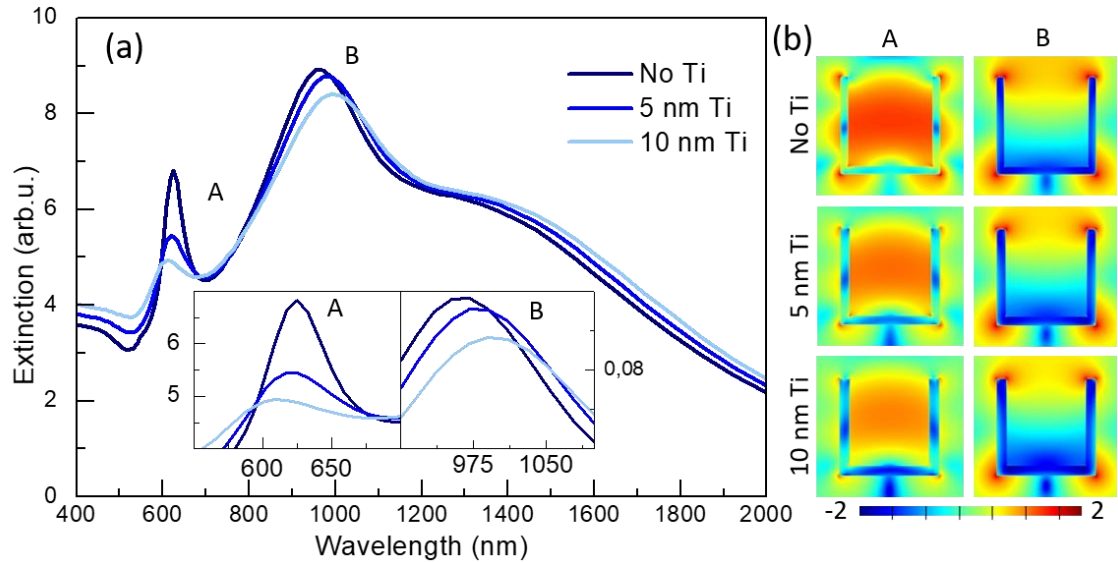


Figure 4.8 (a) FDTD simulated extinction for a $d=h=400$ nm and $t=30$ nm Au nanocup without and with 5 nm and 10 nm Ti adhesion layer. For simplicity, no substrate has been used for these simulations. The insets show a zoom of the peaks. (b) $\text{Log}(|E|^2/|E_0|^2)$ corresponding to the maxima in the extinction spectra.

4.5. The effect of the substrate and the embedding medium

For the sake of simplicity, the results shown up to now disregard the effect of the substrate on the analysis of the different parameters. However, this is, in general, a key point to understand most of the plasmonic systems.

When a plasmonic nanoparticle is on top of a dielectric substrate, the dielectric material screens the electromagnetic field, being this screening equivalent to the potential generated by a mirror image of the nanostructure reduced by a factor $(\epsilon-1)/(\epsilon+1)$, where ϵ is the permittivity of the substrate. Therefore, dielectrics with higher permittivity give rise to bigger interactions. One can understand this effect as the hybridization of the nanostructure with the “image” of the nanostructure in the substrate. The shift in the resonance produced by the substrate is also directly linked to the strength of the structure-substrate interaction.³⁹

An increase in the refractive index of the environment results in a redshift of the resonance due to the larger polarizability of the medium, and hence a reduction in the restoring force of the electron oscillations that shifts the resonances to lower energy levels.¹⁶

4.6. Optical characterization of the nanocups

A $1 \times 1 \text{ cm}^2$ square array formed by Au nanocups with a diameter of 400 nm, lateral wall thickness of about 30 nm and a pitch of 800 nm have been fabricated onto a $170 \mu\text{m}$ thick glass substrate (Carl Roth GmbH).

The optical spectra of absorbance and transmittance of the array have been recorded using an UV and visible spectrophotometer (Specord 205, Analytic Jena). Measurements have been repeated on several spots of the same sample and on similar samples in order to check their reproducibility. The scattering spectra of the nanocup arrays were calculated by subtracting the optical spectra for the absorbance and transmittance.⁴⁰ The scattering spectrum for the uncoated array of Au nanocups shown in black in Figure 4.9 exhibits some distinguishable features such as two peaks located circa 670 and 780 nm, and a rounded shoulder centered at about 930 nm. All these elements of the scattering spectra are overlapped to yield a broad, smooth optical response because of a poor signal of the plasmonic system.

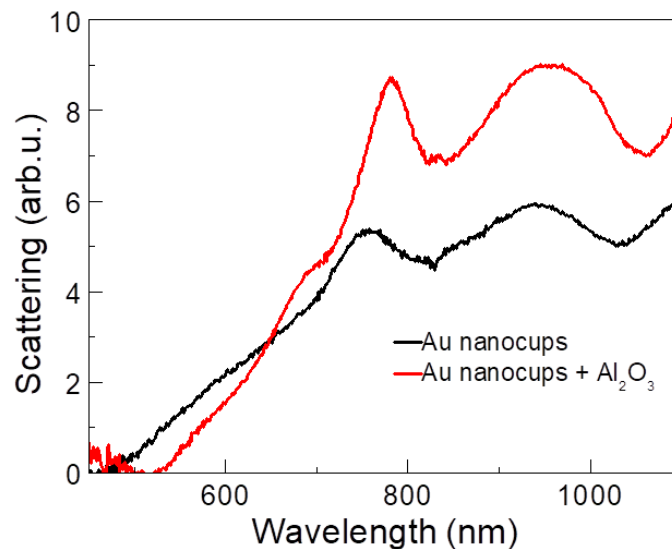


Figure 4.9 Scattering obtained by UV-visible spectrophotometry for an array of Au nanocups with $d=h=400 \text{ nm}$ and $t=30 \text{ nm}$ (black), and for a sample with the same characteristics but also coated with 10 nm of Al_2O_3 (red).

It is known that surface plasmon modes are sensitive to changes of the dielectric constant of the metal environment. Consequently, the scattering signal is enhanced by coating the Au nanocup with a 10 nm Al_2O_3 layer deposited by atomic layer deposition (ALD). ALD presents the advantage of conformal deposition, allowing one to cover uniformly both the inner and outer walls of the nanocup. A significant increase in the scattering signal together with much better definition of the spectral features are obtained for the Al_2O_3 -coated nanocup array shown in Figure 4.9. Two well-defined peaks are now located around 780 nm and 960 nm, that is, redshifted with respect to the non-coated response in accordance with theory.¹⁶ Also, these results are in agreement with the simulations in Figure 4.6. The differences between the experimental and the simulated results may be due to the use of the Ti adhesion layer, slight size changes between the original design and the actual sample, and roughness and porosity.

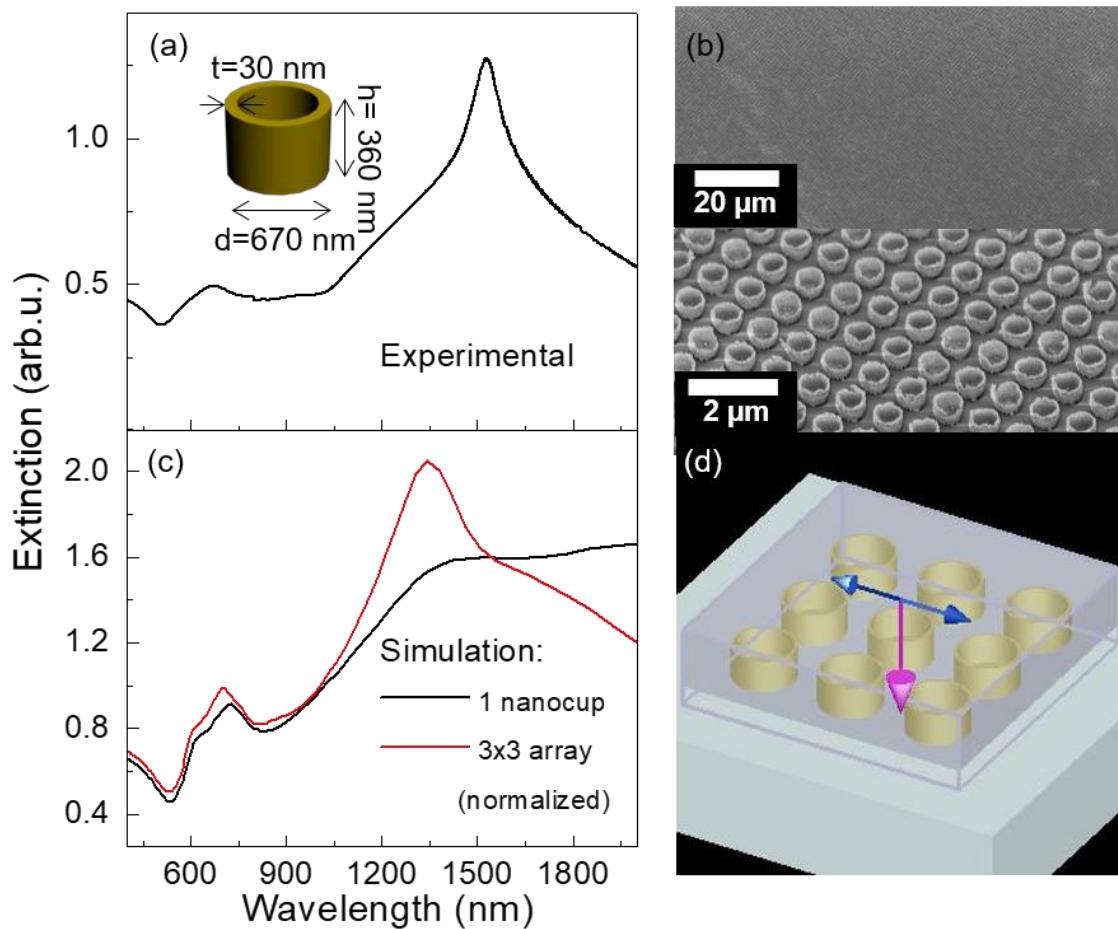


Figure 4.10 (a) FTIR spectra of the sample shown in the SEM micrographs in (b). (c) FDTD simulations for a single structure and an array of 3x3 nanostructures with the dimensions of the sample in (a) and (b). (d) Sketch of the simulations in (c).

It is worth noting that this technique uses unpolarized light, while in the simulations the excitation source was a plane wave propagating along the z -axis with the electric field parallel to the x -axis. However, due to the symmetry of the system, it is clear that the response under the excitation of a field parallel to the x - or y -axis would be the same, and one can conclude that the experimental measurements and simulations can be compared.

The same mold was used to fabricate samples with a bigger diameter, meaning therefore a smaller gap between neighboring elements. Figure 4.10(a) shows the FTIR measurement for a sample of 670 nm and a pitch of 800 nm (Figure 4.10(b)), meaning therefore that the gap between nanocups is reduced to 130 nm. Figure 4.10(a) shows a sharp peak around 1500 nm. Figure 4.10(c) shows the simulation results for a single nanocup (in red) and a 3×3 array of nanocups (in black) of the same dimensions of the experimental sample shown in Figure 4.10(b). It is clearly seen that the peak displayed in the experimental measurement is only present in the simulation of the array. Hence, one can conclude that this is due to interparticle interactions through the local dipolar polarization of the gaps between neighboring nanocups.

4.7. Plasmonic perfect absorbers

4.7.1. Metamaterial perfect absorbers

Since perfect absorption was first demonstrated in 1976,⁴¹ and specially in the last decade, the field of plasmonic absorbers has experienced a thriving development. Today, perfect absorbers with angle or polarization independence and for a broad range of frequencies from optical to microwaves frequency are being studied.^{38,42-51}

Metamaterials are artificial systems made of metallic nanostructures that are replicated to form a material, whose properties arise from the oscillating electrons in the nanostructures but whose response can be considered as a bulk homogeneous medium characterized by complex electric permittivity ($\epsilon(\lambda)$) and complex magnetic permeability ($\mu(\lambda)$). These two magnitudes can be retrieved from the effective medium theory.⁴³ By properly designing metamaterials, novel properties which are not allowed in natural materials such as negative refractive index,³¹ cloaking devices⁵² or perfect absorbers can be realized.^{38,42-51}

Perfect absorption is achieved by using a metal-insulator-metal (MIM) configuration, consisting in a bottom metallic layer that is optically thick (to prevent transmission), a dielectric spacer, and metallic nanoelements supporting LSPR on top, designed in such a way that, for certain values of the parameters, the system behaves as perfect absorber ($A=1$).^{38,42,44-51} At resonance, antiparallel currents are excited in the nanostructures and the film, electromagnetic energy is confined in the spacer, and a resulting magnetic moment due to the circulating currents arises.⁴⁵⁻⁵⁰

To understand the underlying physics of a perfect absorber, typically two different approaches can be used. The first one is the use of impedance matching^{42,45} for which the three-layer stack is considered as a whole and, by carefully choosing the geometric parameters, $\varepsilon(\lambda)$ and $\mu(\lambda)$ can be adjusted in such a way that the system's complex impedance matches that of vacuum ($Z=(\mu/\varepsilon)^{1/2}=\mathbf{1}$) resulting in zero reflection. Since transmission is suppressed by the underlying metallic film, perfect absorbance can be obtained ($A=1-R-T=1$).⁴⁶⁻⁴⁸ In the second approach, the nanoelement layer and the metallic film are considered as two decoupled surfaces, and the enhanced absorption comes from the superposition of multiple reflections between the two metallic systems that destructively interfere leading to zero reflection.^{38,47,48} Then, the system behaves as a Fabry-Perot cavity formed by the film and the metallic nanostructures.⁴⁸ According to classical EM waves theory, the maximum constructive interference can be achieved for:

$$z_{max} = 2 \left(m + \frac{1}{2} \right) \frac{\lambda}{4n_{\lambda} \cos \theta_n} - \delta_n$$

where z_{max} is the dielectric thickness for maximum constructive interference, m is the mode order (0, 1, 2, ...), λ is the incident source wavelength, n_{λ} is the refractive index of the spacer layer at λ , θ_n is the angle of the incident beam within the spacer, and δ_n accounts for the penetration depth of the reflecting material. Therefore, if $m=0$, for low-refractive index films and small angles, one reaches the well-known quarter-wavelength dependence.³⁸ However, when nanostructures are present, the process has to be optimized to account for

interference effects,³⁸ and different values of the thickness have been used depending on the case.

In this way, the MIM structure confines light in the form of SPPs within the spacer layer and leads to Fabry-Perot resonances perpendicular to the film.

Absorbers can be divided in two main groups: resonant and broadband absorbers, depending on whether we want either a sharp high absorption field for a certain wavelength for filtering and sensing applications or high absorption along a wide range or frequencies, such as for example for photovoltaic applications.

4.7.2. Nanocups as perfect absorbers

Here, we use a bottom thick Au layer and a 100 nm thick SiO₂ spacer layer on top of which the lithographic pattern is created.

FTIR spectroscopy has been used to characterize the response of our nanostructures. These measurements were performed with a FTIR spectrophotometer with an optical microscope (Vertex 70 and Hyperion, Bruker, from the group of Dr. A. Mihi, at ICMAB-CSIC) with a 4x objective and unpolarized light.

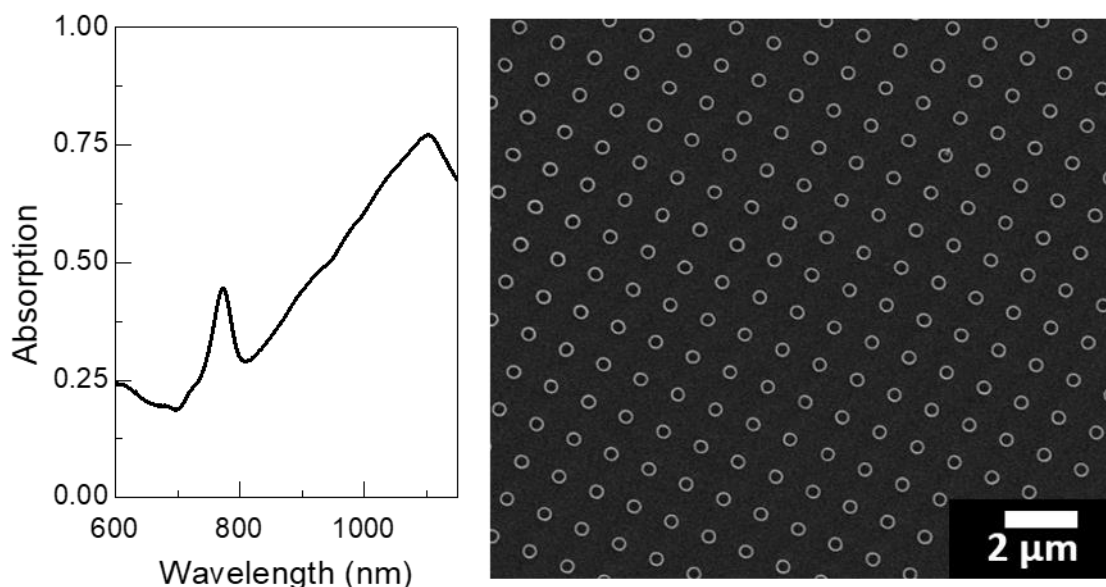


Figure 4.11 Absorption measured by FTIR spectroscopy (left) and SEM micrographs of the corresponding sample consisting of an array of nanocups with a pitch of 2.4 μm.

Figure 4.11 shows the absorption spectrum and a SEM micrograph of an array of nanocups with $d=370$ nm, $h=470$ nm and $t=20$ nm, and with a pitch of $2.4 \mu\text{m}$. The spectrum shows two peaks, a broader peak around 1100 nm and a less intense but sharper one at 785 nm.

However, when the pitch of the system is decreased the absorption peaks strongly broaden. Figure 4.12 displays the absorption spectrum of a sample with a pitch of 600 nm, $d=370$ nm, $h=470$ nm and $t=20$ nm. The measurements reveal these structures behave as broadband perfect absorbers on the visible region, reaching absorption rates above 80% of the total incoming light in the range of 400 to 1000 nm.

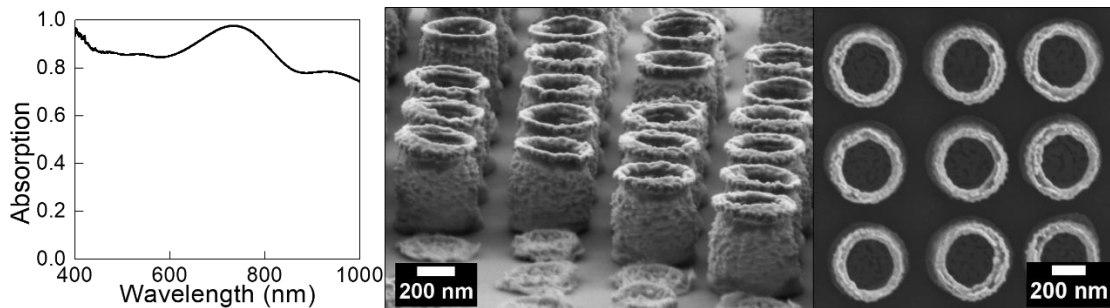


Figure 4.12 Absorption measured by FTIR spectroscopy (left) and SEM micrographs of the corresponding sample consisting of an array of nanocups of $(600 \text{ nm}, 370 \text{ nm}, 470 \text{ nm}, 20 \text{ nm})$, (pitch, d , h , t) with MIM configuration (100 nm spacer).

4.8. Possible applications of Au nanocups

In the following three sections, some examples of possible applications of the Au nanocups will be discussed, including their potential use for enhanced spectroscopies and as sensing platforms.

4.8.1. Surface Enhanced Raman Spectroscopy

As discussed in Chapter 2, Au films and nanostructures have been widely used to enhance the low-efficiency of Raman Spectroscopy (RS). Nanocups are interesting structures for this application thanks to the large enhancement of the electric field either in the upper rim or inside the cavity. The wavelength of these resonances can be tuned as a function of the geometric parameters to match one of the excitation lasers of the RS system. In fact, there were promising results reported for the case of Au semishells.^{53,54}

4.8.2. Surface Plasmon Resonance sensing

The results of the simulations (see Figure 4.13) yield changes on the order of $8 \cdot 10^2$ /RIU (refractive index units) for the visible and $9 \cdot 10^2$ /RIU for the IR peak that can be obtained by changing the refractive index of the embedding medium. Therefore, these structures could be used as platforms for LSPR sensing.

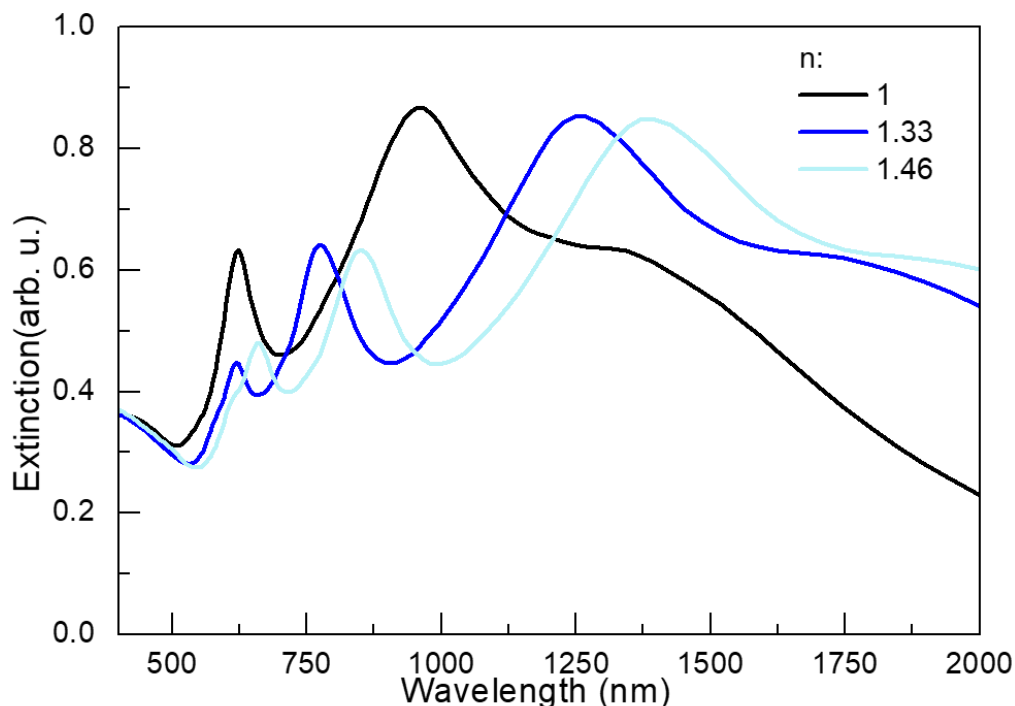


Figure 4.13 FDTD simulated extinction for a $d=h=400$ nm and $t=30$ nm Au nanocup with embedding media with three values of the refractive index.

4.8.3. Gas sensing

Different types of hydrogen sensors that are able to detect hydrogen below the lower explosion limit of 4% at room temperature have been studied. In particular, it is well known that, under the presence of hydrogen, Pd and Mg transform into PdH_x and MgH_2 with an increase in volume, which can be used to sense the presence of hydrogen.^{46,55}

FDTD simulations were done filling the cavity of the nanocups with Pd and Mg. Figure 4.14 compares the extinction spectra for an empty nanocup and one filled with 80 nm of Pd. Under the presence of hydrogen, Pd will turn into PdH with an increase in volume. This results in a change in the position and

intensity of the peak in the visible range providing a way of sensing the presence of hydrogen, while the other peak, that is not significantly affected, can be used as reference.

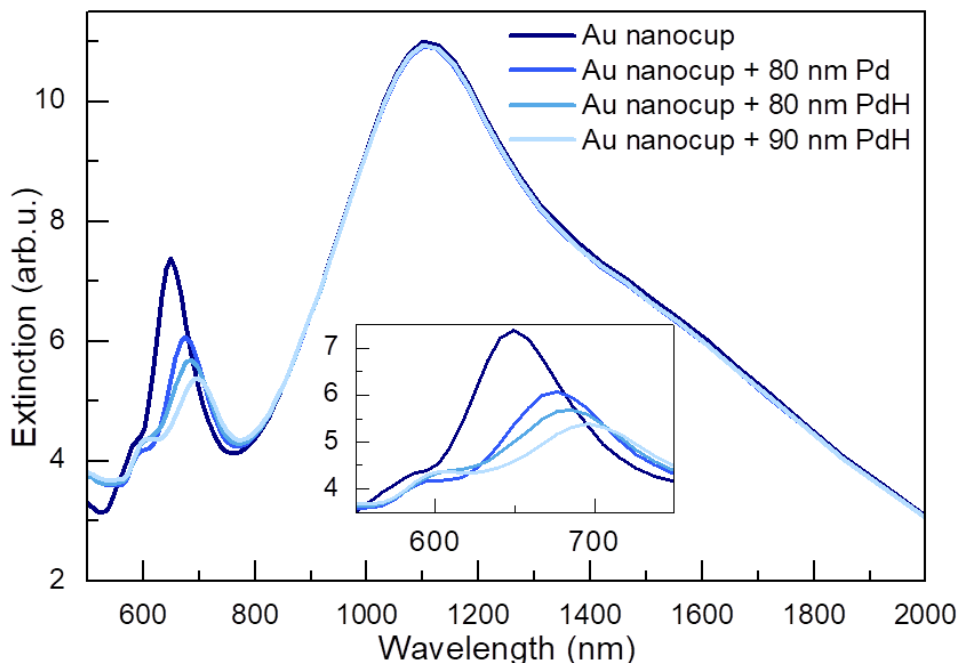


Figure 4.14 FDTD simulated extinction for a $d=h=400$ nm and $t=30$ nm Au nanocup empty, filled with 80 nm of Pd, with 80 nm of PdH and with 90 nm of PdH taking into account the increase in volume when Pd turns to PdH.

4.9. Conclusions and further work

Along this chapter, we have studied the plasmonic response of gold nanocups, both through simulations and experimental measurements. Nanocups showed a big tunability as a function of the geometric parameters, a fact that can be used to tune their response, for example, to match one of the typical wavelengths of the lasers used for SERS (785 nm).

FTIR and UV-VIS spectrophotometry were used to characterize the samples, showing good agreement with simulations. The use of a MIM configuration resulted in very high absorption within the 400-1100 nm range for high density arrays of nanocups, while for larger values of the pitch the spectra exhibited two peaks as in the case of glass substrates.

As further work, it could be of interest to fabricate multilayered nanocups, either to have multi-functional nanostructures, for instance, with a

ferromagnetic layer (magneto-plasmonic coupling), or to give rise to several resonances combining different plasmonic materials. As a matter of fact, the fabrication of multishell nanostructures combining materials with different functionalities (optical and magnetic) has already been used to control the particles' motion. In particular, a combination of magnetic and nonmagnetic materials (Au, Ag and Fe) has been used to control the position and orientation of SERS nanoprobles.⁵⁶ This is completely compatible with our fabrication process, where we could simply sputter different materials to grow multi-layered structures without increasing the difficulty of the fabrication process. Also, following the idea of nanomatryoshkas,¹¹ multilayered cups with alternated plasmonic and dielectric layers could be fabricated.

There are also some details that remained unexplored along this manuscript, such as the effect that roughness - which is expected to broaden the peaks and induce a slight redshift-,^{17,57,58} imperfections – e.g., having an irregular rim that would probably result in a broadened attenuated and redshifted resonance,¹⁷ grain size, and non-crystalline metallic nanostructures may have on the optical response of the nanostructures.^{58,59} We note that many studies report that these effects basically worsen the optical response, by making it less intense and broader.^{17,57-59}

4.10. References

1. Halas, N. The Optical Properties of Nanoshells. *Opt. Photonics News* **13**, 26 (2002).
2. Averitt, R. D., Westcott, S. L. & Halas, N. J. Linear optical properties of gold nanoshells. *J. Opt. Soc. Am. B* **16**, 1824 (1999).
3. Frederiksen, M., Bochenkov, V. E., Cortie, M. B. & Sutherland, D. S. Plasmon Hybridization and Field Confinement in Multilayer Metal–Dielectric Nanocups. *J. Phys. Chem. C* **117**, 15782–15789 (2013).
4. Ye, J. *et al.* Plasmonic Modes of Metallic Semishells in a Polymer Film. *ACS Nano* **4**, 1457–1464 (2010).
5. Oldenburg, S. ., Averitt, R. ., Westcott, S. . & Halas, N. . Nanoengineering of optical resonances. *Chem. Phys. Lett.* **288**, 243–247 (1998).
6. Tam, F. & Halas, N. Plasmon response of nanoshell dopants in organic films: a simulation study. *Prog. Org. Coatings* **47**, 275–278 (2003).
7. Halas, N. Playing with Plasmons: Tuning the Optical Resonant Properties of Metallic Nanoshells. *MRS Bull.* **30**, 362–367 (2005).
8. Wang, H., Tam, F., Grady, N. K. & Halas, N. J. Cu Nanoshells: Effects of Interband Transitions on the Nanoparticle Plasmon Resonance. *J. Phys. Chem. B* **109**, 18218–18222 (2005).
9. Lassiter, J. B., Knight, M. W., Mirin, N. A. & Halas, N. J. Reshaping the Plasmonic Properties of an Individual Nanoparticle. *Nano Lett.* **9**, 4326–4332 (2009).
10. Jian, Z., Jian-jun, L. & Jun-wu, Z. Tuning the Dipolar Plasmon Hybridization of Multishell Metal–Dielectric Nanostructure: Gold Nanosphere in a Gold Nanoshell. *Plasmonics* **6**, 527–534 (2011).
11. Lin, L. *et al.* Nanooptics of Plasmonic Nanomatryoshkas: Shrinking the Size of a Core–Shell Junction to Subnanometer. *Nano Lett.* **15**, 6419–6428 (2015).
12. Liu, J. *et al.* Investigation of the optical properties of hollow aluminium

- ‘nano-caps’. *Nanotechnology* **16**, 3023–3028 (2005).
13. Oldenburg, S. J., Jackson, J. B., Westcott, S. L. & Halas, N. J. Infrared extinction properties of gold nanoshells. *Appl. Phys. Lett.* **75**, 2897–2899 (1999).
 14. Liu, J., Maaroo, A. I., Wieczorek, L. & Cortie, M. B. Fabrication of Hollow Metal “Nanocaps” and Their Red-Shifted Optical Absorption Spectra. *Adv. Mater.* **17**, 1276–1281 (2005).
 15. Jain, P. K. & El-Sayed, M. A. Universal Scaling of Plasmon Coupling in Metal Nanostructures: Extension from Particle Pairs to Nanoshells. *Nanolett* **7**, 2854–2858 (2007).
 16. Ye, J., Van Dorpe, P., Van Roy, W., Borghs, G. & Maes, G. Fabrication, Characterization, and Optical Properties of Gold Nanobowl Submonolayer Structures. *Langmuir* **25**, 1822–1827 (2009).
 17. Maaroo, A. I., Cortie, M. B., Harris, N. & Wieczorek, L. Mie and bragg plasmons in subwavelength silver semi-shells. *Small* **4**, 2292–2299 (2008).
 18. Ye, J. *et al.* Fabrication and Optical Properties of Gold Semishells. *J. Phys. Chem. C* **113**, 3110–3115 (2009).
 19. Oldenburg, S. J., Hale, G. D., Jackson, J. B. & Halas, N. J. Light scattering from dipole and quadrupole nanoshell antennas. *Appl. Phys. Lett.* **75**, 1063 (1999).
 20. Ye, J., Lagae, L., Maes, G., Borghs, G. & Van Dorpe, P. Symmetry breaking induced optical properties of gold open shell nanostructures. *Opt. Express* **17**, 23765 (2009).
 21. King, N. S. *et al.* Angle- and Spectral-Dependent Light Scattering from Plasmonic Nanocups. *ACS Nano* **5**, 7254–7262 (2011).
 22. Wollet, L. *et al.* Plasmon hybridization in stacked metallic nanocups. *Opt. Mater. Express* **2**, 1384 (2012).
 23. Cortie, M. & Ford, M. A plasmon-induced current loop in gold semi-shells. *IOP Publ. Nanotechnol. Nanotechnol.* **18**, 235704–6 (2007).
 24. Van Dorpe, P. & Ye, J. Semishells: Versatile Plasmonic Nanoparticles.

- ACS Nano* **5**, 6774–6778 (2011).
25. Knight, M. W. & Halas, N. J. Nanoshells to nanoeggs to nanocups: optical properties of reduced symmetry core-shell nanoparticles beyond the quasistatic limit. *New J. Phys.* **10**, 105006 (2008).
 26. Wang, H. *et al.* Symmetry breaking in individual plasmonic nanoparticles. *Proc. Natl. Acad. Sci. U. S. A.* **103**, 10856–10860 (2006).
 27. Westcott, S. L., Jackson, J. B., Radloff, C. & Halas, N. J. Relative contributions to the plasmon line shape of metal nanoshells. *Phys. Rev. B* **66**, 155431 (2002).
 28. Prodan, E. A Hybridization Model for the Plasmon Response of Complex Nanostructures. *Science (80-.)*. **302**, 419–422 (2003).
 29. Frederiksen, M., Bochenkov, V. E., Cortie, M. B. & Sutherland, D. S. Plasmon hybridization and field confinement in multilayer metal-dielectric nanocups. *J. Phys. Chem. C* **117**, 15782–15789 (2013).
 30. Kuznetsov, A. I., Miroshnichenko, A. E., Fu, Y. H., Zhang, J. & Luk'yanchuk, B. Magnetic light. *Sci. Rep.* **2**, 492 (2012).
 31. Soukoulis, C. M., Kafesaki, M. & Economou, E. N. Negative-Index Materials: New Frontiers in Optics. *Adv. Mater.* **18**, 1941–1952 (2006).
 32. Johnson, P. B., Christy, R. W. & PB Johnson, R. C. Optical Constants of Noble Metal. *Phys. Rev. B* **6**, 4370–4379 (1972).
 33. Palik, E. D. *Handbook of optical constants of solids. Most 1*, (Academic Press, 1985).
 34. Lumerical Inc. | Innovative Photonic Design Tools.
 35. Williams, M. L. CRC Handbook of Chemistry and Physics, 76th edition. *Occup. Environ. Med.* **53**, 504–504 (1996).
 36. Lacharmoise, P. D. *et al.* Imaging optical near fields at metallic nanoscale voids. *Phys. Rev. B* **78**, 125410 (2008).
 37. Cho, J. H. & Gracias, D. H. Self-Assembly of lithographically patterned nanoparticles. *Nano Lett.* **9**, 4049–4052 (2009).

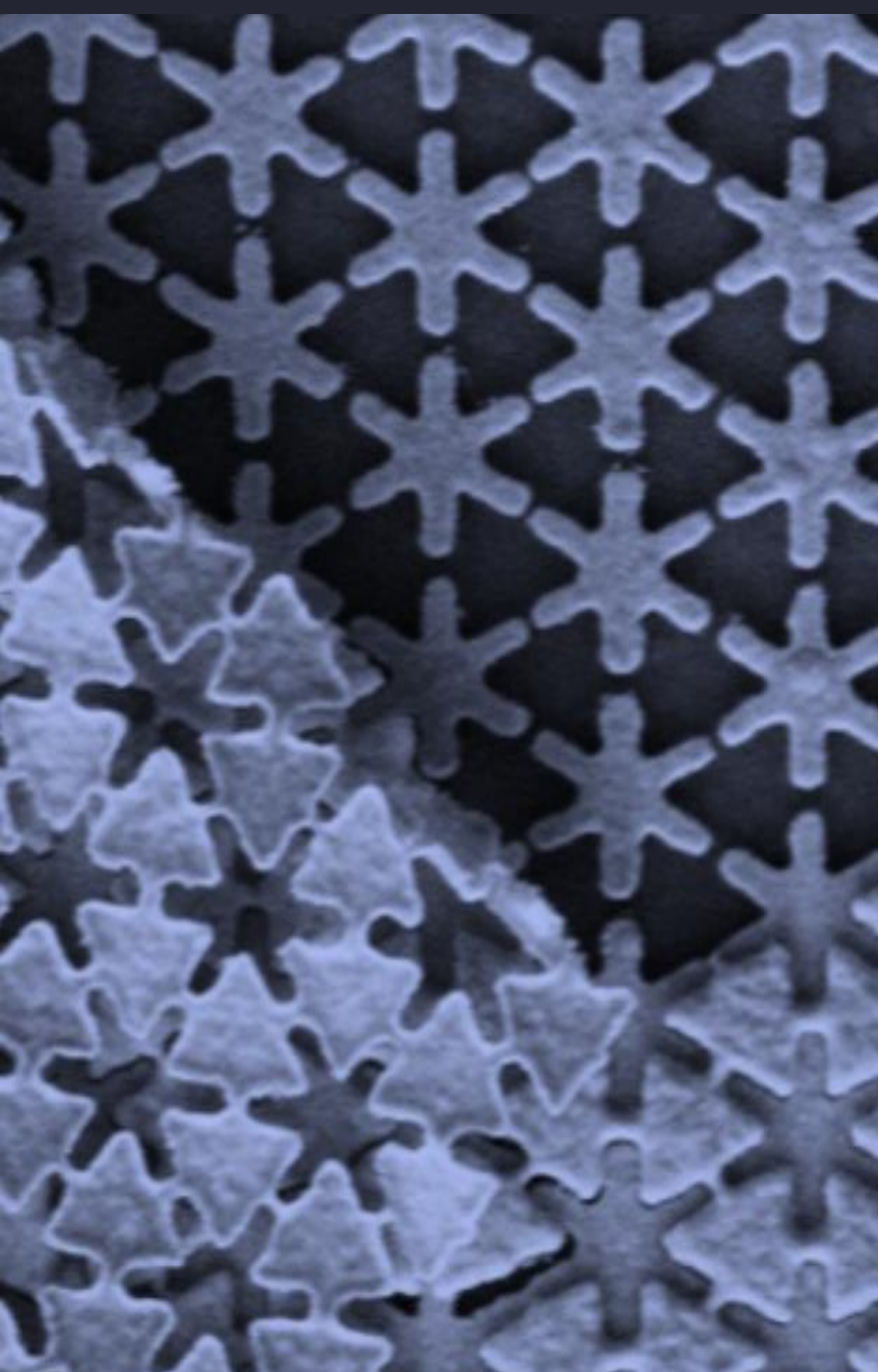
38. Brown, L. V. *et al.* Fan-Shaped Gold Nanoantennas above Reflective Substrates for Surface-Enhanced Infrared Absorption (SEIRA). *Nano Lett.* **15**, 1272–1280 (2015).
39. Knight, M. W., Wu, Y., Lassiter, J. B., Nordlander, P. & Halas, N. J. Substrates Matter: Influence of an Adjacent Dielectric on an Individual Plasmonic Nanoparticle. *Nano Lett.* **9**, 2188–2192 (2009).
40. Bastin, J. A., Mitchell, E. W. J. & Whitehouse, J. Use of an integrating sphere to distinguish between absorption and scattering in solids. *Br. J. Appl. Phys.* **10**, 412–416 (1959).
41. Mashev, L. B., Popov, E. & Loewen, E. G. Brewster effects for deep metallic gratings. *Appl. Opt.* **28**, 2538 (1989).
42. Landy, N. I., Sajuyigbe, S., Mock, J. J., Smith, D. R. & Padilla, W. J. Perfect Metamaterial Absorber. *Phys. Rev. Lett.* **100**, 207402 (2008).
43. Tao, H. *et al.* A metamaterial absorber for the terahertz regime: design, fabrication and characterization. *Opt. Express* **16**, 7181 (2008).
44. Rhee, J. Y., Yoo, Y. J., Kim, K. W., Kim, Y. J. & Lee, Y. P. Metamaterial-based perfect absorbers. *J. Electromagn. Waves Appl.* **28**, 1541–1580 (2014).
45. Tao, H. *et al.* Highly flexible wide angle of incidence terahertz metamaterial absorber: Design, fabrication, and characterization. *Phys. Rev. B* **78**, 241103 (2008).
46. Tittl, A. *et al.* Palladium-Based Plasmonic Perfect Absorber in the Visible Wavelength Range and Its Application to Hydrogen Sensing. *Nano Lett.* **11**, 4366–4369 (2011).
47. Chen, H.-T. Interference theory of metamaterial perfect absorbers. *Opt. Express* **20**, 7165 (2012).
48. Bhattarai, K. *et al.* A Large-Area, Mushroom-Capped Plasmonic Perfect Absorber: Refractive Index Sensing and Fabry-Perot Cavity Mechanism. *Adv. Opt. Mater.* **3**, 1779–1786 (2015).
49. Jiang, Z. H., Yun, S., Toor, F., Werner, D. H. & Mayer, T. S. Conformal Dual-Band Near-Perfectly Absorbing Mid-Infrared Metamaterial Coating.

- ACS Nano* **5**, 4641–4647 (2011).
50. Liu, N., Mesch, M., Weiss, T., Hentschel, M. & Giessen, H. Infrared Perfect Absorber and Its Application As Plasmonic Sensor. *Nano Lett.* **10**, 2342–2348 (2010).
 51. Lin, L. & Zheng, Y. Optimizing plasmonic nanoantennas via coordinated multiple coupling. *Sci. Rep.* **5**, 14788 (2015).
 52. Cai, W., Chettiar, U. K., Kildishev, A. V. & Shalaev, V. M. Optical cloaking with metamaterials. *Nat. Photonics* **1**, 224–227 (2007).
 53. Lu, Y., Liu, G. L., Kim, J., Mejia, Y. X. & Lee, L. P. Nanophotonic crescent moon structures with sharp edge for ultrasensitive biomolecular detection by local electromagnetic field enhancement effect. *Nano Lett.* **5**, 119–24 (2005).
 54. Ye, J. *et al.* Strong location dependent surface enhanced Raman scattering on individual gold semishell and nanobowl particles. *Phys. Chem. Chem. Phys.* **12**, 11222–11224 (2010).
 55. Sterl, F. *et al.* Magnesium as Novel Material for Active Plasmonics in the Visible Wavelength Range. *Nano Lett.* **15**, 7949–7955 (2015).
 56. Liu, G. L., Lu, Y., Kim, J., Doll, J. C. & Lee, L. P. Magnetic nanocrescents as controllable surface-enhanced raman scattering nanoprobe for biomolecular imaging. *Adv. Mater.* **17**, 2683–2688 (2005).
 57. Wang, H., Fu, K., Drezek, R. A. & Halas, N. J. Light scattering from spherical plasmonic nanoantennas: effects of nanoscale roughness. *Appl. Phys. B* **84**, 191–195 (2006).
 58. Tinguely, J.-C. *et al.* Gold Nanoparticles for Plasmonic Biosensing: The Role of Metal Crystallinity and Nanoscale Roughness. *Bionanoscience* **1**, 128–135 (2011).
 59. Bosman, M. *et al.* Encapsulated Annealing: Enhancing the Plasmon Quality Factor in Lithographically–Defined Nanostructures. *Sci. Rep.* **4**, 5537 (2015).



SECTION III

GEOMETRIC FRUSTRATION IN LATTICES OF Au NANOELEMENTS



In this section, the effect of geometric frustration in the optical response of arrays of Au nanoelements is studied.

We present the case of three hexagonal lattices of Au nanoelements fabricated by electron beam lithography and arranged such that the gaps between neighboring elements are small and lead to strong near-field coupling. Besides, far-field interactions yield higher-order collective modes that follow the translational symmetry of the lattice. However, dipolar excitations of the gaps are geometrically frustrated for interactions beyond nearest neighbors, yielding the destabilization of the low energy mode. This in turn results in a slow dynamics of the optical response and a complex interplay between localized and collective modes.

The use of a metal-insulator-metal configuration increases the absorption reaching values above 90% .

All in all, considering the slow dynamics of the system and the occurrence of non-localized enhanced electric fields over large areas, these arrays may be of interest as enhancers for applications related to light absorption.

Chapter 5

Geometric frustration in arrays of plasmonic nanoelements

5.1. Introduction

Frustration has been largely studied in magnetism where the term refers to situations in which one or more spins do not find a proper orientation to fully satisfy all the interactions with the neighboring spins whether by competing interactions or by the geometry of the structure itself.^{1,2} This phenomenon typically occurs, for example, in antiferromagnets with triangle based lattices and short range interactions. As a consequence, the system displays a slow dynamic response induced by the fluctuation between lots of quasi-degenerate configurations.

This chapter aims at introducing and exploiting the concept of geometric frustration in the field of plasmonics. In particular, it is focused on the study of several 2D triangular lattices formed by Au bars, disks, and asterisks, all of them with pitches on the order of the plasmonic resonance frequency.

5.2. Coupling in nanoantennas

It is well known that the response of a plasmonic nanostructure depends on its material, geometry, embedding medium etc.^{3,4} However, when two or more plasmonic nanoelements are close to each other, near- and far-field coupling between them may give rise to responses that are strikingly different.⁴⁻⁸

Near-field coupling takes place in between structures that are just a few nm apart due to the short range EM near-fields (on the order of some tens of nm).^{6,7} In particular, nanoantennas consisting of two close elements, such as bow-tie⁸⁻¹¹ or other dimer structures¹²⁻¹⁶ are an example of in-plane near-field coupled systems. Many systems have been studied, but all of them share a common feature: the fundamental LSPR is shifted or split due to particle interactions (as predicted by the hybridization model¹⁷).⁷ For instance, the near field coupling between two Ag disks excited with a polarization parallel to the dimer axis results in a strong redshift as the gap between the structures is reduced. In fact, at some point, the dipolar approximation starts to underestimate the interaction, which is an indication of the importance of multipolar fields and finite-size effects for small gaps.¹⁴ This implies that a very precise control of the gap in between the structures is needed to tune the response coming from the hybridization of the modes of the two single elements.^{10,16} Moreover, out-of-plane near-field coupling can be achieved as well, for instance, in metal-insulator-metal (MIM) stacks, where the insulator acts as a spacer between both metals and whose thickness can be controlled down to atomic accuracy, in a much easier way than the gap size in coupled dimers.¹⁰ These MIM cavities confine the light in the spacer as SPPs and lead to out-of-plane Fabry-Perot resonances.

Also, far-field coupling can take place in ordered arrays of nanostructures with a pitch on the order of the exciting wavelength induced by the coherent interaction coming from multiple scattering by the ordered elements in the lattice. When the pitch and the LSPR coincide, the optical properties are dramatically modified and sharp diffractive features appear.^{18,19}

5.3. Previous studies of lattices of plasmonic nanoelements

Studies on the geometric dependence of the plasmonic response of arrays of nanoparticles and nanostructures have already been reported by various groups.²⁰⁻²⁴ For instance, Humphrey and Barnes studied Ag disks on glass substrates in different lattices with periods on the order of the LSPR of the particles, finding surface lattice resonances (SLR) for all types of lattices, which depended on the lattice geometry even though the diffraction edge was the same for all of them.²⁰ Guo *et al.* went a step further and analyzed the response of Ag

nanoparticles as a function of the incident angle of the excitation, finding remarkably different extinction dispersions, which were dependent on the polarization of the incoming wave.²¹ Chen *et al.* investigated the response of Au nanodisks in MIM configuration with a thin insulator layer (28 nm), in such a way that LSP and SPP could couple. They found that, while resonances due to the LSP did not change significantly, the SPP modes were certainly affected by the lattice, being the honeycomb lattice the one with the richest absorption characteristics.²² Besides, E. Mariani and G. Weick showed, theoretically, that honeycomb arrays of metallic nanoparticles exhibited unique plasmonic properties that mimicked those of graphene, behaving as massless Dirac plasmons.²⁴ However, to the best of our knowledge, no experimental observations have been carried out in this regard.

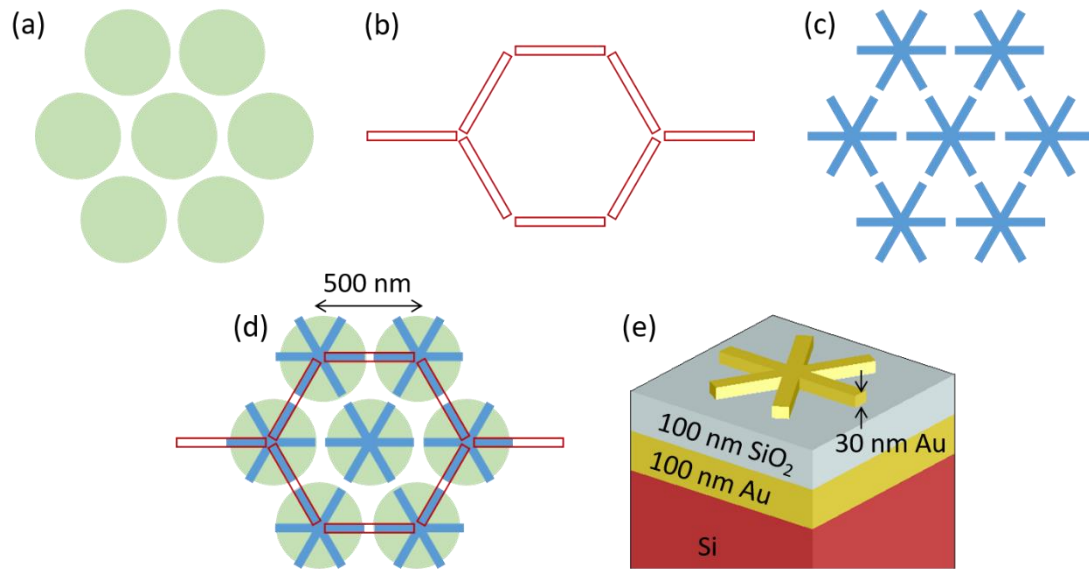


Figure 5.1 (a) Triangular lattice of disks; (b) Honeycomb lattice of bars; (c) Triangular lattice of asterisks; (d) Overlapped lattices to see the comparable sizes of the elements in the three lattices; (e) MIM stack: Si substrate with a 100 nm thick Au and a 100 nm SiO₂ layer and the 30 nm thick nanostructures.

The previously mentioned studies focus on the study of SLR. However, here, we expect to go one step further and benefit from multiple coupling.¹⁰ Figure 5.1(a)-(c) shows the design of the three lattices of Au nanoelements: a triangular lattice of disks (Figure 5.1 (a)), a honeycomb lattice of bars (Figure 5.1 (b)), and a triangular lattice of asterisks formed by three crossing bars (Figure 5.1 (c)). Our structures are arranged in such a way that they strongly

interact via near-field with their nearest neighbors thanks to the small spacing between neighboring elements. For the sake of comparison, instead of optimizing each case, the lattices have been chosen to make their dimensions somehow comparable (see Figure 5.1(d)). Also, we studied structures with MIM configuration where the spacer was set to a quarter-wavelength thickness to achieve maximum absorption for normal incidence thanks to interference as expected from the classical EM wave theory (same approach followed in Section 4.7).¹² Figure 5.1(e) shows the stack over which the array is placed: Si is used as substrate, on top of which 100 nm thick layers of both Au and SiO₂ are placed. All the structures have been designed to be 30 nm thick.

As in the previous chapters, the results presented here have been obtained by using the Finite Difference Time Domain (FDTD) Solutions package from Lumerical.²⁵ Periodic conditions were used in the x - and y -axes, while perfectly-matched layers (PMLs) were used in the z -axis. The source was incident perpendicular to the substrate, following the orientation of the z -axis, with the field oriented parallel to the x -axis. In the simulations, the data from Johnson and Christy²⁶ were used for the permittivity of Au, whereas for SiO₂ and Si, the data from Palik²⁷ were adopted.

5.4. Triangular lattice of disks

To explore the effects of the geometric frustration on the optical response of an ordered array of plasmonic nanoelements, a triangular lattice of disks placed at the vertices of the equilateral triangles forming the array (see Figure 5.2(a)) was studied. This lattice can be also viewed as three offset triangular lattices. Figure 5.2(b) shows the absorption spectra for three cases corresponding to disk diameters (d) of 200 (red), 400 nm (black) and 450 nm (blue), all of them with a thickness (t) of 30 nm of Au and a fixed 500 nm distance between the centers of neighboring disks (pitch, p). In this way, we expect to cover all cases from structures that are coupled through near-field interactions to weakly interacting neighboring elements.

All the spectra show analogue features: low energy broad peaks and sharp high energy peaks collapsed in the visible region of the EM spectrum. The broad peaks in the NIR are strongly dependent on the diameter of the structures,

shifting from ca. 2373 to ca. 1931 and 874 nm when the diameter of the disks is decreased from 450 to 400 and 200 nm, respectively. As a consequence, for the 200 nm case, the peak in the NIR is overlapping one of the sharp peaks in the visible.

The spatial distributions of the electric field in logarithmic scale, $\log(|E|^2/|E_0|^2)$, and charge distributions corresponding to the wavelengths of the peaks of the $d=450$ nm case in Figure 5.2(b), are shown in Figure 5.2(c) and 5.2(d), respectively. The electric field of the NIR peak is concentrated in the horizontal gaps in between disks and is assigned to the dipolar excitation of those gaps, whose corresponding peak is broadened by the effect of damping. This is consistent with the strong shift of the NIR peak observed as a function of the disk diameter and, hence, of the gap between neighboring structures.

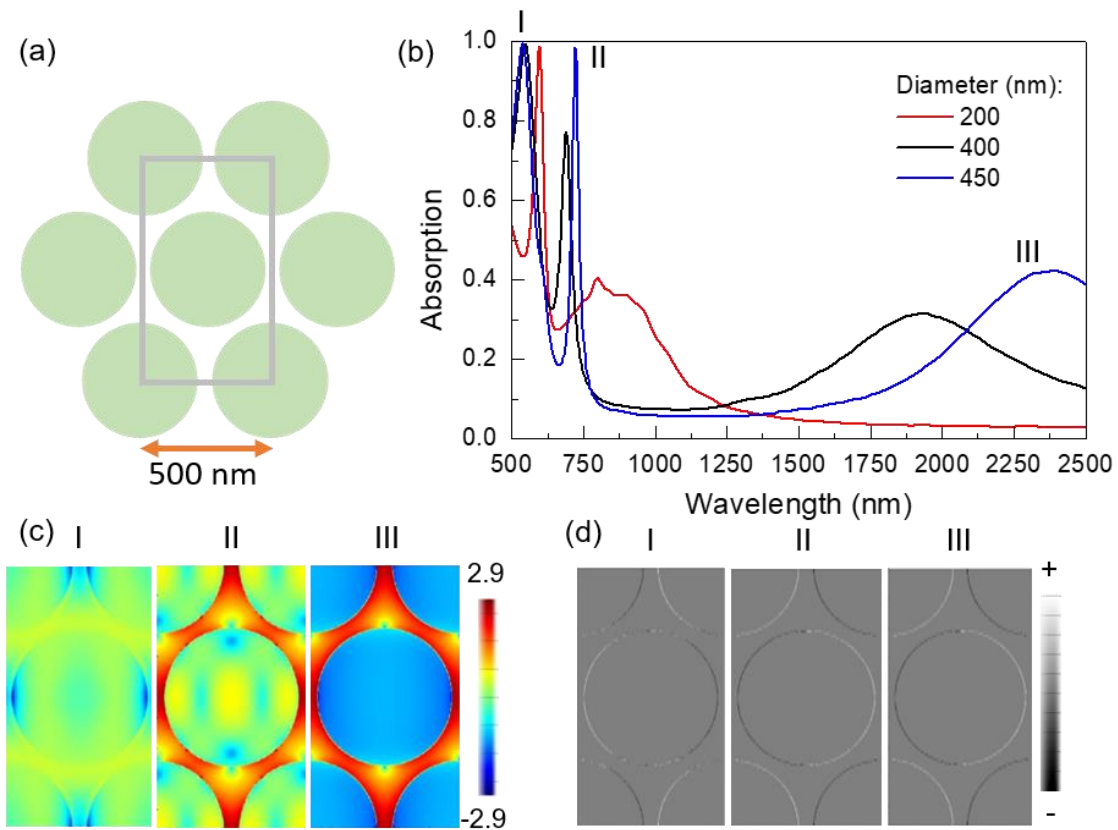


Figure 5.2 (a) Scheme of the triangular lattice of disks, where the grey line shows the simulation area. (b) Absorption spectra of three triangular lattices of disks with $d=200$ nm (red), 400 nm (black), and 450 nm (blue) with $p=500$ nm and a $t=30$ nm. (c) $\log(|E|^2/|E_0|^2)$ and (d) charge distribution for the peaks in (b) for $d=450$, taken at $z=15$ nm, just at half of the thickness of the nanoelements.

On the contrary, for the highest energy mode (labeled as I in Figure 5.2 (b)), the electric field in the horizontal gaps is almost completely suppressed and the maxima are located in the tilted gaps, *i.e.*, gaps at an angle with respect to the electric field of the source. The corresponding sharper and higher energy peaks of the absorption spectrum are much less dependent on the disk diameter and are presumably SLR modes enhanced as a consequence of the cavity formed by the MIM stack. The constructive interference gives rise to high absorption peaks (99.4% at 539 nm, 99.3% at 548 nm, and 98.7% at 598 nm for $d=450$, 400 and 200 nm, respectively). It is worth noting that the $d=450$ nm case shows also almost perfect absorption (98.4%) at 722 nm.

To gain further insight into the effects of the lattice frustration regarding dipolar excitations of the gaps between neighboring nanoelements, we studied the time evolution of the optical response. Such analysis is worthwhile because Kagomé and other 2D triangular lattices exhibiting geometric frustration are well known in magnetism for showing slow relaxation of the magnetization associated with the evolution of the system through a complex energy landscape with a huge number of quasi-degenerate states.²⁸⁻³⁰ This work aims at exploring whether such a slow dynamic response may emerge from the geometric frustration of interacting electric dipoles in plasmonic arrays with triangular symmetry, an approach that, to our knowledge, has not been reported yet.

Figure 5.3(a) shows the time evolution of the magnitude of the electric field in arbitrary units, at two characteristic points of the lattice, depicted in the insets. Remarkably, the system remains active for over 70 fs after an excitation pulse of only about 8 fs long. Furthermore, the time evolution at the two feature points in Figure 5.3(a) follows a slow decaying behavior very similar for both cases, but more intense in the horizontal gaps (parallel to the electric field of the excitation pulse), as one could expect.

In order to shed further light on the response of the system over time, Figure 5.3(b) shows some characteristic snapshots recorded over the time evolution of $\log(|E|^2/|E_0|^2)$ spatial distribution. Under excitation by an incident pulse along the perpendicular direction to the xy plane of the array and with the electric field parallel to the x -axis, the optical response over time follows a complex combination of different modes. The optical response swings between

bonding configurations (panels 1 and 5), where the electric field is enhanced within the gaps along the x -axis, and anti-bonding configurations (panel 3), where the dipolar excitation of the horizontal gaps is suppressed.

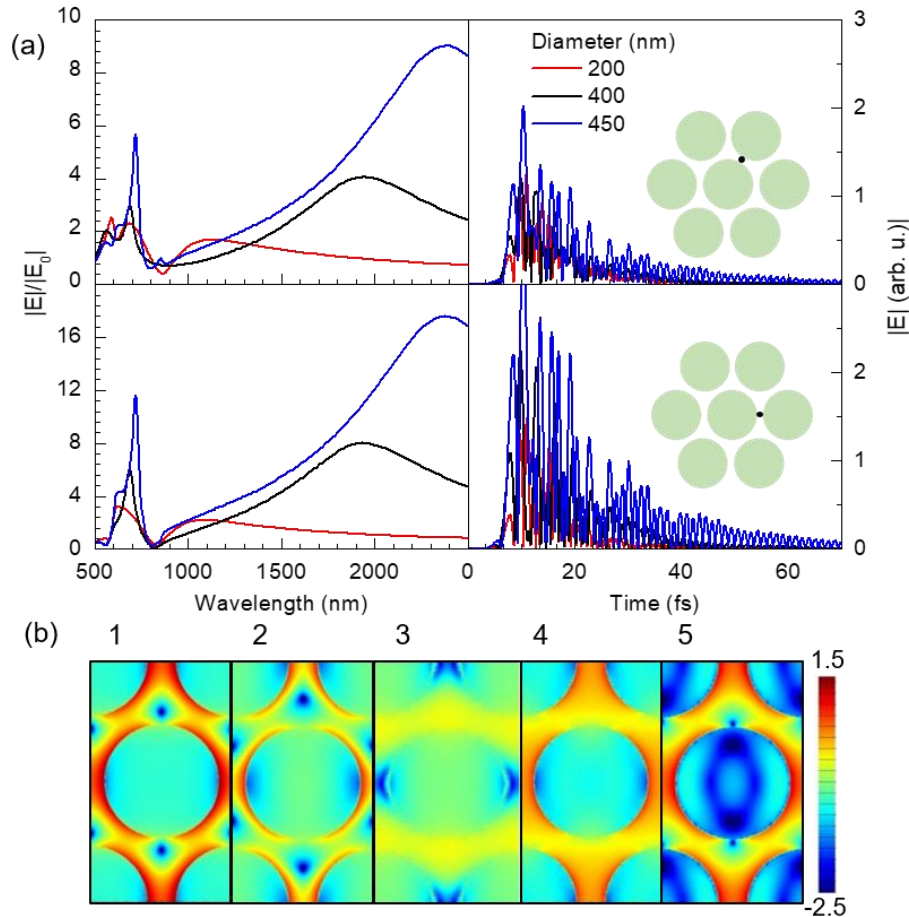


Figure 5.3 (a) Magnitude of the electric field, normalized to the excitation field, E/E_0 , as a function of the wavelength (left) and time evolution of the magnitude of the electric field (right) at the points depicted in the insets. Data correspond to arrays of Au disks of $d=200$ (red), 400 nm (black) and 450 nm (blue), $p=500$ nm and $t=30$ nm. (b) Snapshots of the time evolution of $\log(|E|^2/|E_0|^2)$ for the 400 nm case recorded at a height of $z=15$ nm with respect to the xy plane, being the origin ($z=0$) located at the top of the dielectric layer.

5.5. Honeycomb lattice of bars

Another realization of a plasmonic array with triangular symmetry is a honeycomb lattice consisting in elongated bars placed along the edges of the hexagons at the midpoints of a hexagonal lattice (see Fig. 5.4(a)). This lattice may be, in fact, regarded as two interpenetrated triangular lattices, and,

compared to the previous one, could profit from the lightning rod effect³¹ and give rise to larger areas with enhancement of the electric field. Concomitantly, the gaps between neighboring structures are better defined as compared to the triangular lattice of disks and the near-field coupling between them is more directional and confined.

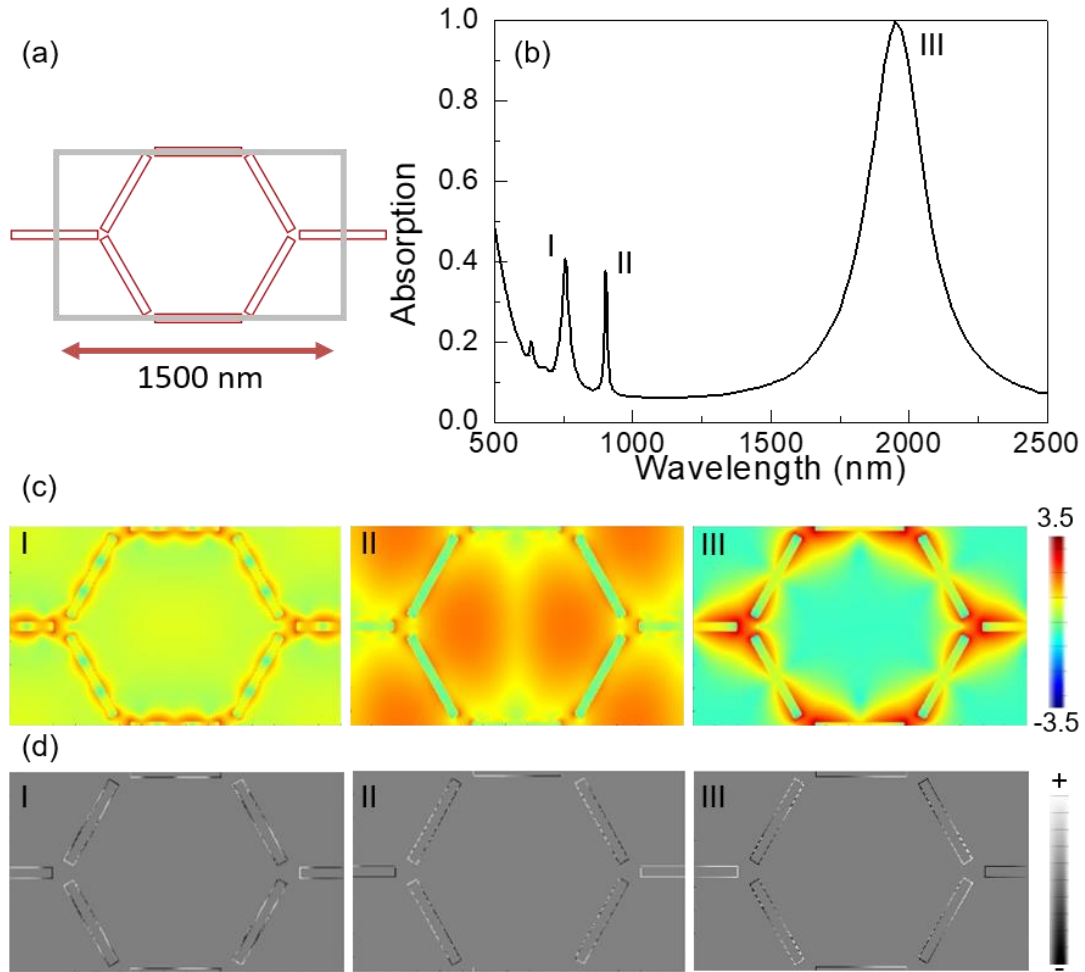


Figure 5.4 (a) Scheme of the honeycomb lattice of bars of 1500 nm/450 nm/45 nm/30 nm ($p/l/w/t$). The grey line shows the simulation region. (b) Absorption spectra of the lattice in (a). (c) $\log(|E|^2/|E_0|^2)$ and (d) charge distribution for the peaks labeled as I-III in (b) at $z=15$ nm, being the origin the top of the dielectric layer.

Figure 5.4 (a) shows a honeycomb lattice of bars of 1500 nm/450 nm/45 nm/30 nm (pitch (p)/length (l)/width (w)/thickness (t)). Unlike the previous case, this system presents a quite sharp peak in the NIR corresponding to a dipolar excitation of the bars, with almost perfect absorption (see Figure 5.4(b)). This peak corresponds to a mode where all the bars show dipolar polarization giving rise to an electric field distribution that is essentially confined in the gaps between bars with a greater intensity than in the case of

disks (see Figure 5.4(c), III). It is worth noting that the geometric frustration of the hexagonal lattice for the dipolar excitation of the bars is clearly evident from the charge distribution of the three bars forming each gap when this low-energy mode is excited: the two tilted bars show a charge accumulation at their ends with opposite sign to that at the end of the horizontal one for every junction (see Figure 5.4(d), III). Interestingly, this is similar to the spin polarization in a magnetic spin-ice lattice.^{32,33}

This is consistent with our assumption that having bars instead of disks may result in a more directional coupling and higher electric field enhancements. Nevertheless, the response in the visible is less intense than that of the disks, showing sharp peaks but poor absorption. The sharper and lower energy peak corresponds to a dipolar excitation along the horizontal bars and a kind of dipolar excitation of the tilted bars in the transverse direction, but modified in the ends due to the constraint of the 3-bars junction. This results in accumulations of charges of the same sign in the two tilted bars and of opposite sign in the horizontal one (see Figure 5.4(d), II). As a result, the electric field map shows big lobes of electric field enhancement surrounding the tilted bars (see Figure 5.4(c), II). The highest energy mode corresponds to an excitation of a mode along the bars of higher order with four maxima of charge. The modes in the visible, showing an enhancement of the electric field far beyond the gaps, are assigned to surface lattices.

Analyzing the time response of the system (see Figure 5.5 (a)), we observe that the evolution of the field intensity in the gaps is pretty similar to that of the disks, with a slow decay of the intensity that extends over 70 fs. The time-lapse frames (see Figure 5.5(b)) show, similarly to the hexagonal lattice of disks, the state of the system changes in a quasi-periodic manner between near-field modes, where the electric field is concentrated in the gaps, and surface lattice resonances, where the electric field is enhanced around the long edges of the bars and almost suppressed in the gaps. Moreover, it is remarkable that, at certain times, a noticeable enhancement of the electric field takes place in the center of the hexagon formed by the bars. Hence, the field as functions of time and wavelength is also studied in this point showing an interesting response (see Figure 5.5 (a), bottom): even though the enhancement is actually low and has

only some importance in the visible, and the decay of the system is faster, the oscillations seem to follow the convolution of two different frequencies.

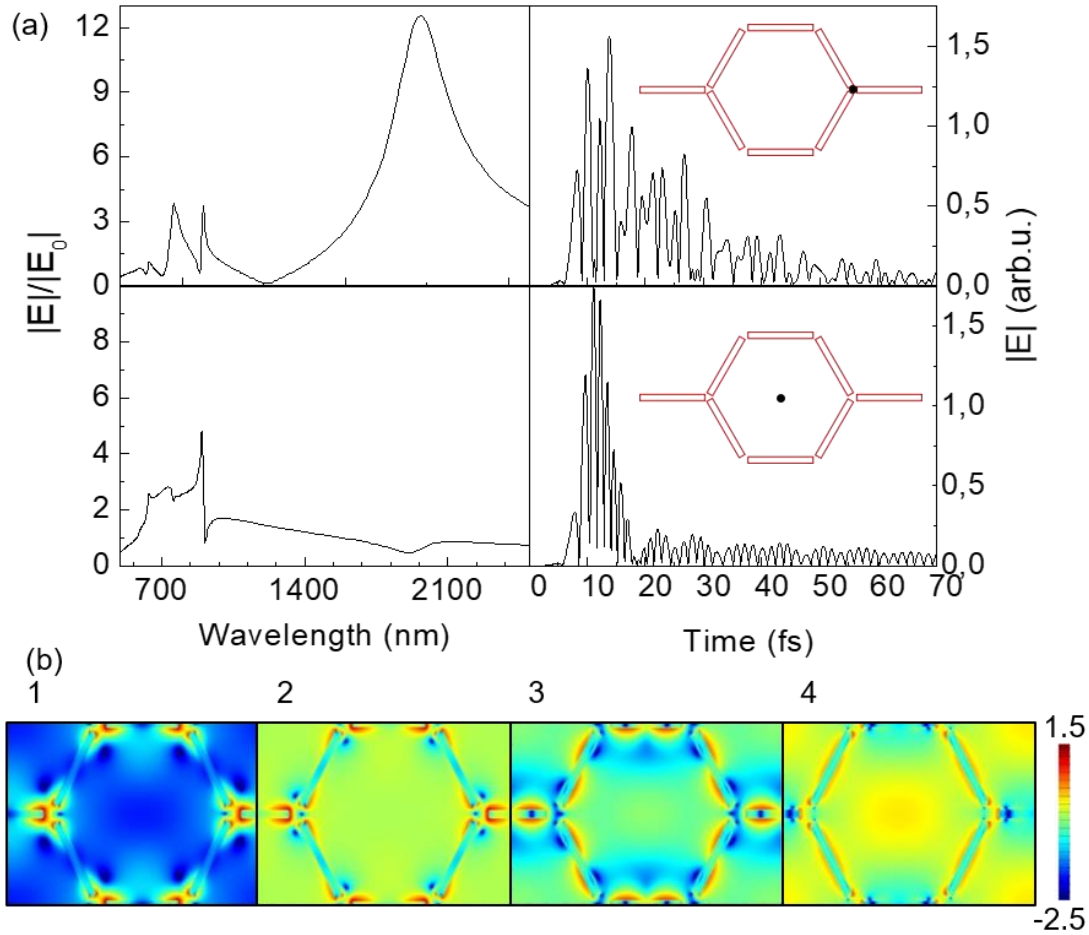


Figure 5.5 (a) Magnitude of the electric field, normalized to the excitation field, E/E_0 , as a function of the wavelength (left) and time evolution of the magnitude of the electric field (right) at the points depicted in the insets. Data correspond to a honeycomb lattice of 1500 nm/450 nm/45 nm/30 nm ($p/l/w/t$). (b) Snapshots of the time evolution of $\log(|E|^2/|E_0|^2)$ recorded at a height of $z=15$ nm with respect to the xy plane, being the origin located at the top of the dielectric layer.

All in all, we have a system which presents almost perfect absorption in the NIR region of the spectrum and high electric field enhancements over a much longer time than the incident pulse, although the response in the visible range of the spectrum is weak. However, this may be improved optimizing the geometric parameters of the elements and the thickness of the dielectric spacer.

5.6. Triangular lattice of asterisks

Trying to unite the benefits of the two previous lattices, a lattice analogue to that shown in Section 5.4 with disks, but composed of asterisks that are formed by three overlapping bars, was analyzed (see Figure 5.6 (a)). In particular, an array of 500 nm/450 nm/45 nm/30 nm ($p/l/w/t$) asterisk-shaped nanostructures is studied. The motivation for this choice is diverse. Firstly, sharper structures will benefit from the lightning-rod effect as in the honeycomb lattice of bars. Secondly, this lattice presents three interpenetrated lattices of gaps (depicted in Figure 5.6(a)), where one of them is oriented parallel to the incident electric field favoring dipolar interactions, while the other two that are not, are expected to result in higher frustration as compared to the previous analyzed lattices. Although the geometric arrangement of the nanoelements is the same than that of the lattice of disks, here the directionality of the gaps is improved. As a consequence, one would expect that the effect of geometric frustration in the array of asterisks to be greater.

The absorption spectrum, displayed in Figure 5.6 (b), exhibits two intense peaks, one wide NIR peak (2277 nm) and a narrow one slightly above the visible region (764 nm), the latter presenting a quality factor of 19 and reaching 98.4% of absorption. Besides, a less intense but also sharp peak is located at 624 nm.

The spatial distributions of both the electric field and charge at the wavelengths of maximum absorbance are shown in Figure 5.6(c) and (d), respectively. For the NIR peak, the electric field namely concentrates in the gaps and at the end edges of the asterisk bars, resulting in localized LSR modes. In contrast, for the VIS peaks, a more spatially extended enhancement of the electric field throughout the array is observed, mostly in areas between the tilted bars of each asterisk, giving rise to more complex, collective SLR modes. This kind of SLR excitation is particularly favored by the coupling with the underlying Au film that creates resonances perpendicular to the MIM structure. As for the charge distributions, the major dipolar character of the NIR peak is evidenced, in contrast to the multipolar charge distribution associated with the high-energy modes.

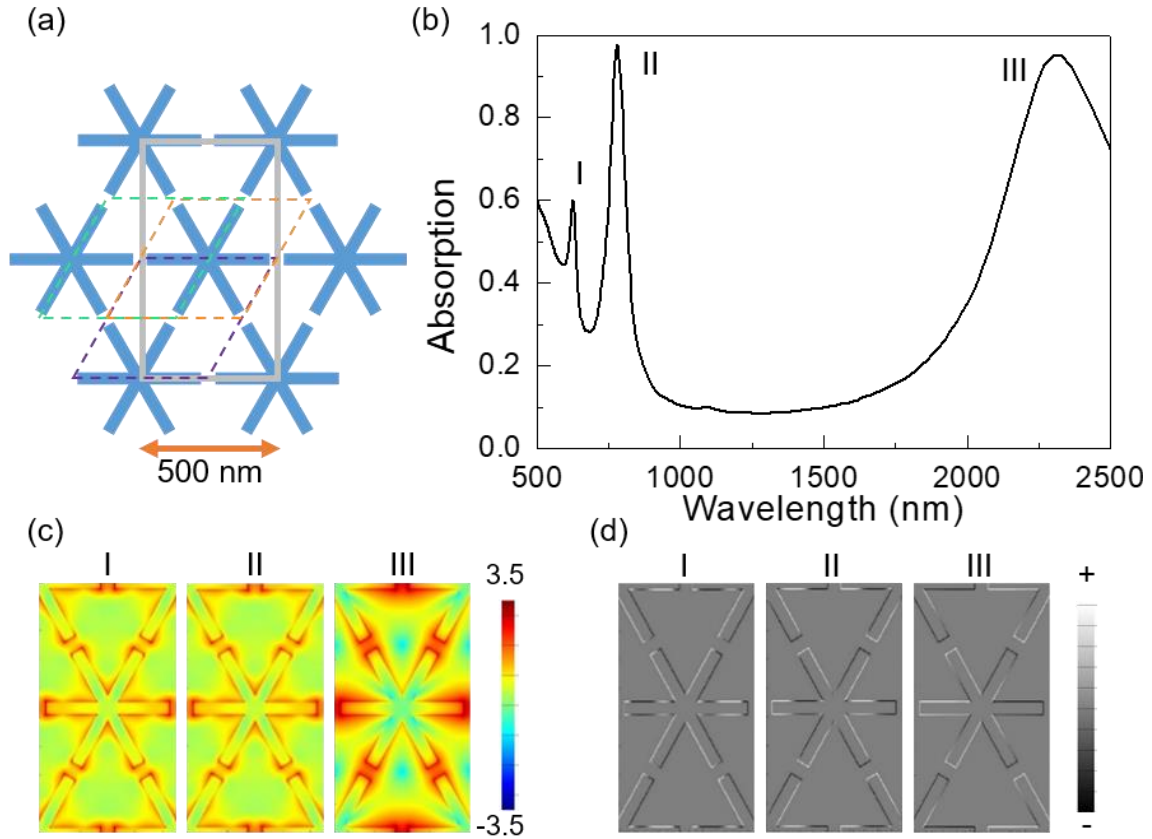


Figure 5.6 (a) Scheme of the hexagonal lattice of asterisks of 500 nm/450 nm/45 nm/30 nm ($p/l/w/t$). The grey rectangle shows the simulation region and the colored dashed lines the three interpenetrated triangular lattices of gaps. (b) Absorption spectra of the array. (c) $\log(|E|^2/|E_0|^2)$ and (d) charge distribution at $z=15$ nm, being the origin located at the top of the dielectric layer, for the peaks labeled as I-III in (b).

The time evolution of the system has been studied by monitoring the evolution in three particular points depicted in the corresponding insets, which are located at characteristic places of the simulated unit cell: the horizontal gaps, the tilted gaps and the V-type shape, formed by the crossing of two bars. The activity of the system extends over 80 fs (Figure 5.7(a), right) showing an oscillating behavior between several configurations, some of which are illustrated in Figure 5.7(b).

Time monitors in the gaps, depicted in the insets in Figure 5.7(a), show the system alternates excitations corresponding to the LSR and SLR modes according to the spectral distributions in Figure 5.6(c). Taking into account that E/E_0 for the low-energy modes is significantly greater than for the high-

energy modes, we can conclude that the higher peaks of the oscillating decay shown in the first row of Figure 5.7(a) are associated with low-energy excitations of dipolar character (LSR modes). In fact, taking the time positions from the higher intensity peaks in the first and second rows of Figure 5.7(a), one retrieves values of the wavelength of 2350 and 2260 nm, respectively, that correspond to the NIR region.

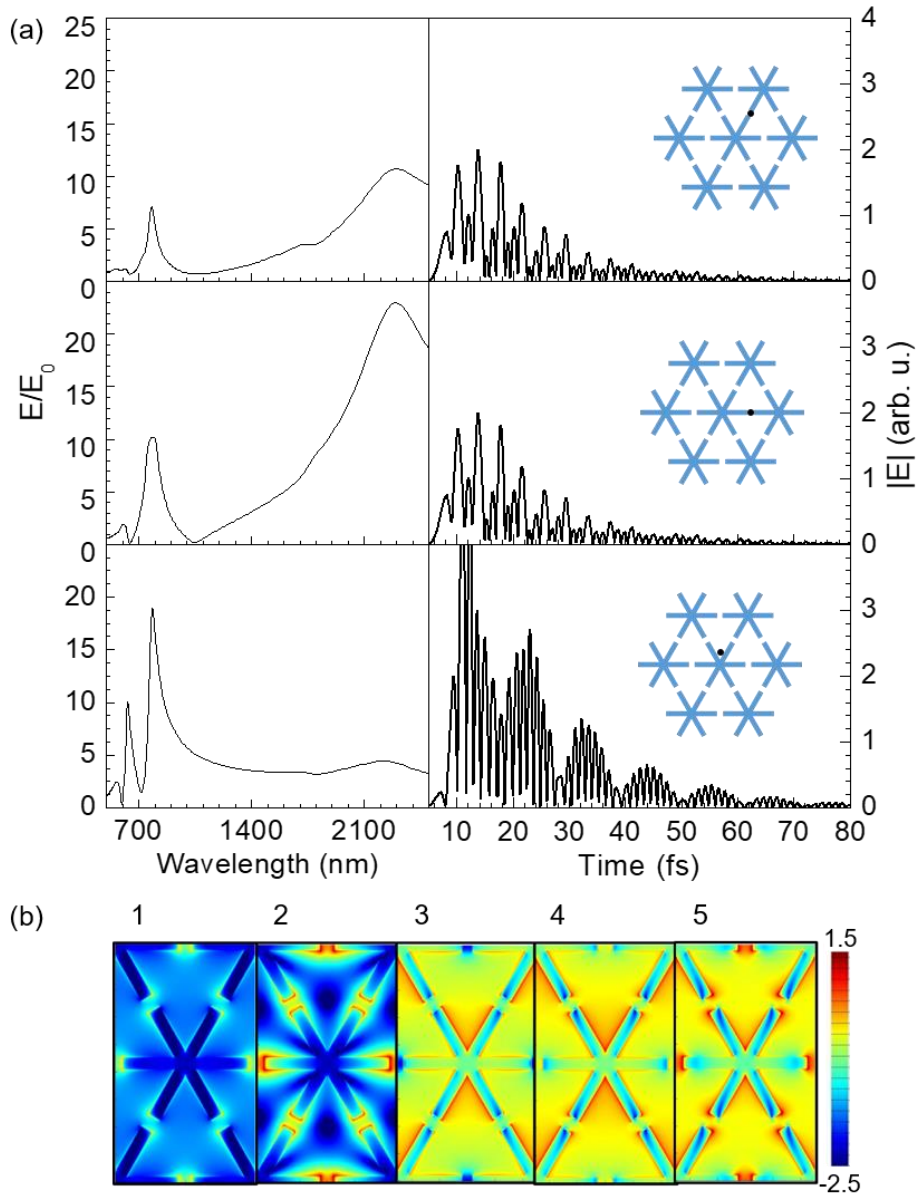


Figure 5.7 (a) Magnitude of the electric field normalized to the excitation field, E/E_0 , as a function of the wavelength (left) and time evolution of the magnitude of the electric field (right), at the points shown in the insets (b) Frames of the time evolution of $\log(|E|^2/|E_0|^2)$ at $z=15$ nm, being the origin located at the top of the dielectric layer.

On the contrary, the time evolution at the V-type shape formed by the arms of the asterisks (last row of Figure 5.7(a)) is simpler, since predominant excitations at this point correspond to high-energy modes (SLR modes). All the peaks of the oscillating decay there are thus related to the excitation of SLR modes, in accordance with the frequency of the observed peaks in the time decay that corresponds to a wavelength of 788 nm.

The foregoing indicates that the extended time response of the array is due to the intricate interplay between local and collective plasmon modes, arising from the geometrical frustration of interacting electric dipoles in lattices with triangular symmetry.

As compared to the previous lattices that presented only one high absorption region (the disks thanks to the SLR in the visible and the bars thanks to the near-field coupling between structures in the NIR), this lattice optimizes both resonances to behave as a dual-band perfect absorber. Also, the excitation follows a slow oscillating decay that results from the convolution of some characteristic frequencies that modulate the swing of the system between the excitation modes over time.

5.7. Conclusions and further work

Along the chapter, the response of three types of lattices of plasmonic nanoelements has been studied, all of which sharing the triangular symmetry, but also having significant differences between them.

The three lattices present an extended time response. The fact that the system resonates for such a long times makes these structures suitable for applications where the absorption and subsequent transfer of the energy of the exciting electromagnetic wave to another system should be maximized such as in enhanced Raman³⁴ and IR spectroscopies³⁵ or in photovoltaic applications.³⁶

Moreover, all of them present, at least, one perfect-absorption peak. While the triangular lattice of disks present two high absorption peaks in the visible and the honeycomb lattice only displays high absorption in the NIR, the array of asterisks achieves almost perfect absorption both in the visible and NIR peaks.

Bars and asterisks formed by bars are easier to polarize resulting in a more confined enhancement of the electric field in the gaps between elements as compared to disks, which have to be very large to achieve near field coupling, at the expense of covering most of the dielectric surface. However, the enhancement of the electric field is not limited to these ‘hot-spots’. In fact, it should be pointed out that the electric field enhancement in these plasmonic arrays extends over much larger areas as compared to strongly coupled dimer antennas, where the hot-spots are limited to the small gap in between the elements.¹⁰ This, together with the fact that they present activity during much longer times than the excitation pulse, makes these types of plasmonic arrays suitable to increase the detection sensitivity limit of biomolecules in enhanced Raman or fluorescence spectroscopies. Even though the maximum field enhancement values (for instance, 528 for the NIR peak and 268 for the VIS peak for the array of asterisks) are lower than those at the hotspots of bowtie antennas,¹⁰ our structures are prone to interact with a significantly larger density of target entities without the need of a precise positioning of the molecules. This would result in both an increase of the spectroscopic signal and a better reproducibility of the results, as compared to nanoantennas with highly confined hotspots which require a complicated positioning of the target molecules that limits the feasibility of those techniques.³⁷

5.8. References

1. Diep, H. T. *Frustrated Spin Systems*. (WORLD SCIENTIFIC, 2005). doi:10.1142/5697
2. Ramirez, A. P. Strongly Geometrically Frustrated Magnets. *Annu. Rev. Mater. Sci.* **24**, 453–480 (1994).
3. Kreibig, U. & Vollmer, M. *Optical Properties of Metal Clusters*. Springer Ser Mater Sci **25**, (1995).
4. Giannini, V., Fernández-Domínguez, A. I., Heck, S. C. & Maier, S. A. Plasmonic Nanoantennas: Fundamentals and Their Use in Controlling the Radiative Properties of Nanoemitters. *Chem. Rev.* **111**, 3888–3912 (2011).
5. Halas, N. J., Lal, S., Chang, W. S., Link, S. & Nordlander, P. Plasmons in strongly coupled metallic nanostructures. *Chemical Reviews* **111**, 3913–3961 (2011).
6. Park, W. Optical interactions in plasmonic nanostructures. *Nano Converg.* **1**, 2 (2014).
7. Ameling, R. & Giessen, H. Microcavity plasmonics: Strong coupling of photonic cavities and plasmons. *Laser and Photonics Reviews* **7**, 141–169 (2013).
8. Ko, K. D. *et al.* Nonlinear Optical Response from Arrays of Au Bowtie Nanoantennas. *Nano Lett.* **11**, 61–65 (2011).
9. Sundaramurthy, A. *et al.* Field enhancement and gap-dependent resonance in a system of two opposing tip-to-tip Au nanotriangles. *Phys. Rev. B - Condens. Matter Mater. Phys.* **72**, 165409 (2005).
10. Lin, L. & Zheng, Y. Optimizing plasmonic nanoantennas via coordinated multiple coupling. *Sci. Rep.* **5**, 14788 (2015).
11. Yan, Z. *et al.* Near-field plasmonic coupling for enhanced nonlinear absorption by femtosecond pulses in bowtie nanoantenna arrays. *Appl. Phys. A* **117**, 1841–1848 (2014).
12. Brown, L. V. *et al.* Fan-Shaped Gold Nanoantennas above Reflective Substrates for Surface-Enhanced Infrared Absorption (SEIRA). *Nano Lett.* **15**, 1272–1280 (2015).
13. Biagioni, P., Huang, J.-S. & Hecht, B. Nanoantennas for visible and infrared radiation. *Reports Prog. Phys.* **75**, 024402 (2012).

14. Gunnarsson, L. *et al.* Confined plasmons in nanofabricated single silver particle pairs: experimental observations of strong interparticle interactions. *J. Phys. Chem. B* **109**, 1079–87 (2005).
15. Humphrey, A. D., Meinzer, N., Starkey, T. A. & Barnes, W. L. Surface Lattice Resonances in Plasmonic Arrays of Asymmetric Disc Dimers. *ACS Photonics* **3**, 634–639 (2016).
16. Huang, J.-S. *et al.* Mode Imaging and Selection in Strongly Coupled Nanoantennas. *Nano Lett.* **10**, 2105–2110 (2010).
17. Prodan, E. A Hybridization Model for the Plasmon Response of Complex Nanostructures. *Science (80-.)*. **302**, 419–422 (2003).
18. Lamprecht, B. *et al.* Metal Nanoparticle Gratings: Influence of Dipolar Particle Interaction on the Plasmon Resonance. *Phys. Rev. Lett.* **84**, 4721–4724 (2000).
19. Auguié, B. & Barnes, W. L. Collective Resonances in Gold Nanoparticle Arrays. *Phys. Rev. Lett.* **101**, 143902 (2008).
20. Humphrey, A. D. & Barnes, W. L. Plasmonic surface lattice resonances on arrays of different lattice symmetry. *Phys. Rev. B* **90**, 075404 (2014).
21. Guo, R., Hakala, T. K. & Törmä, P. Geometry dependence of surface lattice resonances in plasmonic nanoparticle arrays. *Phys. Rev. B* **95**, 155423 (2017).
22. Chen, Y., Dai, J., Yan, M. & Qiu, M. Metal-insulator-metal plasmonic absorbers: influence of lattice. *Opt. Express* **22**, 30807 (2014).
23. Hu, J. *et al.* Surface Plasmon Resonance in Periodic Hexagonal Lattice Arrays of Silver Nanodisks. *J. Nanomater.* **2013**, 1–6 (2013).
24. Weick, G., Woollacott, C., Barnes, W. L., Hess, O. & Mariani, E. Dirac-like Plasmons in Honeycomb Lattices of Metallic Nanoparticles. *Phys. Rev. Lett.* **110**, 106801 (2013).
25. Lumerical Inc. | Innovative Photonic Design Tools.
26. Johnson, P. B., Christy, R. W. & PB Johnson, R. C. Optical Constants of Noble Metal. *Phys. Rev. B* **6**, 4370–4379 (1972).
27. Palik, E. D. *Handbook of optical constants of solids. Most 1*, (Academic Press, 1985).
28. Farhan, A. *et al.* Exploring hyper-cubic energy landscapes in thermally active finite artificial spin-ice systems. *Nat. Phys.* **9**, 375–382 (2013).

29. Morgan, J. P., Stein, A., Langridge, S. & Marrows, C. H. Thermal ground-state ordering and elementary excitations in artificial magnetic square ice. *Nat. Phys.* **7**, 75–79 (2011).
30. Farhan, A. *et al.* Direct Observation of Thermal Relaxation in Artificial Spin Ice. *Phys. Rev. Lett.* **111**, 057204 (2013).
31. Urbieto, M. *et al.* Atomic-Scale Lightning Rod Effect in Plasmonic Picocavities: A Classical View to a Quantum Effect. *ACS Nano* **12**, 585–595 (2018).
32. Giblin, S. R., Bramwell, S. T., Holdsworth, P. C. W., Prabhakaran, D. & Terry, I. Creation and measurement of long-lived magnetic monopole currents in spin ice. *Nat. Phys.* **7**, 252–258 (2011).
33. Drisko, J., Marsh, T. & Cumings, J. Topological frustration of artificial spin ice. *Nat. Commun.* **8**, 14009 (2017).
34. Du, L., Zhang, X., Mei, T. & Yuan, X. Localized surface plasmons, surface plasmon polaritons, and their coupling in 2D metallic array for SERS. *Opt. Express* **18**, 1959 (2010).
35. Neubrech, F., Huck, C., Weber, K., Pucci, A. & Giessen, H. Surface-Enhanced Infrared Spectroscopy Using Resonant Nanoantennas. *Chem. Rev.* **117**, 5110–5145 (2017).
36. Atwater, H. A. & Polman, A. Plasmonics for improved photovoltaic devices. *Nat. Mater.* **9**, 205–213 (2010).
37. Rakovich, A., Albella, P. & Maier, S. A. Plasmonic Control of Radiative Properties of Semiconductor Quantum Dots Coupled to Plasmonic Ring Cavities. *ACS Nano* **9**, 2648–2658 (2015).

Chapter 6

Arrays of plasmonic nanoelements: experimental results

6.1. Introduction

Along this chapter, the experimental results regarding the plasmonic arrays of nanoelements discussed in Chapter 5 are gathered.

EBL has been used to fabricate the samples to monitor the relationship between the geometry and the optical response of the nanostructures: by varying the design and lithography parameters, different sizes and shapes have been produced and later characterized using FTIR spectroscopy, showing the tunability of the plasmonic response as a function of the geometry. Moreover, it is also shown that the proper engineering of the optical properties enables the use of these structures as substrates for SERS.

Special emphasis has been devoted to the nanoasterisks lattice since, as shown in the previous chapter, it is the one presenting the most interesting properties. Hence, for this case, simulation results regarding the optical response as a function of each and every relevant geometric parameter have also been enclosed.

6.2. Triangular lattice of asterisks

As in previous cases, in the simulations presented along this chapter the incident field is normal to the substrate, with the electric field parallel to the x -axis. A TFSF source is used for single elements and plane wave illumination is used for simulations of the whole array. For the former, PML boundary conditions are used in the three axes, while for the later periodic conditions are used in the x - and y -axes and PMLs for the z -axis. When possible, symmetric and anti-symmetric conditions are used to further reduce the calculation area to a quarter of unit cell. The permittivities are directly taken from the data base of Lumerical: Johnson and Christy's¹ data for Au, Palik's² for Cr, Si and SiO₂ and CRC³ for Ti.

6.2.1. Plasmonic response of a single nanoasterisk

Before going into the analysis of the lattice, a single element, *i.e.*, an asterisk formed by the intersection of three bars is studied. From now on, the geometry of the asterisks will be denoted as (pitch (p)/length (l)/width (w)/thickness (t)), in nm, for the sake of simplicity. The simulation area was 1500 nm x 1500 nm x 500 nm with a mesh of 5 nm covering the structure.

Extinction, scattering and absorption as a function of length, width and thickness

Figure 6.1 shows the effect of geometry in the extinction, scattering and absorption of a single asterisk without substrate. In each row, the y -scale is kept constant for better comparison between the contributions of absorption and scattering to the extinction.

In the first row, plots (a)-(c), the length varies from 100 to 600 nm while keeping width and thickness constant (45 and 30 nm, respectively). The extinction shows two peaks, one in the visible range and a more intense one in the NIR, that shift to longer wavelengths for increasing length, except for the 100 nm case in which both peaks are too close to be distinguishable. Besides, a small peak appears to the right of the peak located in the visible, while a

shoulder emerges to the left of the NIR peak, being more prominent for smaller lengths. Looking at the scattering and absorption plots, one can see that the peak in the visible is mostly due to absorption while the NIR peak has contribution from both scattering and absorption.

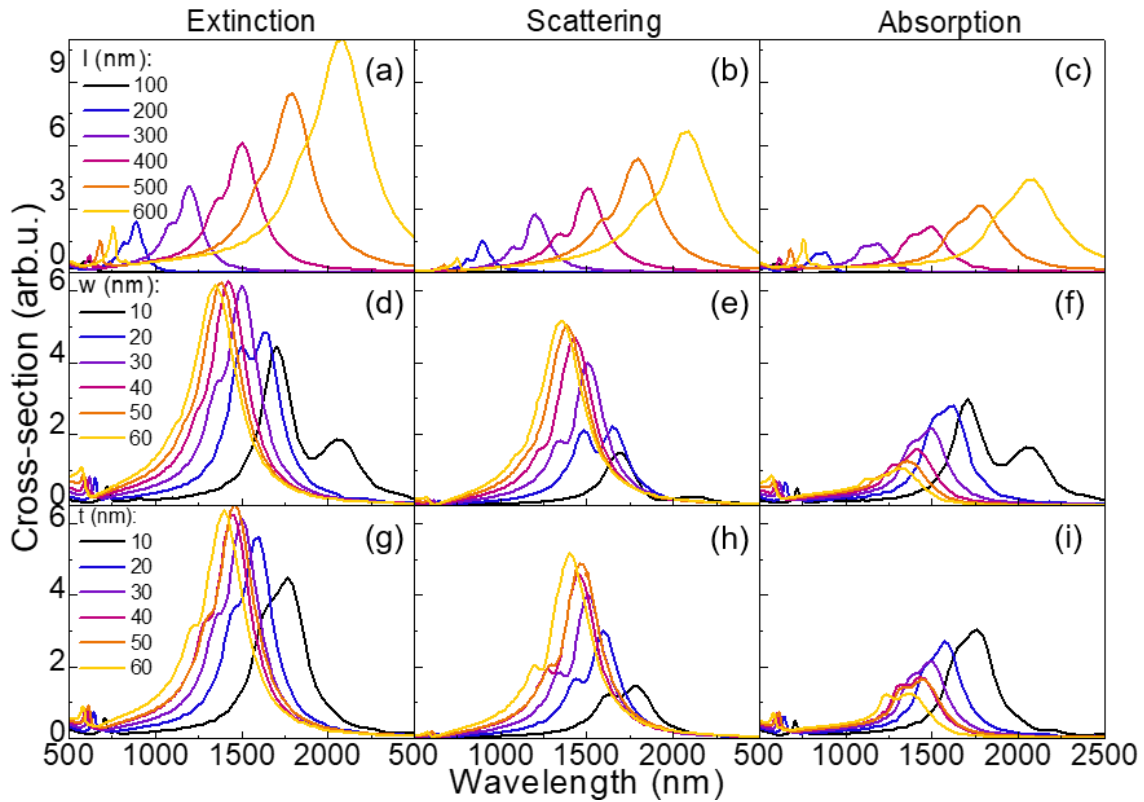


Figure 6.1 Extinction ((a), (d) and (g)), scattering ((b), (e) and (h)), and absorption ((c), (f) and (i)) cross-sections of a single asterisk without substrate: (1) for constant $w=45$ nm and $t=30$ nm, changing length ((a)-(c)); (2) for constant $l=450$ nm and $t=30$ nm, changing width ((d)-(f)); and (3) when thickness is varied from 10 to 60 nm while keeping $w=45$ nm and $l=450$ nm constant ((g)-(i))

When the width is changed for $l=450$ nm and $t=30$ nm (case shown in the second row, in panels (d)-(f)), a small peak appears in the visible arising from the absorption that shows a blueshift for increasing width. However, the main response lies on the NIR part of the spectrum, with a peak that redshifts with decreasing width. Besides, one can see that as the width is reduced, the peak in the NIR splits into two different peaks, starting as a smooth shoulder to the left of the peak for the case of 60 nm to two well differentiated peaks, the higher energy being more intense, for the case of 10 nm. Panels (e) and (f) show that there are contributions from both absorption and scattering to these two peaks.

Finally, in the third row, $l=450$ nm and $w=45$ nm are kept constant, while the t is changed from 10 to 60 nm. Again, there is a peak in the visible range, coming from the absorption of the structures that shows a blueshift for increasing thickness. The main response is, once again, in the NIR region, where a main peak with a shoulder to its left appears, blueshifting for increasing thickness.

6.2.2. Plasmonic response of a lattice of asterisks

Figure 6.2 shows the absorption, reflection and transmission of arrays of nanoasterisks of different geometry without substrate. The system presents, for all cases, two well-defined peaks: a sharper peak in the visible and a broader one in the NIR. By tuning the gap, length and pitch of the system, a clear evolution is observed.

Constant gap

Figure 6.2 shows that, keeping the gap constant to 50 nm and increasing the pitch of the array and hence the length of each asterisk, both peaks are redshifted, being this shifting more noticeable in the lower energy peak. Also, with increasing size, the absorption is slightly increased. For the NIR peak, this increase is due to a decrease in the reflection, while for the visible peak, it is more related to an increase in the transmission for increasing pitch/length.

Constant length

If the length is kept constant, and the pitch is increased to enlarge the gap, a blueshift is observed in Figure 6.2(d)-(f). It is worth noting that, while for a change from 460/20 to 480/30 (pitch/gap) the shift is very notable, for a further to 480/50, the shift is barely noticeable.

Constant pitch

Keeping the pitch constant and increasing the length (Figure 6.2(g)-(i)), with a concomitant decrease in the gap size, results in shifts of the peaks to lower energies.

When the pitch is kept constant (Figure 6.2(g)-(i)) or when it is only slightly shifted (Figure 6.2(d)-(f)), the shift in the visible peak is barely changed as compared to the lower energy peak. This could make one think that the higher energy peak could be more related to the lattice itself while the lower energy one could be more related to the individual elements, in accordance with the results shown in the previous chapter.

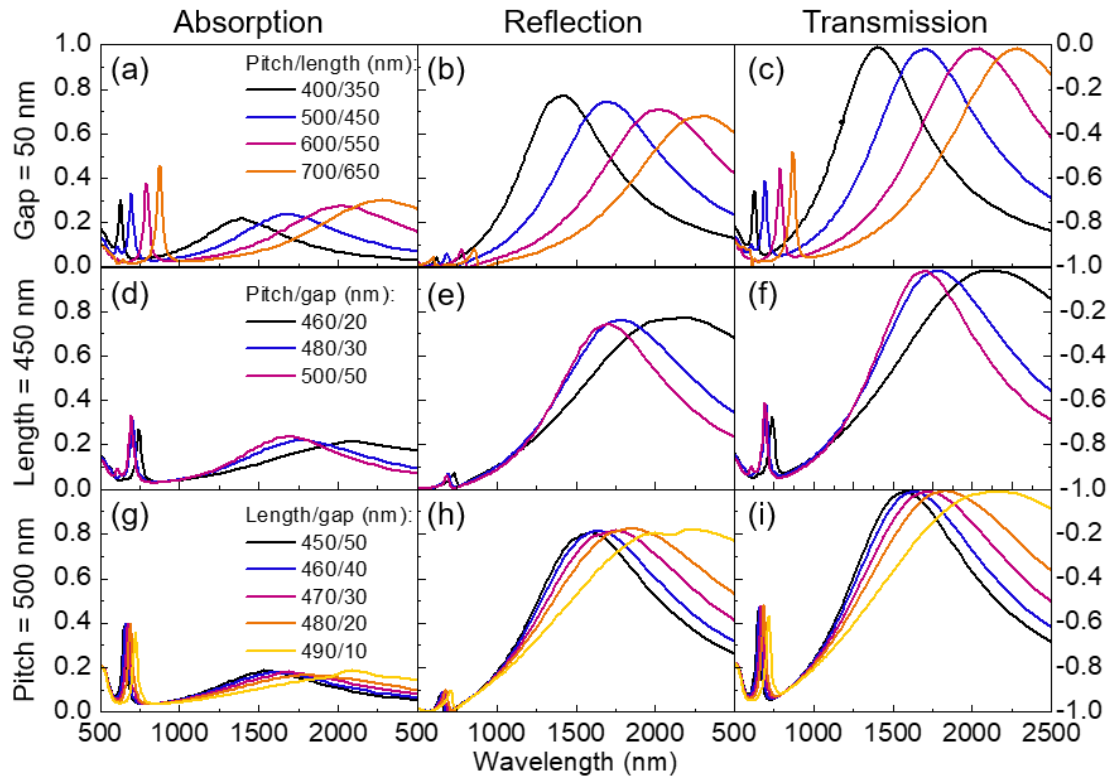


Figure 6.2 Absorption (a), (d), (g), reflection (b), (e), (h), and transmission (c), (f), (i) for arrays of nanoasterisks with constant gap (a)-(c), length (d)-(f), and pitch (g)-(i) with no substrate.

MIM configuration

To enhance the absorption of light, a MIM configuration has been implemented following the same optimization described in Chapter 4. The absorption for a 500/450/45/30 nm array of asterisks ($p/l/w/t$), with SiO₂ substrate (dashed black line) and for a stack of Si + Au + SiO₂ (MIM) of different thicknesses (solid lines) is displayed in Figure 6.3. As compared to the SiO₂ substrate, presenting a 29 and 17 % absorption in the visible and NIR

peaks, respectively, the simulations performed with MIM configuration can be optimized to reach over 99% of light absorption for both peaks. Besides, the latter configuration leads to a sharpened NIR peak. Since we were aiming to optimize the absorption in the visible, the samples were fabricated with a 100 nm-thick SiO_2 layer which presents the highest value in the visible and still 90% absorption in the NIR peak.

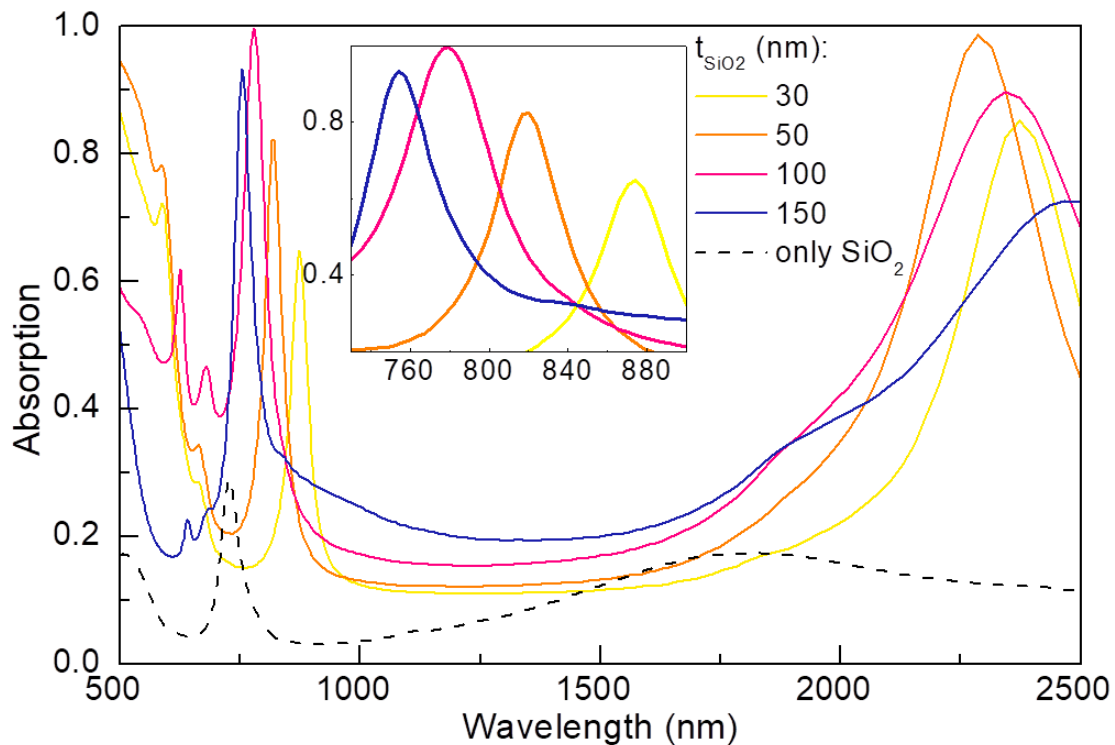


Figure 6.3 Absorption measured in reflection as a function of wavelength for an array of asterisks of 500 nm/450 nm/45 nm/30 nm, and different SiO_2 thickness, without adhesion layer. Inset: detail of spectra in the 740 nm- 900 nm region.

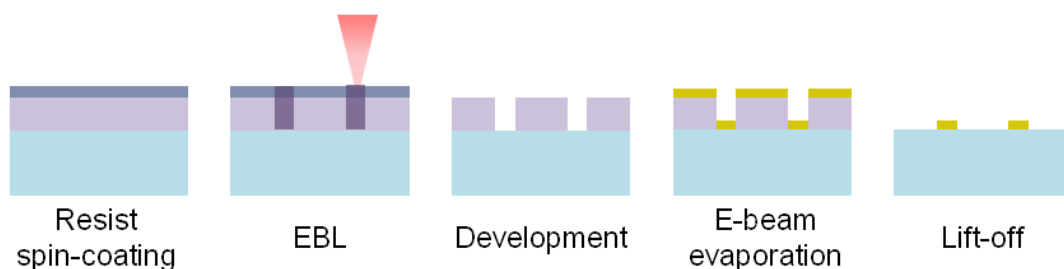
6.2.3. Fabrication of the samples

All samples were fabricated by EBL with the Raith 150 Two available at the Clean Room of the IMB-CNM. EBL was chosen to do fast prototyping to study effects of different geometries in the plasmonic response.

Samples were fabricated onto glass substrates and using a MIM configuration, following the scheme illustrated in Figure 6.4. Glass substrates were cleaned using acetone in ultrasounds for 5 minutes, IPA in ultrasounds for

5 minutes and oxygen plasma at 500 W for 5 minutes. For the case of the MIM configuration, a wafer was cleaned following the same procedure as for the glass substrates and the whole wafer was metallized by thermal evaporation, using 5 nm of Ti as adhesion promoter for the 60 nm thick Au layer. Then, the wafer was cleaved into pieces of 1.5 x 1.5 cm² approximately and those pieces were processed separately.

(a) Samples on glass substrates:



(b) Samples with MIM configuration:

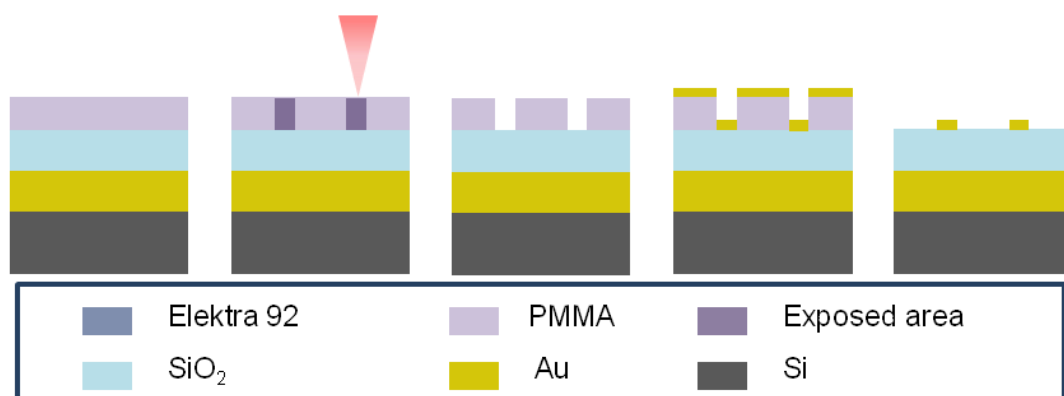


Figure 6.4 Fabrication scheme for samples fabricated onto glass substrate (a) and in MIM configuration (b).

According to the simulation results, a layer of 100 nm of SiO₂ as spacer for the MIM configuration was the optimum value to achieve maximum absorbance in the visible. Accordingly, the OXFORD PLASMALAB 800 Plus PECVD was used to deposit the oxide in two steps: first, a thin layer was deposited at 50 W of RF power and 350°C for 20 seconds, which corresponds to around 20 nm. This layer, which comprises typically 10-20% of the total oxide thickness, protects the underlying Au layer. Then, the power was increased to 200 W and the temperature to 380°C to deposit the remaining thickness. The time of the second step was adjusted according to the desired thickness taking into account

that from 50 nm on, the deposition rate is constant. In particular, to deposit 80 nm in the second stage, having a total of 100 nm of SiO₂, the time was adjusted to 71 s. The roughness of SiO₂ and Au were measured with AFM showing values under 1 nm (not shown).

The resist used for all the samples was PMMA A2 (Microchem) with a variable thickness (spinning speed changed from 1500 to 1000 rpm). For glass substrates, a conductive resist (Elektra 92, AR-PC-5090, All Resist) was used to avoid problems with beam deflection due to charge build-up during the EBL exposure. This resist was spin coated at 4000 rpm for 1 minute and cured for 2 minutes at 90°.

The electron beam exposure was done at 20 kV with a 20 µm gun aperture and a step size of 10 nm. The dose was fixed to 180 µA/cm² and the dose factor (DF) was changed from area to area to finely tune the size of the obtained nanoelements.

After the exposure, the sample was developed by dipping it in a 1:3 solution of methyl isobutyl ketone (MIBK) in IPA for 30 seconds and rinsed for 30 seconds in IPA to stop the reaction. For samples containing the conductive resist, prior to the development, the conductive layer was removed by dipping the sample in deionized water for 1 minute.

The metallization was performed in the ATC Orion (AJA International, Inc) electron beam evaporator at the Institut Català de Nanociència i Nanotecnologia (ICN2). For all the samples, thin (0.5-2 nm) layers of Ti or Cr were used to promote adhesion before depositing the Au layer (20-30 nm).

Finally, the sample was immersed in acetone at 40°C for 5 minutes to soften the resist and then ultrasounds were applied to perform the lift-off. However, to favor lift-off, an undercut or inverted profile is required and a minimum ratio of about 1:3 for the metal:resist thickness is desired. Hence, this is one of the main challenges of the fabrication process: we are dealing with linewidths on the order of 20 nm in some cases, separated by gaps on the same order. The design of these structures results in an almost closed triangle of remaining resist opened

only by three small gaps, with the additional difficulty of having a minimized thickness of PMMA to improve resolution.⁴

Figure 6.5 shows some of the features obtained where the tunability of the fabrication method to obtain structures going from asterisk- (upper left) to star-shaped (bottom right) nanostructures is clearly proved. This wide range in the shape of the nanoelements is obtained by changing the design, but also by changing the DF during the EBL: the higher the DF, the more star-like structures.

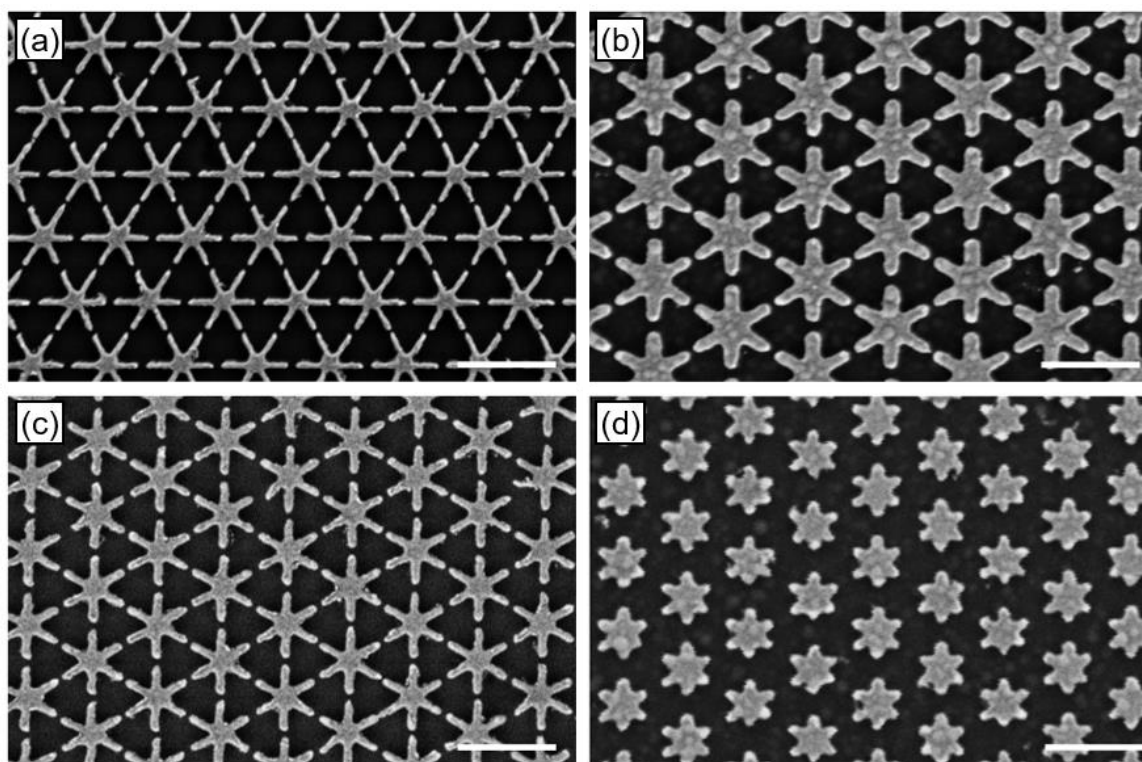


Figure 6.5 Representative SEM micrographs corresponding to different samples, from asterisk- (a) to star-shaped (d) nanostructures, obtained by changing the fabrication parameters. The scale bars correspond to 500 nm.

As explained before, one of the main challenges in the fabrication is the lift-off process: to fabricate high resolution samples with gaps and widths below 20-30 nm, the resist should be as thin as possible to minimize the deflection of the electrons along the resist layer and the backscattered electrons. However, the

thinner the resist, the more difficult to have a successful lift-off: as the gaps are small and the resist layer is thin, the available area of resist for the acetone to actuate is very small.

6.2.4. FTIR characterization

The plasmonic response of the fabricated samples was characterized using FTIR spectroscopy at ICMAB. In accordance with the FDTD simulations, Figure 6.6 shows, for a constant pitch, a redshift in the low energy peak for increasing length. Besides, one can finely tune this peak by just changing the dose factor during the EBL exposure.

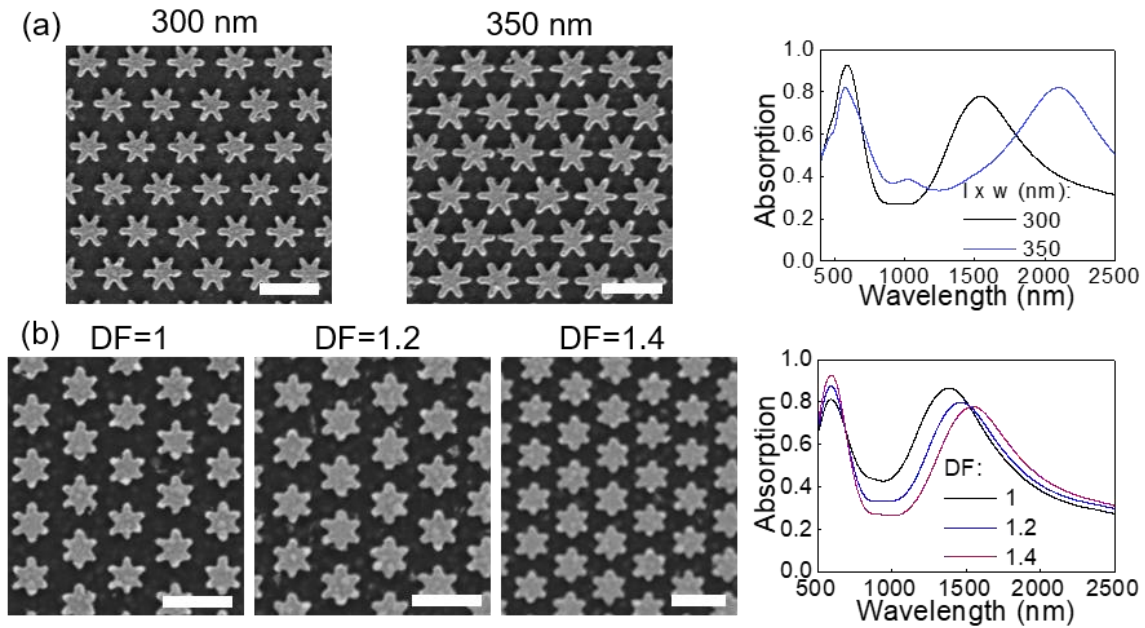


Figure 6.6 SEM micrographs (left) and their corresponding FTIR spectra (right) for samples with a pitch of 400 nm designed to have a width of 30 nm and metallized with 0.5 nm of Cr and 20 nm of Au, for different lengths (a) and for a length of 300 nm with different dose factors during the EBL (b). The scale bars correspond to 500 nm.

Figure 6.6 shows a reasonable agreement with the simulations shown in the previous chapter, FTIR results displaying the same features as the simulations, *i.e.* two high absorption peaks located in the visible and NIR, respectively. In further agreement with the simulation results, the low energy peak is easily

shifted with changes in the geometry of the single elements, while the higher energy peak is less movable. However, this latter peak broadens as compared to the one in the simulations, which makes it difficult to determine whether there is any actual shift with changes in the geometry.

6.2.5. Differences between simulations and experimental results: approximation to the real sample

In this section, the physical origin of the differences between experimental and simulation results are addressed.

First, the shape obtained after the EBL fabrication is far from being the perfect designed asterisk, which is in fact what is simulated. Secondly, AFM profiles (see Figure 6.7) show that the structures are thicker in their ends. To account for the actual geometry of the nanoelements, Figure 6.8 shows the simulated absorption of modified geometries according to the real samples for an array of asterisks of 500 nm/450 nm/30 nm/0.5 nm Cr + 30 nm Au. To begin with, corners of the EBL-fabricated structures tend to be rounded. To account for this, a cylinder with a diameter equal to the width of the bar was added to the end of the bars forming the asterisks, whose length was reduced by a length equal to the radius of the cylinder, keeping constant the width of the gap (see Figure 6.8(a)). Besides, the nanoelements are not purely rectangular bars overlapped like those shown in the FDTD design, but they rather have a bigger center as compared to the end of the bars. This is due to an overexposure of the center as compared to the ends of the bars. To compensate for this, a central cylinder of 200 nm was added at the center of the asterisk (see Figure 6.8(b)). When adding that central cylinder, the intersection between two bars makes a rounded outwards form, while in the fabricated samples this rounded shape is inwards. To account for that inwards shape in the simulations, a cylinder etch of 66 nm in diameter was added (Figure 6.8 (c)). Finally, taking into account the AFM profiles in Figure 6.7, semi-spheres were added at the ends of the stars.

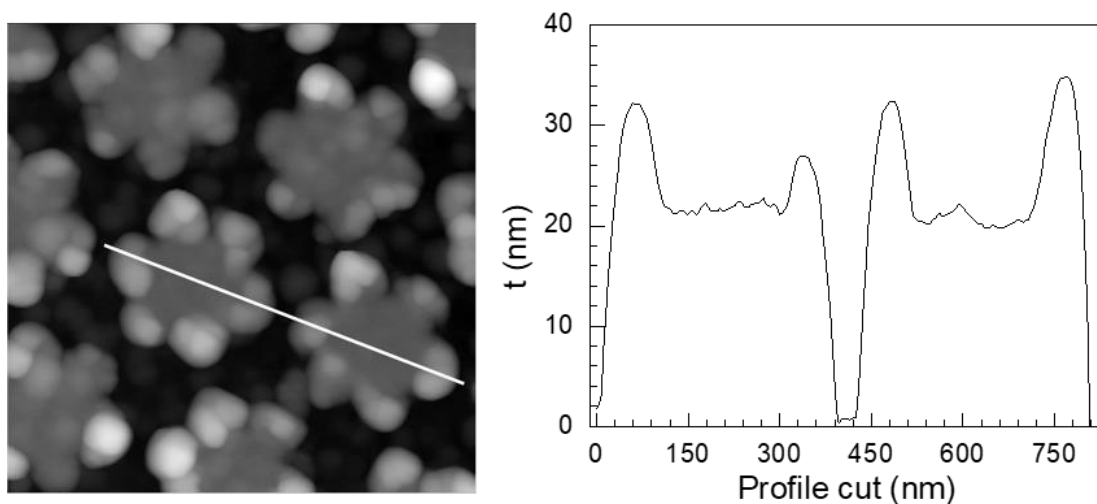


Figure 6.7. AFM image (left) and profile (right) of the line in the image of an array of asterisk-shaped nanostructures.

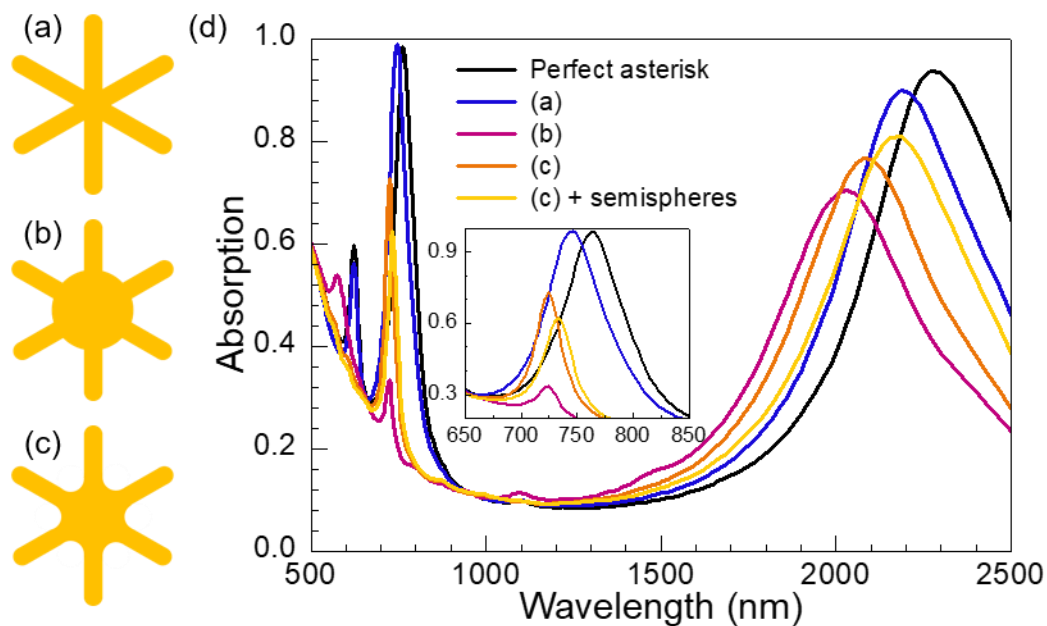


Figure 6.8 Effect of shape correction in the absorption spectrum. (a)-(c) Schemes of the simulated samples with different corrections of the shape: (a) asterisk with the rounded shape correction of the bars' ends. (b) correction in (a), plus an added 200 nm in diameter central cylinder to account for overexposure in the central part. (c) corrections in (b) plus inwards rounded junctions between bars and the central cylinder. (d) Absorption spectra for the different corrections.

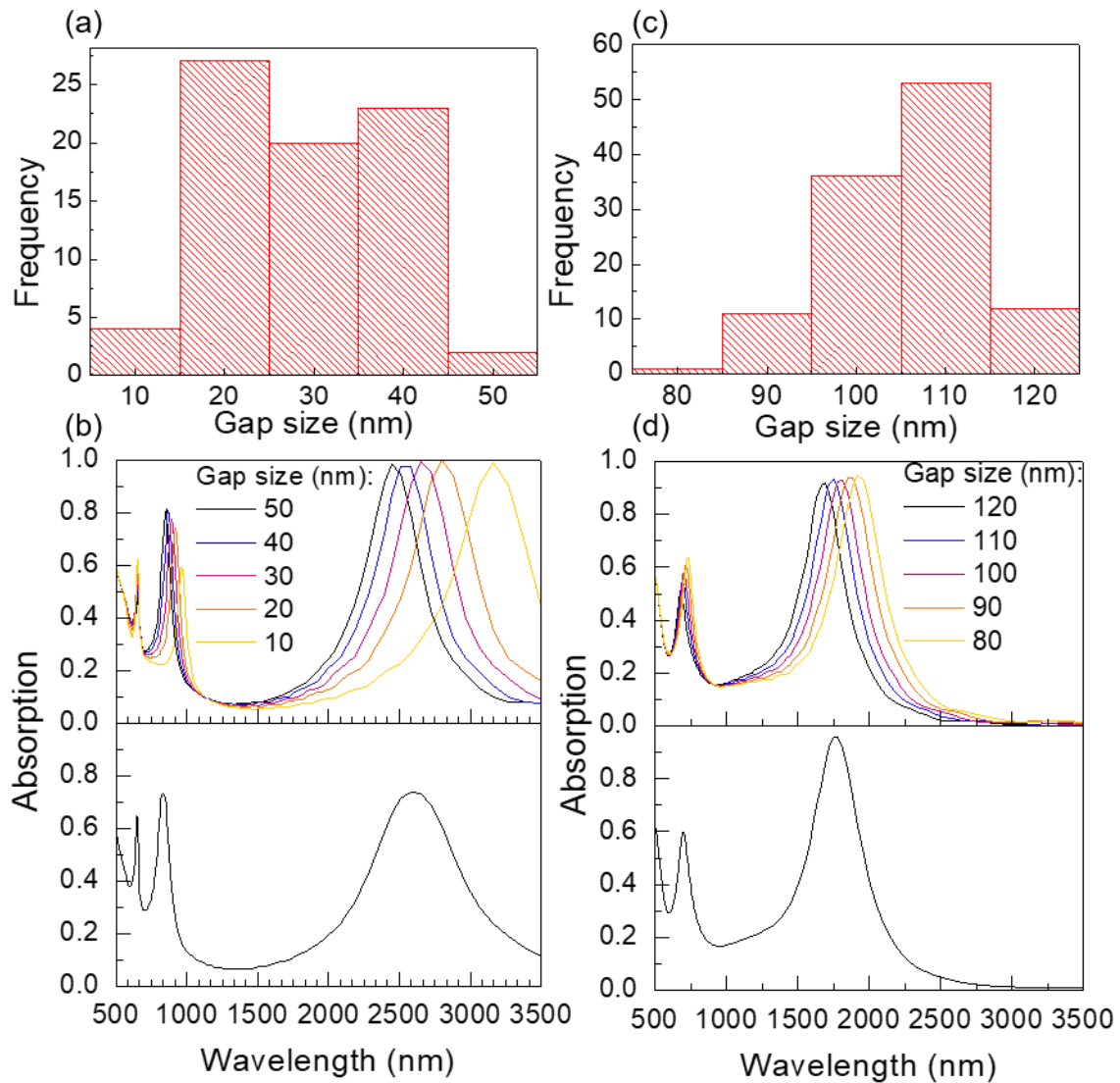


Figure 6.9. Effect of the gap distribution in the absorption spectra for two asterisk arrays with pitch of 400 nm (a)-(b) and pitch of 500 nm (c)-(d), respectively, both metallized with 0.5 nm Cr + 20 nm Au and fabricated on a substrate with MIM configuration, being the spacer layer 100 nm of SiO₂. (a) and (c) show the gap distributions obtained from the SEM images in Figure 6.5(b)-(c). Top (b) and (d) panels show the simulated absorption spectra as a function of the gap size, while bottom panels show the resulting averaged curves according to the distributions in (a) and (c) panels, respectively.

The first correction simply redshifts slightly the position of the peaks as compared to the ‘perfect asterisk’ (Fig. 6.8(a)). However, the addition of the central cylinder suppresses the high absorption peak in the visible (Fig. 6.8(b)). This makes sense if one recalls the electric field distribution of the system

presented in Chapter 4, as the main enhancement of the electric field in this high-energy mode corresponds to a concentration of the electric field in the V-shape formed by the intersection of the bars, which no longer exists with the addition of a central cylinder. To correct for this, inwards rounded junctions were added, yielding again a high absorption peak in the visible (Fig. 6.8(c)), although partially suppressed as compared to the sharp V-shaped junction.

Another factor that should be taken into account is the actual distribution of sizes, in particular in the gaps' width, which is evident in the nearly-touching structures shown in Figure 6.5(b)-(c). The latter is a key factor in the NIR peak and the near-field coupling between nanoelements.

Adhesion layer

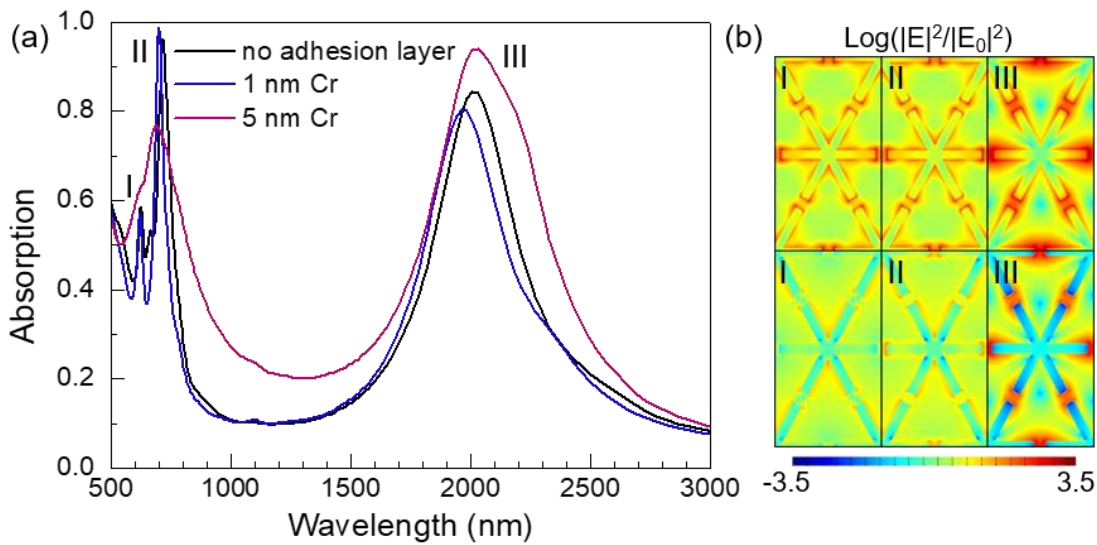


Figure 6.10 (a) Simulated absorption spectra for an array of asterisks of 500 nm / 450 nm / 45 nm / 30 nm with different Cr thickness as adhesion layer. (b) $\text{Log}(|E|^2/|E_0|^2)$ for the peaks in (a) for the no adhesion layer (top) and the 5 nm Cr adhesion layer (bottom) cases, taken at $z=15$ nm, just at half of the thickness of the nanoelements.

It is well known that Au adheres poorly to substrates and, therefore, it is common to use adhesion layers. However, the use of Ti and Cr, that are the most extended materials to promote Au adhesion, results in a damping of the plasmonic response.^{5,6} Figure 6.10 shows the absorption for different Cr adhesion

layers. While the NIR maximum in the absorption spectrum is only slightly affected, the absorption in the visible is drastically reduced for the 5 nm- thick Cr layer and the two peaks are broadened and merged together. This fact is in agreement with the results obtained for FTIR where, instead of two sharp peaks in the visible, only one broader peak appears, whatever the design of the sample may be.

Taking these results into account, we tried to avoid the use of these adhesion promoters, however, some structures went away during the lift-off process and many of the arms of the stars were also either deformed or broken (see Figure 6.11). Finally, we managed to use 0.5-2 nm thick adhesion layers, minimizing that way the effect that Ti and Cr may have in the response of the system.

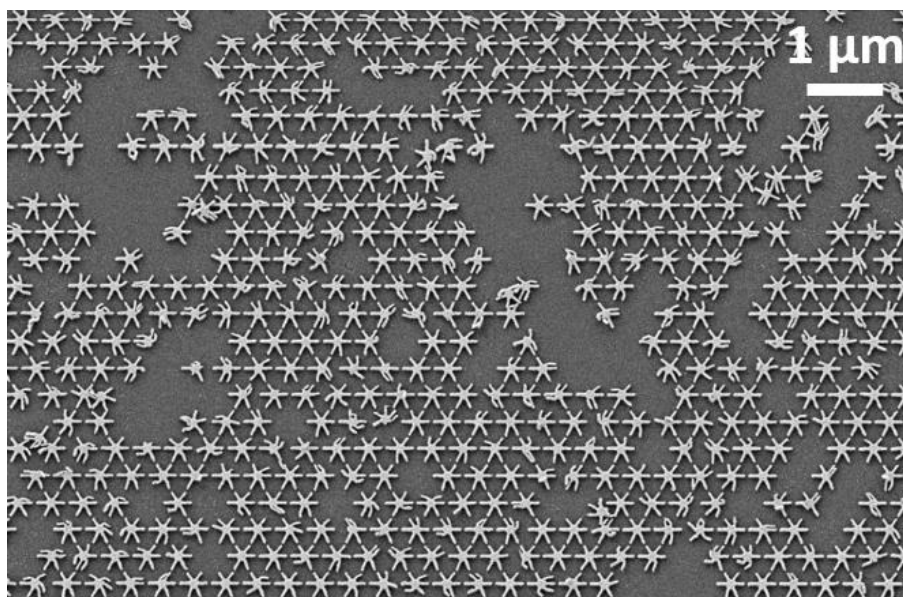


Figure 6.11 SEM micrograph showing the poor adhesion of a sample with 30 nm of Au deposited without adhesion layer, deposited by *e*-beam evaporation.

6.2.6. Arrays of nanoasterisks as substrates for SERS

First attempts to use these samples as substrates for SERS have been performed by functionalizing the samples with 4-Mercaptopyridine (also known as 4-Pyridinethiol) (4-Mpy). The enhancement of the Raman intensity of 4-Mpy has already been reported using colloidal nanoparticles^{7,8} and substrates.⁸

Thanks to the thiol group, 4-Mpy adheres easily to Au and Ag structures, making functionalization easy.

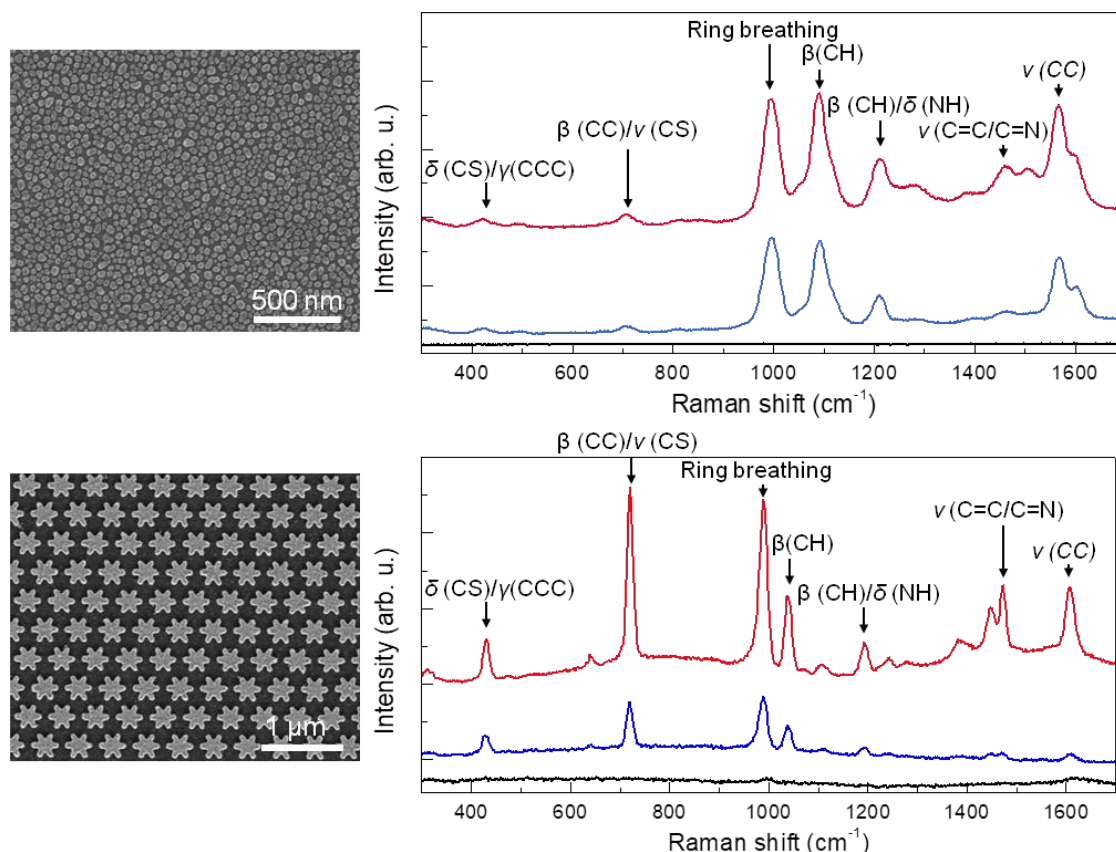


Figure 6.12 SEM micrographs (left) and corresponding Raman measurements (right) for a sample of Ag nanoparticles and an array of Au nanoasterisks. The Raman measurements have been performed in three cases: prior to functionalization (black), after functionalization with a drop of 1 μl of 10^{-3} M 4-Mpy in water (blue), and after letting the drop dry (red) for both substrates.

Measurements were performed on a substrate with Ag nanoparticles and on a sample with asterisks of 400 nm / 300 nm / 30 nm / 1 nm Ti + 20 nm Au. Figure 6.12 shows the SEM micrographs of the sample (left) and the Raman measurements (right). Measurements were done prior to functionalization (black), after functionalization with a 1 μl drop of 10^{-3} M solution of 4-Mpy (blue) and after letting the solution dry (red). The most remarkable vibrations are indexed in the spectra. Figure 6.12 shows that our structures exhibit better defined peaks than those of Ag nanoparticles. The peaks corresponding to the ring breathing and $\beta(\text{CC})/\nu(\text{CS})$ are particularly enhanced and peaks that are

hardly distinguishable for the Ag nanoparticles, like the $\nu(\text{C}=\text{C}/\text{C}=\text{N})$ and the $\delta(\text{CS})/\gamma(\text{CCC})$ ones, are much better defined using the Au asterisks.

6.3. Experimental results regarding the honeycomb lattice of bars and the triangular lattice of dots.

Following the same procedure, the honeycomb lattice of bars and the triangular lattice of dots have also been fabricated. Figure 6.13 shows the SEM micrographs and absorption spectra obtained for the honeycomb lattice designed to have 1500 nm/300 nm/40 nm/0.5 nm Cr + 20 nm Au fabricated by EBL with a dose of 180 $\mu\text{A}/\text{cm}^2$ at 20 kV and with a step size of 10 nm. The DF for the tilted bars was double than that of the horizontal ones to obtain the same thickness. The SEM micrographs in Figure 6.13(a) show that some columns of horizontal bars are thinner than others are. This is probably due to the fact that as the bars are designed to be only 40 nm thick, and the step size is 10 nm, possibly one step less is taken in those bars which results in a visible difference.

Different areas have been fabricated increasing the DF from 1 to 1.5 in the same MIM substrate, which is exactly the same as the one used for the fabrication of the asterisks (Si + 5 nm Ti + 60 nm Au + 100 nm SiO₂). The absorption spectra obtained by FTIR shown in Figure 6.13 (a) reveals how sensitive the response is to changes in the fabrication process: by increasing the dose factor from 1 to 1.5, the absorption is increased in the three peaks, probably as a consequence of the increased size of the structures. However, the change in the peak around 950 nm is remarkably greater than for the other cases: while for the sample with a DF=1 the peak is barely detectable, for a DF=1.5 this peak turns into a very sharp peak.

Figure 6.13 (b) shows the absorption spectra for two samples where some of the patterns are contacted. As a result, the NIR peak is less intense and two new peaks appear at higher energies, but still above the visible. However, it is interesting to notice that the response in the visible is barely affected.

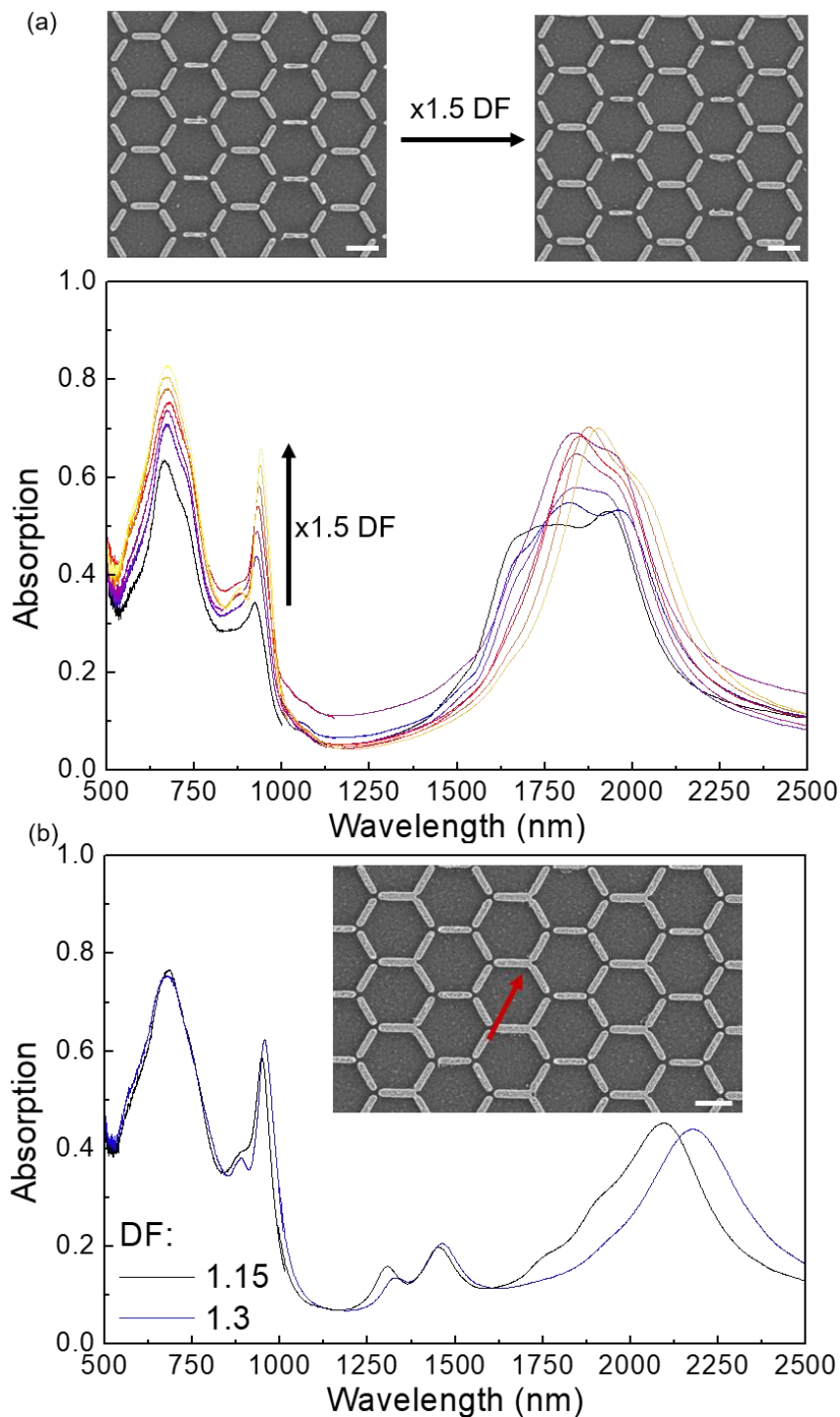


Figure 6.13 (a) Absorption spectra for several honeycomb samples, where the dose factor (DF) during EBL has been changed from 1 to 1.5. The two SEM micrographs on top correspond to the samples with DF equal to 1 (left) and 1.5 (right). (b) Absorption spectra for samples where some of the structures are connected, as shown in the inset. The scale bar corresponds to 500 nm.

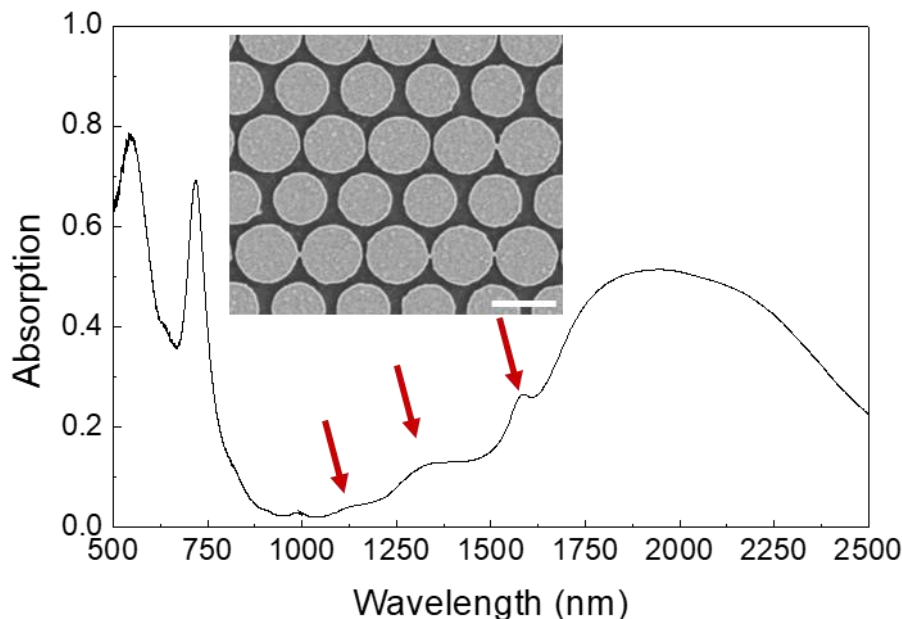


Figure 6.14 Absorption spectrum for an array of disks in a triangular lattice with pitch of 500 nm. The scale bar corresponds to 500 nm.

The array consisting in disks in a triangular lattice has also been fabricated on the same substrate. The sample is designed to have a pitch of 500 nm. Figure 6.14 displays the absorption spectrum and a SEM micrograph in the inset. Although there are two characteristic sizes of disks due to some fabrication issues, the spectrum resembles that of Chapter 5 obtained by numerical simulation.

6.4. Conclusions and further work

Along this chapter, the feasibility of the fabrication of the plasmonic arrays presented in Chapter 5 has been proved. FTIR measurements agree well with simulations, except for the experimental broadening of the peak in the visible, presumably due to the combined effect of the adhesion layer, the roughness of the metal layer, and the rounded shapes of the fabricated structures, as thoroughly discussed in section 6.2.5.

Besides, preliminary results from Raman spectroscopy show that these structures can be suitable for SERS. The functionalization of the samples with 4-Mpy resulted in enhanced intensities of the characteristic vibrations of the

molecule. As further work, the fabrication should be optimized to match the absorption peaks with the laser frequency for Raman spectroscopy and the functionalization of the substrate should be improved to be able to detect lower analyte concentrations.

Measurements also reveal that when the size of the elements is increased by slightly increasing the dose factor during the EBL fabrication, some elements become connected to each other. As a consequence, the absorption is modified by the appearance of small additional peaks in the region between the broad IR peak and the visible peaks. However, the collective resonances lying on the visible region of the spectrum are not affected as these defects affect the sample only locally and hence they are only reflected in the NIR peak. By further increasing the dose, the amount of connected elements should increase until all of the elements formed a connected lattice. Therefore, it would be of interest to analyze the effect of larger amounts of defects in the sample, by increasing either the connectivity of the structures until the connected lattice or, just the opposite, removing elements from the lattice and studying the response as a function of the faults in the lattice to find out when the collective response of the system changes.

6.5. References

1. Johnson, P. B., Christy, R. W. & PB Johnson, R. C. Optical Constants of Noble Metal. *Phys. Rev. B* **6**, 4370–4379 (1972).
2. Palik, E. D. *Handbook of optical constants of solids. Most 1*, (Academic Press, 1985).
3. Haynes W. M. *CRC Handbook of Chemistry and Physics, 97th Edition. CRC Handbook of Chemistry and Physics* (2017). doi:10.1136/oem.53.7.504
4. Léron del, G., Kostcheev, S. & Plain, J. in *Springer Series in Optical Sciences* 269–316 (2012). doi:10.1007/978-3-642-28079-5_9
5. Habteyes, T. G. *et al.* Metallic Adhesion Layer Induced Plasmon Damping and Molecular Linker as a Nondamping Alternative. *ACS Nano* **6**, 5702–5709 (2012).
6. Brown, L. V. *et al.* Fan-Shaped Gold Nanoantennas above Reflective Substrates for Surface-Enhanced Infrared Absorption (SEIRA). *Nano Lett.* **15**, 1272–1280 (2015).
7. Nalbant Esenturk, E. & Hight Walker, A. R. Surface-enhanced Raman scattering spectroscopy via gold nanostars. *J. Raman Spectrosc.* **40**, 86–91 (2009).
8. Hu, J., Zhao, B., Xu, W., Li, B. & Fan, Y. Surface-enhanced Raman spectroscopy study on the structure changes of 4-mercaptopyridine adsorbed on silver substrates and silver colloids. *Spectrochim. Acta A* **58**, 2827–2834 (2002).

General conclusions

This Ph.D. Thesis has been devoted to the study of different Au nanostructures, including their fabrication by nanolithographic tools, simulation of their plasmonic response, and their optical characterization. The most significant contributions from the studies developed throughout these years are given below.

Cylindrical Au nanocups.

- Arrays of 1 cm^2 of Au hollow cylindrical nanostructures have been obtained combining nanoimprint lithography (NIL) with sputtering metallization. A trilayer stack has been used, which is composed of a bottom resist layer that controls the height of the nanostructures, a thin (20-30 nm) SiO_2 layer that acts as a mask for the bottom resist layer etching, and a top resist layer where the NIL process takes place. In this way, the height of the nanostructures is independent of the lithography step and, hence, the height aspect ratio limitation of NIL is overcome.
- The fabrication process enables easy changes of the geometry. The height of the nanostructures is tuned by changing the thickness of the bottom resist layer. The diameter can be modified to a certain extent by changing the etching time. Finally, the thickness of the wall is monitored as a function of the amount of deposited material. This tunability has been proven by fabricating a set of samples with nanoelements of various dimensions and dense arrays of nanostructures as well. This process could be also adapted to fabricate other types of structures or to combine different materials. Also, using electron beam evaporation, solid structures such as dots or cones can be obtained.
- FDTD simulations have shown that the extinction of the nanostructures can be easily tuned by changing their geometry.

- Non-interacting nanocups of 400 nm in both diameter and height, and 30 nm in thickness of both walls and base, present an extinction spectrum with two peaks, one in the visible and one in the IR regions of the EM spectrum. The first peak is associated with an enhancement of the electric field inside the cavity of the nanostructure. When both the diameter and height of the cavity are of the order of the incident half wavelength, a kind of resonance phenomenon takes place resulting in a large enhancement of the electric field within the cavity. This resonant behavior could be used for example for SERS, to enhance the response of molecules placed inside the cavity, provided the resonance takes place at the excitation laser wavelength.
- Using a MIM configuration, superabsorbing substrates have been fabricated using the densely-packed Au nanocups. These structures absorb over 80% of light in the range of the spectrum between 400 and 1000 nm.

Geometric frustration in arrays of plasmonic nanoelements.

- Inspired by geometrically frustrated magnetic systems, hexagonal lattices of plasmonic nanoelements have been studied aiming at finding an analogue behavior. In particular, three different arrays have been studied: triangular lattices of disks and asterisks and a honeycomb lattice of bars, all of them designed in a similar manner:
 - A MIM configuration has been used to enhance absorption.
 - The pitch of the arrays and the element size have been chosen such that the gaps between neighboring elements are small enough to yield strong near-field coupling through the gaps.
- According to simulations, the three systems share some common features:
 - Far-field interactions among the elements give rise to higher-order collective modes that are compatible with the translational symmetry of the lattice and can be understood as surface lattice resonances.
 - Dipolar excitation of the gaps is geometrically frustrated in these hexagonal lattices for interactions beyond nearest neighbors. As a consequence, the systems fluctuate through a variety of excitation modes arising from combinations of the localized near-field modes and the collective surface lattice resonances. This in turn results in a slow dynamics of the optical response, a behavior similar to that of

geometrically frustrated magnetic systems. These two kinds of modes give rise to two high absorption peaks located around the NIR (localized modes) and VIS (collective modes). These systems present enhancements of the electric field not only in the gaps between neighboring elements, but also in larger areas.

- The arrays have been fabricated using EBL to do fast prototyping of various geometries.
- FTIR spectroscopy results are in good agreement with the numerical simulations.
- Considering the slow dynamics of the system and the occurrence of non-localized enhanced electric fields over large areas, these systems may be of interest as enhancers for applications related to light absorption or enhanced spectroscopies. First results indicate that these systems can be used as substrates for SERS.

There is plenty of room for further improvement, for example, regarding the design of the structures and specially their use for particular applications. Some issues remained unexplored, e.g., the use of other adhesion layers with less effect on the plasmonic properties, or the role of the roughness on both the plasmonic response and the SERS signal. Geometrically frustrated arrays of nanoelements might be further optimized and it would be of interest to keep exploring different geometries. Today, the efforts are mainly focused on optimizing the substrates for SERS and finding new interesting lattices to fabricate.

Apart from all the relevant results detailed above, I have come to a very important conclusion: I feel that I have acquired valuable knowledge that is not explicitly described in this manuscript that comes, most probably, from failures and mistakes. And, what is more important, with some time and ability, some of those “failures” will become new successes.

“Progress is made by trial and failure; the failures are generally a hundred times more numerous than the successes; yet they are usually left unchronicled.”

Sir William Ramsay

Appendix A

FDTD simulations

A.1. Introduction

Simulating the interaction of light with metallic structures to test ideas, optimize parameters, and solve problems is a key challenge in plasmonic research. Maxwell equations for complex geometries cannot be solved analytically. Therefore, a variety of numerical methods based on different discretization processes have been developed, where the complex problem is approximated using a set of analytical functions, solved by a certain algorithm to give approximate solutions. Therefore, the simulation methodology can be very complicated.

FDTD is one of the most common approaches used to simulate broadband electromagnetic problems, being Lumerica¹ the most extended commercial software. Along with Comsol Multiphysics,² that uses the Finite Element Method (FEM), and other numerical approaches, these types of software make it possible to deal with a wide variety of systems that, otherwise, could not have been solved.

The aim of this Appendix is to clarify some of the details related to the simulations presented along this manuscript. For further technical information one can refer to Lumerical's web page.¹

A.2. FDTD simulations in Lumerical

All the simulations shown in this manuscript have been performed using a commercial-grade simulator based on the finite-difference time-domain method by Lumerical Solutions, Inc.¹

A.2.1. Meshing

The software uses a rectangular, Cartesian style mesh. By default, the simulation mesh is automatically chosen, creating a smaller mesh in both higher index materials, to keep constant the number of mesh points per wavelength, and highly absorbing materials, to account for penetration depths. However, this mesh is usually not enough in complex structures with large field variations and additional meshing is required. Also, at the interfaces the field can be discontinuous and the positions at the interface cannot be resolved better than the minimum spatial increment.

The first solution for this is the use of a graded mesh that reduces the mesh size near interfaces. However, sometimes this is not enough. As a matter of fact, the standard Yee cell FDTD algorithm does not account for structure variations within a Yee cell and results in a ‘staircase’ permittivity mesh, that coincides with the Cartesian mesh as the classical approach is to use a weighted volume average to obtain an effective dielectric constant that does not account for the actual geometry of the material. As a consequence, the same result is obtained for different cases. Conformal mesh technologies (CMTs) try to improve the results by integrating Maxwell’s equations near boundaries. For example, the Yu-Mittra model can be used in curved Perfect Electrical Conductor (PEC) surfaces, reducing the contour integral to include only the region outside the PEC where the electric field is non-zero.³ Lumerical has developed a conformal mesh technology (CMT) that uses an integral solution of Maxwell’s equations near interfaces and offers the possibility to choose between different options:

Conformal Variant 0: is the default option and applies CMT to all materials except metals (defined as $Re(\epsilon) < 1$) and PEC.

Conformal Variant 1: CMT is applied to all materials but can give worse results than the previous case for a large mesh.

Conformal Variant 2: Yu-Mittra model is applied to PEC and metals.

This CMT enhances the simulation accuracy for a given mesh size (dx) and is faster due to the $(1/dx)^4$ dependence of the simulation time with the mesh size. The memory requirements scale as $\sim V \cdot (\lambda/dx)^3$ and time as $\sim V \cdot (\lambda/dx)^4$ in 3D simulations.

To further control the mesh, there is a mesh accuracy slider that goes from 1 to 8 meaning that $\lambda/dx = 6, 10, 14, 18, 22, 26, 30, 34$, being $\lambda = \lambda_0/n$, where n is the refractive index. Usually mesh accuracy of 2 is considered reasonable and 4-5 very high.

A.2.2. Material modelling

Lumerical offers the user a vast materials database with experimental data and parametrized models of the dielectric constant/refractive index of the most common materials in the field of plasmonics. For dispersive materials, Lumerical also offers the possibility to introduce data, either experimental or theoretical, by entering (n, k) data as a function of wavelength using the sampled material option. Also, the dielectric properties can be described with several models, including dielectric ($\epsilon_r(\omega) = n^2 = \text{constant for } n \geq 1$), PEC, conductive, plasma, Debye, Lorentz, Sellmeier or other nonlinear and advanced configurations such as Chi2, Chi2/3, Kerr nonlinear or paramagnetic methods.

Drude, Debye or Lorentz models, which are widely used in the field of plasmonics to account for the dispersive behavior of materials, are idealizations that usually fail to describe real materials in broadband simulations. To overcome this limitation, Lumerical offers the possibility to use the multi-coefficient materials model (MCMs) that uses a set of functions to better fit the response of materials that cannot easily be described by the classical approaches. The user can tune the number of coefficients and the fit tolerance until the model reproduces correctly the data introduced in the database.

A.2.3. Boundary conditions

The boundaries of the simulation region can be designed in several ways by choosing the appropriate boundary conditions (BCs):

Perfectly Matched Layers (PMLs): PMLs are designed to absorb the outgoing waves by impedance match to the simulation region and the materials it contains.⁴ They are characterized by absorbing all the incident field, no matter the frequency or incident angle. The current version (introduced in 2015) was designed based on the stretched coordinate formulation proposed by Gedney and Zhao.⁵ This type of BCs is used for simulations in which the fields should propagate away from the simulation region. PMLs should be placed at least half a wavelength away from the scattering objects to avoid interactions with the evanescent fields.

Metal: They are perfect metal boundaries that reflect all the light.

Bloch: Used to simulate periodic structures, they can be used wherever the structure and the fields are periodic and can be used when the source has not normal incidence.

Periodic: It is a particular case of Bloch conditions intended for cases in which $k=0$ and requires only half of the memory Bloch BC require.

Besides these BCs, one can use the (anti)symmetry of the system to reduce memory and time as long as both structures and fields are (anti)symmetric. To simulate periodic structures, the minimum and maximum BCs can be set to be symmetric and antisymmetric, simulating only one quarter of the unit cell.

A.2.4. Sources

Lumerical offers the possibility to work with a variety of sources, including point sources (dipoles), Gaussian and Cauchy/Lorentzian beam sources, plane wave sources or even to import a customized profile.

The case of the total-field scattered-field source (TFSF) is of special interest. This type of sources divide the simulation region in two different zones: a region with the total field (incident plus scattered field) inside the TFSF source area

and a region outside the TFSF source area where only the scattered field is present. The incident field is a plane wave with a wave vector normal to the injection surface.

A.2.5. Simulations with unpolarized light

All common sources of light, including the Sun or incandescent and fluorescent lights, provide unpolarized light. Hence, it is of great importance to be able to simulate this kind of light. However, Lumerical does not offer directly any source of unpolarized light. To obtain the response of an unpolarized wave, all the possible polarization need to be averaged:

$$\langle |E|^2 \rangle = \frac{1}{2\pi} \int_0^{2\pi} |\vec{E}(\theta)|^2 d\theta$$

Due to the linearity of Maxwell's equations, one can represent the electric field of an arbitrarily polarized wave as the sum of two orthogonal polarizations:

$$\vec{E}(\theta) = \vec{E}_s \sin(\theta) + \vec{E}_p \cos(\theta)$$

Hence, integrating:

$$\begin{aligned} \langle |E|^2 \rangle &= \frac{1}{2\pi} \int_0^{2\pi} |\vec{E}(\theta)|^2 d\theta = \frac{1}{2\pi} \int_0^{2\pi} |\vec{E}_s \sin(\theta) + \vec{E}_p \cos(\theta)|^2 d\theta \\ &= \frac{1}{2\pi} \int_0^{2\pi} \left(|\vec{E}_s|^2 \sin^2(\theta) + |\vec{E}_p|^2 \cos^2(\theta) + 2|\vec{E}_s \vec{E}_p| \sin(\theta) \cos(\theta) \right) d\theta = \\ &= \frac{|\vec{E}_s|^2}{2\pi} \int_0^{2\pi} \sin^2(\theta) d\theta + \frac{|\vec{E}_p|^2}{2\pi} \int_0^{2\pi} \cos^2(\theta) d\theta + \frac{2|\vec{E}_s \vec{E}_p|}{2\pi} \int_0^{2\pi} \sin(\theta) \cos(\theta) d\theta \end{aligned}$$

Taking into account that:

$$\int_0^{2\pi} \sin^2(\theta) d\theta = \pi \quad \int_0^{2\pi} \cos^2(\theta) d\theta = \pi \quad \int_0^{2\pi} \sin(\theta) \cos(\theta) d\theta = 0$$

the integral results in:

$$\langle |E|^2 \rangle = \frac{1}{2} (|\vec{E}_s|^2 + |\vec{E}_p|^2)$$

Thus, it is sufficient to perform two simulations with sources with orthogonal polarization and add the results incoherently. The result of transmission or absorption for unpolarized light is calculated by simply averaging the transmissions of the two simulations.

A.3. References

1. Lumerical Inc. | Innovative Photonic Design Tools.
2. COMSOL Multiphysics® Modeling Software.
3. Wenhua Yu & Mittra, R. A conformal finite difference time domain technique for modeling curved dielectric surfaces. *IEEE Microw. Wirel. Components Lett.* **11**, 25–27 (2001).
4. Berenger, J.-P. A perfectly matched layer for the absorption of electromagnetic waves. *J. Comput. Phys.* **114**, 185–200 (1994).
5. Gedney, S. D. & Zhao, B. An Auxiliary Differential Equation Formulation for the Complex-Frequency Shifted PML. *IEEE Trans. Antennas Propag.* **58**, 838–847 (2010).

Appendix B

List of publications and contributions to scientific events

B.1. Peer-reviewed publications

(1) Alayo, N.; Conde-Rubio, A.; Bausells, J.; Borrisé, X.; Labarta, A.; Batlle, X.; Pérez-Murano, F. *Nanotechnology* 2015, 26 (44), 445302.]].

(Labtalk <http://iopscience.iop.org/0957-4484/labtalk-article/63030>)

(2) Kovylyna, M.; Alayo, N.; Conde-Rubio, A.; Borrisé, X.; Hibbard, G.; Labarta, A.; Batlle, X.; Pérez-Murano, F. *Appl. Phys. Lett.* 2015, 107 (3).

(3) Conde-Rubio, A.; Fraile Rodríguez, A.; Borrisé, X.; Pérez-Murano, F.; Batlle, X.; Labarta, A. *Geometric frustration in a hexagonal lattice of plasmonic nanoelements* (submitted)

(4) Conde-Rubio, A.; Fraile Rodríguez, A.; Mihi, A.; Pérez-Murano, F.; Batlle, X.; Labarta, A. *Topological frustration in hexagonal lattices of plasmonic nanoelements: influence of the lattice* (in preparation)

B.2. Contributions to scientific events

International Conference on Magnetism 2018, San Francisco (USA), July 2018

Oral contribution: Geometric frustration in a hexagonal array of plasmonic nanoelements (Conde-Rubio, A; Fraile Rodriguez, A.; Pérez-Murano, F; Batlle, X and Labarta, A.)

X GEFES Meeting 2018, Valencia (Spain), January 2018

Oral contribution: Plasmonic lattices with high absorption and extended time response (Conde-Rubio, A; Borrísé, X; Fraile Rodriguez, A.; Pérez-Murano, F; Batlle, X and Labarta, A.)

NALS2017, Nanomaterials applied to life sciences, Gijón (Spain), December 2017

Invited contribution: Plasmonic nanoelements and lattices as platforms for biosensing (Conde-Rubio, A; Borrísé, X; Fraile Rodriguez, A.; Pérez-Murano, F; Batlle, X and Labarta, A.)

3rd Scientific Meeting of BNC-b PhD students, Bellaterra (Spain), November 2017

Oral contribution: Plasmonic response of a triangular array of nanogaps with high absorption and extended temporal response (Conde-Rubio, A.; Espinha, A.; Borrísé, Fraile Rodriguez, A; X.; Mihi,A.; Pérez-Murano, F.; Batlle, X.; Labarta, A.)

7th Nanolito Workshop, Madrid (Spain), October 2017

Oral contribution: Plasmonic response of a triangular array of nanogaps: high absorption and extended temporal response (Conde-Rubio, A.; Borrísé, Fraile Rodriguez, A; X.; Pérez-Murano, F.; Batlle, X.; Labarta, A.)

43rd International Conference on Micro and Nanoengineering (MNE 2017), Braga (Portugal), September 2017

Poster contribution: The plasmonic response of a hexagonal array of nanogaps (Conde-Rubio, A; Borrísé, X; Fraile Rodriguez, A.; Pérez-Murano, F; Batlle, X; and Labarta. A)

Nineteenth Annual YUCOMAT Conference, Herceg Novi (Montenegro), September 2017

Appendix B. List of publications and contributions to scientific events

Invited contribution: Au nanocups as optical tunable nanoresonators (Conde-Rubio, A; Pérez-Murano, F; Labarta. A; and Batlle, X)

ICSS & EMN Nanoparticles Meeting, San Sebastián (Spain), May 2017

Oral contribution: Au nanocups as optical tunable nanoresonators (Conde-Rubio, A; Pérez-Murano, F; Labarta. A; and Batlle, X)

10th Anniversary IN2UB, Barcelona (Spain), January 2017

Oral contribution: Plasmonics: light at the nanoscale (Conde-Rubio, A; Pérez-Murano, F; Labarta. A; and Batlle, X)

JPHD2016, 2nd scientific meeting of BNC-b students, Bellaterra (Spain), June 2017

Oral contribution: Plasmonics: light at the nanoscale (Conde-Rubio, A; Pérez-Murano, F; Labarta. A; and Batlle, X)

12th Nanoscience and Nanotechnology Conference (NANOTR-12), Kocaeli (Turkey), June 2016

Invited contribution: Plasmonic hollow cylindrical nanostructures fabricated by Nanoimprint Lithography and non-directional metallization (Conde-Rubio, A; Alayo, N; Borrisé, X; Pérez-Murano, F; Labarta. A; and Batlle, X)

Jornada d'Investigadors Predoctorals Interdisciplinària (JIPI), Barcelona (Spain), February 2016

Oral contribution: A brief introduction to the nanoworld! (Conde-Rubio, A; Evangelio, L; Gottlieb, S.)

20th International Conference on Magnetism (ICM) 2015, Barcelona (Spain), July 2015

Poster contribution: Plasmonic hollow cylindrical nanostructures fabricated by Nanoimprint Lithography and non-directional metallization (Conde-Rubio, A; Kovylyna, M.; Alayo, N; Borrisé, X; Pérez-Murano, F; Hibbard, G; Labarta. A; and Batlle, X)

Poster contribution: Multifunctional Fe-Au heterogeneous thin-films (Conde-Rubio, A; Kovylyna, M; Labarta, A; and Batlle, X))

Appendix B. List of publications and contributions to scientific events

IEEE Magnetism Summer School, Minneapolis (USA), June 2015

Poster contribution: Multifunctional Fe-Au heterogeneous thin-films (Kovylyna, M.; Conde-Rubio, A.; Labarta, A.; and Batlle, X)

JPHD2015, 1st scientific meeting of bnc-b students, Bellaterra (Spain), May 2014

Oral contribution: Plasmonic hollow cylindrical nanostructures fabricated by Nanoimprint Lithography and non-directional metallization (Conde-Rubio, A.; Kovylyna, M.; Alayo, N.; Borrísé, X.; Pérez-Murano, F.; Hibbard, G.D.; Batlle, X.; Labarta, A.)

International Society for Optics and Photonics SPIE. Advance Lithography. Symposium: Alternative Lithographic Technologies VII, San José (USA), February 2015

Oral contribution: A nanoimprint lithography based fabrication route to obtain metallic nanoparticle of diverse/tunable shape (Alayo, N.; Conde, A.; Kovylyna, M.; Borrísé, X.; Bausells, J.; Hibbard, G.; Labarta, A.; Batlle, X.; Pérez-Murano, F.)

6th Nanolito Workshop, Zaragoza (Spain), October 2014

Oral contribution: Plasmonic hollow cylindrical nanostructures fabricated by Nanoimprint Lithography and non-directional metallization (Conde-Rubio, A.; Kovylyna, M.; Alayo, N.; Borrísé, X.; Pérez-Murano, F.; Hibbard, G.D.; Batlle, X.; Labarta, A.)

Novel Frontiers of Magnetism, 2014 Winter Meeting Club Español de magnetism, Benasque (Spain), February 2014

Poster contribution: Multifunctional Fe-Au heterogeneous thin-films (Kovylyna, M.; Conde, A*; Labarta, A.; and Batlle, X)

VIII GEFES Meeting 2014, Ciudad Real (Spain), January 2014

Poster contribution: Multifunctional Fe-Au heterogeneous thin-films (Kovylyna, M.; Conde, A.; Labarta, A.; Batlle, X)

Nanoimprint and Nanoprint Technology (2013), Barcelona (Spain), October 2013

Poster contribution: Functional nanoparticle arrays fabricated by nanoimprint lithography with applications in plasmonics and nanomagnetism (Alayo, N.; Pérez-Murano, F.; Borrísé, X.; Kovylyna, M.; Conde, A.; Labarta, A.; Batlle, X.)

Appendix B. List of publications and contributions to scientific events

39th Micro and Nanoengineering (MNE) 2013, London (UK), September 2013

Poster contribution: Functional nanoparticle arrays fabricated by nanoimprint lithography with applications in plasmonics and nanomagnetism (Alayo, N.; Kovylyna, M.; Conde, A.; Labarta, A.; Batlle, X.; Llobet, J.; Borrisé, X.; Pérez-Murano, F.)

Resumen

Esta tesis está dedicada a la nanofabricación, simulación y caracterización de las propiedades plasmónicas de diferentes nanoestructuras de oro.

Cuando una onda electromagnética incide sobre una nanoestructura metálica puede producir oscilaciones colectivas de la nube de electrones libres del metal. Estas oscilaciones llegan a un máximo a una cierta longitud de onda, conocida como resonancia del plasmón de superficie, cuya intensidad y frecuencia dependen de factores tales como el material, la forma, el tamaño y el medio en el que se encuentra la estructura. De este fenómeno se han beneficiado diversos campos donde se explota por ejemplo la posibilidad de conseguir confinar la luz en espacios nanométricos o el aumento de la absorción o de la difusión de la luz o su direccionalidad. Éste es el caso de la fotovoltaica, nanomedicina, óptica, sensores y un largo etcétera.

Las condiciones para que un material tenga buenas propiedades plasmónicas recaen sobre su función dieléctrica, y en particular en que la parte real de su función dieléctrica sea negativa y grande y la parte imaginaria, asociada a pérdidas por absorción, sea lo más pequeña posible. Por ello, metales como el oro son apropiados para este tipo de sistemas.

Para obtener las frecuencias de resonancia de las estructuras y los modos de excitación se deben resolver las ecuaciones de Maxwell. Sin embargo, estas ecuaciones pueden resolverse analíticamente solo para los casos sencillos y casi siempre es necesario el uso de métodos numéricos. En particular, en esta tesis, se ha utilizado el paquete de simulaciones de elementos finitos en el dominio temporal (FDTD) de Lumerical.

La tesis puede está dividida fundamentalmente en dos partes: la primera se centra en el estudio de nanoestructuras de oro cilíndricas en forma de taza (Section II) y en la segunda se analizan redes frustradas de nanoelementos plasmónicos (Section III).

Son muchos los artículos y estudios dedicados a nanopartículas plasmónicas con estructura *core-shell* (compuestas por una corteza metálica y un núcleo típicamente dieléctrico) gracias a la gran capacidad de ajuste de sus propiedades ópticas en función de su geometría, pudiendo desplazar la longitud de onda de resonancia centenares de nanómetros. Basados en estas propiedades, hemos fabricado nanoestructuras de oro cilíndricas en forma de taza, fabricadas combinando litografía por nanoimpresión con metalización por pulverización catódica. Además, para tener la posibilidad de fabricar estructuras de una elevada altura frente a su anchura, se ha utilizado una tricapa de resina-óxido-resina, de manera que la capa inferior de resina controla la altura de las estructuras mientras que la litografía se realiza en la capa superior y por tanto se sobreponen las típicas dificultades que aparecen en la litografía de nanoimpresión para estructuras de elevada relación de aspecto. Estas nanoestructuras, al igual que las nanopartículas con estructura *core-shell*, presentan también gran capacidad de ajuste de sus propiedades como función del diámetro, altura y grosor de las mismas. El método de fabricación permite cambiar fácilmente la geometría de las estructuras, facilitando el ajuste de las propiedades plasmónicas de las mismas hasta el punto deseado. Además, para ciertas dimensiones (400 nm de diámetro y altura y 30 nm de grosor) estas estructuras presentan un pico en el visible que corresponde a una concentración del campo eléctrico en el interior de la cavidad. Este modo de excitación se ha visto también en otro tipo de estructuras con geometría cilíndrica, sin embargo, el hecho de tener simetría cilíndrica hace que el aumento del campo eléctrico se produzca de forma homogénea en toda la cavidad, algo que no ocurre en el caso de geometría esférica. Además, el uso de una configuración metal-aislante-metal hace que estas estructuras funcionen como absorbentes de alto espectro, consiguiendo absorber por encima del 80% de la luz en el rango de 400 a 1000 nm.

Por otro lado, basados en los sistemas magnéticos con frustración geométrica se han estudiado diferentes redes hexagonales de nanoelementos de oro, buscando propiedades análogas en el campo de la plasmónica. En particular, se han estudiado tres casos: dos redes triangulares de discos y de estrellas y una de estructura tipo panal de abeja de barras. Todos los sistemas se han diseñado de modo que el periodo es del orden de la longitud de onda de resonancia y los espacios entre estructuras suficientemente pequeños para tener acoplo de campo cercano. Además, en estos sistemas se ha utilizado de nuevo la configuración metal-aislante-metal, diseñada para obtener interferencia constructiva y, en consecuencia, picos de alta absorción. Las muestras se han fabricado utilizando

litografía por haces de electrones para poder cambiar fácilmente el diseño y estudiar los cambios en la respuesta óptica en función de la geometría. Tanto las simulaciones como las medidas de espectroscopía por transformada de Fourier muestran que, efectivamente, todos estos sistemas presentan picos de alta absorción en el visible, en el infrarrojo, o en ambos. Todos ellos presentan un pico de absorción ancho en el infrarrojo ligado a la excitación dipolar de los huecos entre nanoestructuras y picos más estrechos en el visible que corresponden a modos donde predomina el comportamiento colectivo del sistema. Además, el estudio de la evolución temporal del sistema muestra que este tipo de redes presentan una respuesta extendida en el tiempo inducida por la frustración geométrica del sistema, durante la cual el sistema oscila entre modos donde predomina la excitación dipolar de los huecos entre estructuras, frustrada para interacciones más allá de primeros vecinos, y modos colectivos que siguen la simetría de la red. Este tipo de respuesta es típica también de los sistemas magnéticos frustrados. Además, las interacciones colectivas dan lugar a aumentos del campo eléctrico en áreas muy extensas de la superficie, haciendo que estos elementos sean de interés para espectroscopias aumentadas con este efecto plasmónico. En comparación con otro tipo de estructuras donde el aumento del campo eléctrico es más elevado, pero en un lugar muy localizado, estas estructuras contrarrestarían el hecho de tener un aumento del campo eléctrico menor, con tener una mayor área donde aumentar la señal de la molécula, siendo, además, más reproducibles. Como prueba de concepto se han funcionalizado las muestras con mercaptopiridina mostrando que efectivamente sirven como sustratos para espectroscopia Raman amplificada en superficie.

